



Finite temperature field theory for the masses

Hugo Schérer

Department of Physics
McGill University, Montréal

April, 2024

A thesis submitted to McGill University in partial fulfillment of
the requirements of the degree of
Master of Science

Table of Contents

Abstract	iv
Acknowledgements	viii
Contribution of authors	x
List of Figures	xi
List of Tables	xv
List of Abbreviations	xvi
Introduction	1
1 Cosmology and dark matter	6
1.1 The early universe	6
1.2 Dark matter	12
1.3 The dark photon	14
2 Plasma physics	23
2.1 Classical, non-relativistic plasmas	24
2.2 General plasmas	27

TABLE OF CONTENTS

3 Finite temperature field theory	33
3.1 Path integral formulation of QFT	34
3.2 Imaginary time formalism	36
3.3 Self-energies in imaginary-time formalism	43
3.4 The imaginary part of self-energies	46
3.5 Forward scattering	51
4 Photon self-energy on shell	53
4.1 One-loop photon self-energy integral	54
4.1.1 Residue theorem exchange of poles trick	55
4.1.2 Equivalence with forward scattering	57
4.2 On-shell analytic approximations	61
4.2.1 Removing the $(K^2)^2$ term in the denominator	61
4.2.2 Integration by parts and sharp peak approximation	65
5 General photon self-energy	70
5.1 Real part	72
5.1.1 Final analytic expressions	77
5.1.2 Limits	80
5.1.3 Comparing analytic approximations to numerical results	82
5.2 Imaginary part	88
5.2.1 Final analytic expressions	93
5.2.2 Limits	95
5.2.3 Comparing analytic approximations to numerical results	97
Conclusion	103

TABLE OF CONTENTS

Appendix	105
A Discrepancies between analytic and numerical	105
References	107

Abstract

The Standard Model of particle physics is the most successful theory ever invented by humankind. At the same time, it is fundamentally incomplete. Among other things, it does not account for dark matter, which constitutes about 85% of the matter content of the universe. Many constraints on physics beyond the Standard Model come from astrophysics and cosmology. While collider physics computations can assume that processes happen in vacuum, our universe is far from being a vacuum, and this approximation will not hold in many astrophysical environments such as stars or the early universe. In these physical settings, an accurate description requires that we take into account thermal effects generated by the hot and dense medium. The Standard Model photon is particularly affected by in-medium effects. Indeed, densities of charged particles can be high in nature, and the photon's coupling to these charged particles is big enough to maintain a high interaction rate. In particular, the photon acquires an effective mass, or self-energy, in a plasma. Furthermore, it acquires a new, longitudinal degree of freedom, in addition to the two transverse ones present in vacuum.

Approximately 30 years ago, Braaten and Segel derived beautiful analytic approximations for the photon self-energy, more specifically for the longitudinal and transverse modes in a homogeneous and isotropic plasma. These expressions have since been used by many researchers in the high-energy physics phenomenology community. However, these dispersion relations are only valid in the on-shell regime, meaning for actual photons that can propagate

Abstract

through the medium for an arbitrarily high distance, or in the soft photon momentum regime. There exists no analytic approximation for the general photon self-energy, which would also be generally valid off shell, meaning for virtual photons which are intermediate states in particle physics processes and which can have any energy and momentum.

In this thesis, I first review some context about the search for physics beyond the standard model using cosmology and astrophysics, and show how the photon self-energy is a central element in a particular model, the dark photon. I then review some finite temperature field theory formalism and use it to compute the general photon self-energy in a homogeneous and isotropic medium to first order in the fine-structure constant. This is a general expression in the sense that it is valid on shell and off shell for any photon energy and momentum. I derive analytic approximations for the general self-energy, and I evaluate how good they are compared to numerical computations.

Abrégé

Le modèle standard de la physique des particules est la théorie la plus réussie jamais élaborée. En même temps, il est fondamentalement incomplet. Entre autres, le modèle standard ne peut expliquer la matière noire, qui constitue environ 85% de la matière de l'univers. De nombreuses contraintes sur la physique au-delà du modèle standard proviennent de l'astrophysique et de la cosmologie. Pour les calculs en physique des collisionneurs de particules, il est possible d'assumer que les processus se déroulent dans le vide. Par contre, notre univers est loin d'être vide, et cette approximation n'est pas adéquate pour traiter de nombreux environnements en astrophysique, tels que les étoiles ou l'univers primitif. Dans ces situations, une description précise nécessite de prendre en compte les effets thermiques générés par le milieu chaud et dense. Le photon du modèle standard est particulièrement affecté par ces effets thermiques. En effet, il peut exister des densités élevées de particules chargées dans la nature, et le couplage du photon avec ces particules chargées est suffisamment fort pour maintenir un taux d'interaction élevé. Le photon, en particulier, acquiert, dans un plasma, une masse effective, aussi appelée auto-énergie. De plus, il acquiert une nouvelle polarisation longitudinale, en plus des deux polarisations transversales présentes dans le vide.

Il y a environ 30 ans, Braaten et Segel ont dérivé de belles approximations analytiques pour l'auto-énergie des photons, pour le mode longitudinal et les modes transversaux, dans un plasma homogène et isotrope. Ces expressions ont depuis été utilisées par de nombreux

chercheurs en phénoménologie de la physique des hautes énergies. Cependant, ces relations de dispersion ne sont valables que pour les photons réels, qui peuvent se propager à travers le milieu sur une distance arbitrairement élevée, ou pour les photons avec une faible quantité de mouvement. Il n'existe aucune approximation analytique générale de l'auto-énergie des photons, qui serait également valable en général pour les photons virtuels, c'est-à-dire des photons intermédiaires dans les processus de la physique des particules.

Dans cette thèse, je passe d'abord en revue le contexte de la recherche d'une physique au-delà du modèle standard en utilisant la cosmologie et l'astrophysique, et je montre comment l'auto-énergie des photons constitue un élément central dans une théorie particulière, le photon sombre. Je passe ensuite en revue le formalisme de la théorie des champs à température finie, puis je l'utilise pour calculer une expression générale de l'auto-énergie des photons dans un milieu homogène et isotrope, au premier ordre dans la constante de structure fine. Il s'agit d'une expression générale dans le sens où elle est valable aussi bien pour les photons réels que les photons virtuels avec une énergie et une quantité de mouvement arbitraires. Je développe également des approximations analytiques pour cette auto-énergie, et j'évalue s'il s'agit de bonnes estimations de l'auto-énergie déterminée par des calculs numériques.

Acknowledgements

This work was carried out thanks to funding from the Fonds de recherche du Québec - Nature et technologies (FRQNT).

I would like to thank my supervisor, Prof. Katelin Schutz, and my co-supervisor, Prof. Oscar Hernández, for their advice, their support, and their help on this project. I would also like to thank all members of Prof. Katelin Schutz's group, with special thanks to Dr. Saniya Heeba, Nirmalya Brahma, Christian Capanelli, and Kelvin Chan, for the helpful scientific discussions and for their support as friends.

In addition, I would like to thank Prof. Luc Vinet, Elaine Caron, and Shihan Bryan Mattias, who have been mentors for me throughout my journey. I would also like to thank Angélique Desgroseilliers. I would finally like to thank my friends and family: the friends I made in physics (with special thanks to Marguerite Dion, Charles Raymond, Sovannie Sir, and Erny Au Yang), my colleagues and friends from CHU Sainte-Justine (everyone in the pharmacy department and the cystic fibrosis team, with special thanks to Hélène Roy, Denis Lebel, and Jean-François Bussières), my friends from a previous life (with special thanks to Bojan Odobasic, Alex Soucy, and especially Marylou Fournier-Tondreau), and my family (with special thanks to Jacques Schérer and Marianne Roche, Sylvie Allard and Benoît Forté, as well as Antoine Schérer and Sabrina Gallant).

You have been a source of inspiration and support for me. I wouldn't be where I am today without all of you.

Remerciements

Ces travaux ont été réalisés grâce au financement du Fonds de recherche du Québec - Nature et technologies (FRQNT).

Je tiens à remercier ma superviseure, Prof. Katelin Schutz, et mon co-superviseur, Prof Oscar Hernández, pour leurs conseils et leur soutien, ainsi que pour leur aide sur ce projet. Je voudrais également remercier tous les membres du groupe de Prof. Katelin Schutz, avec des remerciements particuliers à Dre Saniya Heeba, Nirmalya Brahma, Christian Capanelli et Kelvin Chan, pour les discussions scientifiques utiles et pour leur soutien en tant qu'amis.

De plus, je tiens à remercier Prof. Luc Vinet, Elaine Caron et Shihan Bryan Mattias, qui ont été des mentors pour moi tout au long de mon parcours. Je tiens également à remercier Angélique Desgroseilliers. J'aimerais enfin remercier mes amis et ma famille : les amis que je me suis fait en physique (avec des remerciements particuliers à Marguerite Dion, Charles Raymond, Sovannie Sir et Erny Au Yang), mes collègues et amis du CHU Sainte-Justine (tout le monde à la pharmacie et en fibrose kystique, avec des remerciements particuliers à Hélène Roy, Denis Lebel et Jean-François Bussières), mes amis d'une vie antérieure (avec des remerciements particuliers à Bojan Odobasic, Alex Soucy et tout spécialement Marylou Fournier-Tondreau), et ma famille (avec des remerciements particuliers à Jacques Schérer et Marianne Roche, Sylvie Allard et Benoît Forté, ainsi qu'Antoine Schérer et Sabrina Gallant).

Vous avez été pour moi une source d'inspiration et de soutien. Je ne serais pas là où je suis aujourd'hui sans vous tous.

Contribution of authors

Everything presented in Chapter 5 is original work from the author. The expression for the self-energy at the end of Section 4.1 is a known result, but the detailed derivation leading to it has so far remained unpublished. The rest of Chapter 4, as well as Chapters 1, 2 and 3, are all reviewing existing literature on which the original work is built.

List of Figures

1.1	The effective number of relativistic degrees of freedom as a function of (decreasing) temperature, considering only Standard Model of particle physics (SM) particles. The approximate periods when some important cosmic events happen are highlighted in light gray. Some key masses from Standard Model of particle physics (SM) particles are also displayed, to indicate approximately when they become non-relativistic. MRE stands for the time of matter-radiation equality. Adapted from [4].	10
1.2	The bullet cluster [6, 7]; retrieved online from [8]. The X-ray image (in pink) indicates where the bulk of the baryonic matter is. The concentration of mass (in blue) is reconstructed from gravitational lensing. The discrepancy is proof that collisionless dark matter is the main source of matter in this galaxy cluster.	13
1.3	Limits on the dark photon [11]; updated version retrieved online from [12]. Red regions indicate laboratory experiment bounds, green regions indicate astrophysical bounds, and blue regions indicate cosmological bounds.	17
1.4	Feynman diagram of a generic dark photon production process, with initial states i and final states f . There is always a generally off-shell Standard Model of particle physics (SM) photon A^μ oscillating into a dark photon S^μ with coupling κ . Adapted from [19].	20

LIST OF FIGURES

3.1	Schematic visualization of the contour for the path integral in the complex time plane. Adapted from [22].	38
3.2	Feynman diagram of the boson self-energy in our toy model. Adapted from [24].	43
3.3	Feynman diagram of an example fermion self-energy.	46
4.1	One-loop Feynman diagram of the photon self-energy.	54
4.2	Schematic visualization of the contours in the complex p_0 plane that are involved in the “exchange of poles” trick. On the left, the contour C is infinitesimally narrow in the real direction and extends to infinity in the imaginary direction; it encloses an infinite number of poles (the poles of \tanh at $p_0 = i\omega_n + \mu$). On the right, the semicircles of C' are closed at infinity and the contour now simply encloses the four poles of the fermion propagators.	56
4.3	Plots of $J(v)$ for some values of n (top and middle), and plots of $d\omega_p^2/dv$ for some values of $x = m/T$ and $y = \mu/T$ (bottom), as a function of v . The two top panels show that $J(v)$ is indeed quite flat, and the bottom one that $d\omega_p^2/dv$ is sharply peaked.	67
4.4	Dispersion relations for both photon modes on shell, using the analytical approximations; adapted from [1]. The longitudinal one stops when it crosses the light cone, shown in a dashed line. The values of x and y are the same as those from Figure 1 in [1]. The thermal correction of the electron mass wasn’t taken into account.	68
5.1	Plots of $J(v)$ for $\xi = 2$ and some values of n (top and middle), and plots of $d\omega_p^2/dv$ for some values of x and y (bottom), as a function of v . The bottom panel is the same as in Figure 4.3. This time, $J(v)$ is less flat than in the on-shell case.	82

5.2	Plots of the real part of the self-energy as a function of ω and k for L modes in the regime where $x = 0.1$ and $y = 0$. The self-energy is computed with the new analytic approximation $\Pi_a \simeq \omega_p^2 J(v_*)$ (top left panel), with the numerical integral of $F_a(v)$ (top middle panel), and with the expression from Braaten and Segel [1] (top right panel). The bottom panels show a ratio to assess the discrepancy between the approximations and the numerical evaluation, with the new analytic approximation on the bottom left and the one from Braaten and Segel [1] on the bottom right.	83
5.3	Plots of the real part of the self-energy as a function of ω and k for T modes in the regime where $x = 0.1$ and $y = 0$. The display is the same as Figure 5.2. .	84
5.4	Plots of the real part of the self-energy as a function of ω and k for L modes in the regime where $x = 10, y = 100$. The display is the same as Figure 5.2. .	85
5.5	Plots of the real part of the self-energy as a function of ω and k for T modes in the regime where $x = 10, y = 100$. The display is the same as Figure 5.2. .	86
5.6	Plots of $\Gamma(v)$ for $\xi = 2$ and some values of n (top and middle), and plots of $d\omega_p^2/dv$ for some values of x and y (bottom), as a function of v . For n corresponding to timelike photons, $n < 1$, $\Gamma(v)$ is only plotted in the relevant interval v_- to v_+ , shown in dashed vertical lines. For the spacelike photons, $\Gamma(v)$ is plotted from v_- to 1. The bottom panel is the same as in Figure 4.3. .	96
5.7	Plots of the imaginary part of the self-energy as a function of ω and k for L modes in the regime where $x = 0.1$ and $y = 0$. The self-energy is computed with the analytic approximation (top left panel) and the numerical integral of $D(v)$ (top right panel). The bottom panels show a ratio to assess the discrepancy between the analytic approximation and the numerical evaluation. The dashed region indicates where the imaginary part is exactly zero, due to kinematics arguments.	98

5.8	Plots of the imaginary part of the self-energy as a function of ω and k for T modes in the regime where $x = 0.1$ and $y = 0$. The display is the same as Figure 5.7.	99
5.9	Plots of the imaginary part of the self-energy as a function of ω and k for L modes in the regime where $x = 10$ and $y = 100$. The display is the same as Figure 5.7. In the gray region, both the analytic and numerical expressions evaluate to zero.	100
5.10	Plots of the imaginary part of the self-energy as a function of ω and k for T modes in the regime where $x = 10$ and $y = 100$. The display is the same as Figure 5.7. In the gray region, both the analytic and numerical expressions evaluate to zero.	101
A.1	Plots of the real part of the self-energy as a function of ω and k for L modes (top) and T modes (middle) in the regime where $x = 0.1$ and $y = 0$. The self-energy is computed with the analytic approximation $\Pi_a \simeq \omega_p^2 J(v_*)$ (left panel), the numerical integral using Equation (A.1) (middle panel), and the alternative numerical integral using Equation (A.2) (right panel). The bottom panels show a ratio to assess the discrepancy between both numerical evaluations, for L modes (left) and T modes (right).	106

List of Tables

List of Abbreviations

BBN	Big Bang nucleosynthesis
CMB	cosmic microwave background
DM	dark matter
EW	electroweak
FLRW	Friedmann–Lemaître–Robertson–Walker
FTFT	finite temperature field theory
KMS	Kubo–Martin–Schwinger
LSW	light shining through wall
QCD	quantum chromodynamics
QED	quantum electrodynamics
QFT	quantum field theory
SM	Standard Model of particle physics

Introduction

Our universe is not empty. Sometimes, we approximate the universe's background as a vacuum to simplify our computations, but there are instances where this is far from being a good approximation. The primordial universe, for example, is a hot and dense plasma, and the effects of this environment on particle properties must be taken into account. The interior of stars is another stellar example where we are far from being in a vacuum. These environments, because of their high interaction rates, are extremely interesting to look for new physics beyond the Standard Model of particle physics (SM), like dark matter signals.

One important in-medium effect is the modification of the dispersion relations of particles in a plasma. In quantum field theory (QFT), the dispersion of a particle is encoded in its propagator, which takes the form

$$D \sim \frac{i}{\omega^2 - k^2 - m^2} \tag{1}$$

in vacuum, where ω is the particle's energy, \mathbf{k} its momentum, and m its mass. Propagators are used for real or virtual particles, also called on shell and off shell, respectively. On-shell particles are the ones that can propagate to arbitrarily high distances and that obey this dispersion relation:

$$\omega^2 - k^2 = m^2. \tag{2}$$

Off-shell particles, on the other hand, can have any values of energy and momentum. In a

medium, the modification of the dispersion relation can be thought of as the particle having an effective mass which in general depends on its energy, its momentum, and the medium temperature.

Photon dispersion relations in a plasma are qualitatively different from their massless dispersion relations in vacuum. Plasmas are collections of moving charged particles. Due to the high interaction rate, these particles obey thermal distributions. Accelerating charged particles generate electromagnetic fields, i.e. photons on the quantum level. Therefore, plasmas also contain a thermal distribution of photons. The photon is massless in vacuum, obeying the dispersion $\omega^2 - k^2 = 0$. Therefore, any thermal correction to its dispersion relation gives rise to important qualitative differences in the photon behavior. Furthermore, photons in vacuum have two polarization modes, both transverse to the propagation direction. However, in-medium collective effects give rise to a third, longitudinal photon mode¹. This also leads to significant and qualitatively different phenomena in plasmas.

The in-medium photon behavior is encoded in the thermal photon self-energy² $\Pi^{\mu\nu}$, which depends on the inverse temperature $\beta = 1/T$. This appears in an effective Lagrangian as

$$\mathcal{L} \supset \frac{1}{2} A_\mu \Pi^{\mu\nu} A_\nu, \quad (3)$$

which is akin to a mass term for the photon field A^μ . Indeed, the real part of $\Pi^{\mu\nu}$ acts as an effective in-medium mass (squared), while the imaginary part encodes the production and absorption (or damping) of in-medium photons. For a homogeneous and isotropic medium, the longitudinal and transverse modes are decoupled, and the self-energy can thus be completely described by two form factors:

$$\Pi^{\mu\nu} = \Pi_L P_L^{\mu\nu} + \Pi_T P_T^{\mu\nu} \quad \text{with} \quad \Pi_a = P_a^{\mu\nu} \Pi_{\mu\nu}, \quad a = L, T. \quad (4)$$

¹In the literature, in-medium photons are sometimes referred to as plasmons. Sometimes, plasmons only refer to the new longitudinal mode. In this thesis, I refer to them as photons.

²The self-energy is sometimes also called the polarization tensor.

where $P_a^{\mu\nu}$, $a = L, T$, are projectors. The propagator can, in its turn, be decomposed in the same manner:

$$D^{\mu\nu} = D_L P_L^{\mu\nu} + D_T P_T^{\mu\nu} \quad \text{with} \quad D_a = \frac{i}{\omega^2 - k^2 - \Pi_a}, \quad a = L, T. \quad (5)$$

In general, the photon self-energy is an integral that can only be computed numerically, mainly due to the presence of thermal distributions inside the integral. However, in 1993, Braaten and Segel computed analytic approximations for the on-shell self-energy of longitudinal and transverse photons [1]. Remarkably, these are valid in all regimes, that is, for any photon energy and for any temperature and electron density. However, one crucial point of their calculation is the assumption that the photons are *on shell*. The research community did not fully appreciate that the expressions for the photon self-energy from [1] were derived for on-shell photons, and many authors have used these analytic approximations for computations involving off-shell photon propagators. While these analytic expressions are valid off shell for soft photon momentum (for example, in describing the screening effects of static electric fields [2]), they are not valid for off-shell photons in general. This overlooked fact is important enough that, in 2021, Raffelt published an erratum in his book stating (see Appendix E in [2]):

This section was aiming at the dispersion relations of transverse and longitudinal plasmons, following Braaten and Segel (1993) who provided beautiful analytic approximations. The expressions for the polarization tensor [...] are accurate to lowest order in α only in the neighborhood of $\omega \sim k$ and thus are only useful to find the dispersion relations. *They should not be used in the off-shell regime.*

It is therefore quite important to study the behavior of the self-energy in the off-shell regime and see how much it differs from the on-shell one.

Furthermore, no general off-shell analytic expression exists for the photon self-energy.

First, having analytic approximations for the photon self-energy can be a useful tool to save some time on the computations. For example, to compute the production of dark photons in the early universe, which is discussed in more detail in Chapter 1, one has to integrate over the energy and momentum entering the photon propagator, and the photon self-energy depends on these quantities. One then has to integrate over the range of temperatures during which the dark photon is produced. Having an analytic approximation for the photon self-energy instead of computing it numerically for each value of energy, momentum and temperature involved can thus save a lot of time. Furthermore, the photon self-energy is often involved in resonances, and having analytic approximations can help us find where these resonances happen for a given system and gain physical intuition.

In this thesis, I derive a general analytic approximation for the photon self-energy at one loop. It is general in the sense that it is valid off shell at all photon energy and momentum, in addition to on shell. This thesis is structured as follows. Chapter 1 reviews physics of the early universe in order to get a grasp on how plasma effects are important in this environment. It also introduces the dark photon, a well-motivated dark sector particle which could be the dark matter or act as a portal or a mediator. The photon self-energy determines when photon/dark photon resonances occur, and thus plays a crucial role in its phenomenology. The aim of this chapter is to provide a concrete example of the use of the photon self-energy and a motivation to compute it analytically. Chapter 2 introduces some key basic notions about plasma physics and how the photon dispersion relations come to be modified. It contains a classical derivation, as well as a zero-temperature QFT derivation. However, we cannot accurately compute the general thermal self-energy with these methods. Chapter 3 introduces the formalism of finite temperature field theory (FTFT), which is used to compute thermal self-energies. I focus on the imaginary-time formalism, which can be used when dealing with systems in thermal equilibrium. In Chapter 4, I review the existing computation for the on-shell photon self-energy, adding some detailed, intermediate

steps which are usually omitted in the literature. Finally, in Chapter 5, I present the new analytical computations for the general photon self-energy, and I assess their validity by comparing them to numerical computations. I find that the Braaten and Segel expressions [1] are indeed good approximations for photons close to the on-shell regime. However, some qualitatively different things happen when going further off shell. For example, there are some regions of the phase space where the self-energy is negative, something that never happens on shell.

The scope of this thesis is to compute and analyze the one-loop photon self-energy (i.e., to first order in α , the fine-structure constant), which is the dominant contributions in a number of physical contexts. However, there are situations where the one-loop contribution isn't enough to capture the relevant physics. For example, in ultrarelativistic plasmas, where the temperature is much greater than the mass of the charged particle ($T \gg m$), higher-loop corrections for hard photons near the mass shell ($\omega^2 - k^2 \sim \alpha T^2$) are of the same order as the one-loop contribution because the photons can remain collinear with charged particles over multiple scattering times [3]. The imaginary part as well vanishes for certain parts of the parameter space at one-loop and higher-loop contributions are thus obviously essential. These higher-loop considerations are outside the scope of this work.

Throughout this thesis, I work in natural units: $\hbar = c = \epsilon_0 = k_B = 1$. Every quantity is therefore expressed in units of energy, usually in eV, unless specified otherwise.

Chapter 1

Cosmology and dark matter

This first chapter is aimed at motivating the computation of the photon self-energy in the context of dark matter phenomenology. I will first review the thermal history of our universe, to highlight how this is an example of a hot and dense plasma where in-medium effects play an important role. I will then briefly discuss dark matter and dark sectors, focusing on the dark photon and emphasizing how in-medium effects, more specifically the photon self-energy, play a crucial role in this extension to the Standard Model of particle physics. This isn't an exhaustive treatment of the use of the photon self-energy but consists more in a detailed example that illustrates how an accurate computation of the photon self-energy can be crucial in certain physical contexts.

1.1 The early universe

The main idea of this section is to point out that the early universe is a hot and dense environment where in-medium effects are of great importance. I review here the essentials of standard cosmology theory to emphasize and develop this point. This section is mostly based on Reference [4].

Our universe is, on large scales, statistically homogeneous and isotropic. It is also ex-

panding with time. Thus, the dynamics of the universe is encoded in the scale factor $a(t)$ of the Friedmann–Lemaître–Robertson–Walker (FLRW) metric, or equivalently in the Hubble parameter $H(t) = \dot{a}/a$. This quantity is determined by the content of the universe through the first Friedmann equation, which is, assuming our universe has no intrinsic curvature¹,

$$H^2 = \frac{8\pi G}{3}\rho, \quad (1.1)$$

where ρ is the total energy density of the universe. The energy density varies differently with $a(t)$ depending on the type of energy content. For matter, or pressureless non-relativistic energy content, $\rho \propto a^{-3}$, which only represents the dilution of the energy density due to volume expansion of the universe. For radiation, which includes all relativistic particles (i.e., particles for which the energy is dominated by kinetic energy), $\rho \propto a^{-4}$. In this case, in addition to the volume expansion, the wavelength expands and redshifts, which reduces the energy density by an additional factor of $a(t)$. Finally, dark energy contributes with a constant energy density, independent of $a(t)$. This is sometimes referred to as the cosmological constant, Λ .

It is useful to rewrite the first Friedmann equation in terms of dimensionless energy densities of each component at the present day, Ω_i , as well as the Hubble parameter today, H_0 . These dimensionless energy parameters are in units of (today's) critical density:

$$\rho_{crit,0} = \frac{3H_0^2}{8\pi G} \quad \text{and} \quad \Omega_i = \frac{\rho_{i,0}}{\rho_{crit,0}} \quad i = m, r, \Lambda. \quad (1.2)$$

Then, with the convention of today's scale factor being $a(t_0) = 1$, we find:

$$\frac{H^2}{H_0^2} = \Omega_r a^{-4} + \Omega_m a^{-3} + \Omega_\Lambda. \quad (1.3)$$

¹Cosmological observations place stringent bounds on the curvature of our universe, meaning that, to a good approximation, our universe is flat. Therefore, I omitted the curvature term for simplicity.

The values of these parameters have been measured by different cosmological observations.

The latest measurements come from the Planck Collaboration in 2018 [4, 5]:

$$H_0 = 67.66 \pm 0.42 \text{ km s}^{-1} \text{ Mpc}^{-1},$$

$$\Omega_\Lambda = 0.6889 \pm 0.0056, \quad \Omega_m = 0.3111 \pm 0.0056, \quad \Omega_r \simeq 8.99 \times 10^{-5},$$

with uncertainties representing the 68% confidence interval. Today, the universe is thus dark energy dominated, with a significant matter contribution. Radiation is negligible. However, this wasn't always the case. Going back in time, as $a(t)$ gets smaller, we can clearly deduce that there was a period when the universe was matter-dominated and, prior to that, a period when it was radiation-dominated. This radiation-dominated early universe era is the one we are interested in. Neglecting all terms except radiation, we can solve the Friedmann equation and get

$$a(t) \propto \sqrt{t} \quad \text{and} \quad H = \frac{1}{2t}. \quad (1.4)$$

The energy density of a relativistic particle in thermal equilibrium is $\rho \propto T^4$. Comparing this with $\rho \propto a^{-4}$ leads to

$$T \propto \frac{1}{a} \propto \frac{1}{\sqrt{t}}. \quad (1.5)$$

As we go back in time, a smaller scale factor $a(t)$ represents a higher particle density and corresponds to a higher temperature, meaning that particle interaction rates were very high. At temperatures above 13.6 eV, everything was ionized². All this implies that the early universe was a plasma of particles in thermal contact with each other. This is the key point, and it is worth emphasizing: at early times, the universe was a hot and dense, homogeneous and isotropic plasma, and thus, in-medium effects on particle behavior were crucial.

I now go a bit further in the thermal history of the universe, to single out a particular

²In fact, because of entropy considerations, the universe is ionized until it reaches much lower temperatures of $T \sim 0.25 - 0.29$ eV, as pointed out in Table 1.1.

period around $T \gtrsim \text{MeV}$ when the early universe was an electron-positron plasma. This is exactly the kind of environment where the photon self-energy, the main quantity computed in this thesis, is very much relevant. Recall that a particle with mass m behaves like radiation as long as $T \gg m$. Furthermore, thermal equilibrium is achieved for this particle when its rate of interaction Γ is big enough to restore equilibrium, meaning when $\Gamma \gg H$ since the only other physically important rate is the Hubble parameter. In the very early universe, all particles behave like radiation, when the temperature is much higher than any of the particle masses. Then, two things can happen. First, when the temperature becomes low enough compared to a particle's mass, $T \lesssim m$, that particle species becomes non-relativistic and starts behaving like matter. To a good approximation, the early universe has a vanishing chemical potential $\mu \simeq 0$, so the energy density of non-relativistic particles in thermal equilibrium goes like $\rho \sim e^{-m/T}$. The density of a non-relativistic particle species is exponentially suppressed as long as these particles remain in thermal equilibrium. For the purpose of early universe dynamics, they become irrelevant. Second, when a particle's rate of interactions becomes low enough, $\Gamma \lesssim H$, that particle decouples from the thermal bath and isn't in thermal equilibrium anymore. We say that this particle freezes out. Its energy density then simply follows $\rho \propto a^{-4}$ or $\rho \propto a^{-3}$ depending on whether it's radiation or matter. Note that these two events can happen in any order for a given particle. They may also never happen; for example, the photons obviously never become non-relativistic.

With that in mind, we usually parameterize the energy density in the early universe as

$$\rho = \frac{\pi^2}{30} g_* T^4, \quad (1.6)$$

where

$$g_*(T) = \sum_{\substack{i=\text{rel.} \\ \text{boson}}} g_i \left(\frac{T_i}{T} \right)^4 + \frac{7}{8} \sum_{\substack{i=\text{rel.} \\ \text{fermion}}} g_i \left(\frac{T_i}{T} \right)^4 \quad (1.7)$$

is the effective number of relativistic degrees of freedom. This equation allows for particle

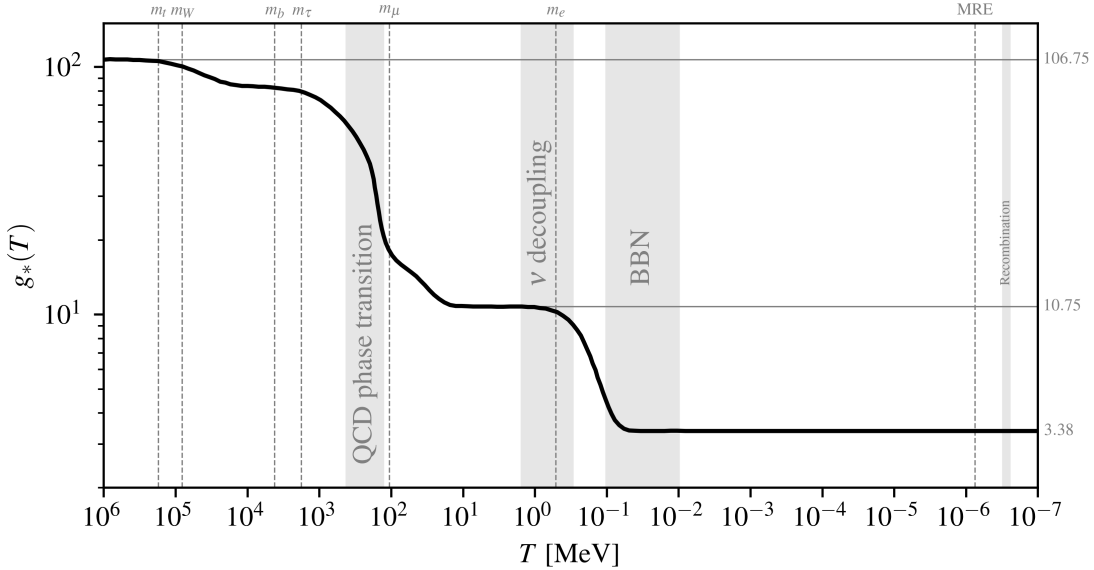


Figure 1.1: The effective number of relativistic degrees of freedom as a function of (decreasing) temperature, considering only SM particles. The approximate periods when some important cosmic events happen are highlighted in light gray. Some key masses from SM particles are also displayed, to indicate approximately when they become non-relativistic. MRE stands for the time of matter-radiation equality. Adapted from [4].

species having a temperature T_i different than that of the universe. The exact numerical prefactor for a given relativistic particle's equilibrium energy density depends only on its phase-space distribution, hence the factor of $7/8$ for fermions. Thus, we find:

$$H = \left(\frac{4\pi^3 G}{45} \right)^{1/2} \sqrt{g_*} T^2. \quad (1.8)$$

As the universe evolves and the temperature gets lower, more and more species become non-relativistic and stop contributing to $g_*(T)$. The evolution of $g_*(T)$ is shown in Figure 1.1 when considering only SM particles. Most of the time, g_* consists of just counting the relativistic degrees of freedom, so it mainly consists of plateaus. It changes mainly through sudden drops, at temperatures when particles become non-relativistic or at temperatures when phase transitions happen. Furthermore, $H \propto \sqrt{g_*} T^2$ changes as the temperature

Event	Time	Temperature
Inflation (?)	?	—
Baryogenesis (?)	?	?
EW phase transition	20 ps	100 GeV
QCD phase transition	20 μ s	150 MeV
Neutrino decoupling	1 s	1 MeV
Electron-positron annihilation	6 s	0.5 MeV
Big Bang nucleosynthesis	3 min	0.1 MeV
Matter-radiation equality	50 kyr	0.80 eV
Recombination	290–370 kyr	0.29–0.25 eV
Photon decoupling (CMB)	370 kyr	0.25 eV

Table 1.1: Main events in the thermal history of our universe. Adapted from [4].

lowers, which affects the specific time when given species decouple from this thermal bath.

Following these principles, the main events of the thermal history of our universe, once again allowing for SM particles only, are outlined in Table 1.1. Soon after the quantum chromodynamics (QCD) phase transition, muons and pions become non-relativistic and annihilate, at around $T \sim 100 - 10$ MeV. This is the epoch when $g_* = 10.75$, accounting for electrons, positrons, neutrinos and photons as the remaining relativistic particles. Then, neutrinos decouple at $T \sim 1$ MeV but stay relativistic. Electrons and positrons become non-relativistic closely after, at $T \sim 0.5$ MeV, but stay in thermal contact with the photons until recombination is over. Recombination is the process of electrons and protons combining to neutral hydrogen, meaning that photons ultimately stop scattering with, and decouple from, free electrons. These photons that last scattered with the early universe electrons traveled freely through the universe to reach us, and we detect them today in the microwave wavelengths as the cosmic microwave background (CMB).

It is clear now that there is a significant period of time when the early universe was essentially an electron-positron-proton plasma. This hot and dense medium must be taken into account when computing particle physics quantities such as interaction rates. This thermal history involving only SM particles predicts very well the measured primordial abundances

of light elements, synthesized during Big Bang nucleosynthesis (BBN). In fact, these BBN measurements are a reason why we can today claim that this thermal history of the universe after QCD phase transition is a scientific fact. The thermal effects related to the photon self-energy do not impact these predictions at leading order. They must be involved in a qualitatively different physical process to affect early universe physics. Dark matter and dark sector particles provide such new, qualitatively different circumstances, and the dark photon in particular crucially involves the photon self-energy through resonant mixing with the SM photon.

1.2 Dark matter

While the thermal history of our universe discussed in the previous section is an extremely successful theory, a key element is missing: dark matter (DM). This refers to non-baryonic energy content that acts as matter, i.e. that dilutes as $\rho \propto a^{-3}$. In addition to the total matter content of the universe, Ω_m , the CMB allows us to measure the baryonic content of the universe, Ω_b . Indeed, being collisionless, DM in the early universe creates background gravitational potential wells of some typical size given the DM abundance. The baryon-photon fluid oscillates in and out of these wells, due to the tension between the gravitational pull of the wells and the pressure of the fluid. The exact baryon abundance corresponds to typical length scales for the accumulation of baryons at the bottom as well as at the top of these potential wells. These oscillations occur until recombination ends and photons decouple. Then, these overdensities get imprinted in the photon fluid and we detect them today as anisotropies in the CMB. A detailed analysis of the CMB thus gives us information on the baryon content of the universe. The latest measurement, from Planck 2018, is $\Omega_b = 0.04897$ [5], which is wildly different from the total matter density parameter $\Omega_m = 0.3111$. Therefore, about 85% of the matter content of the universe consists of DM.

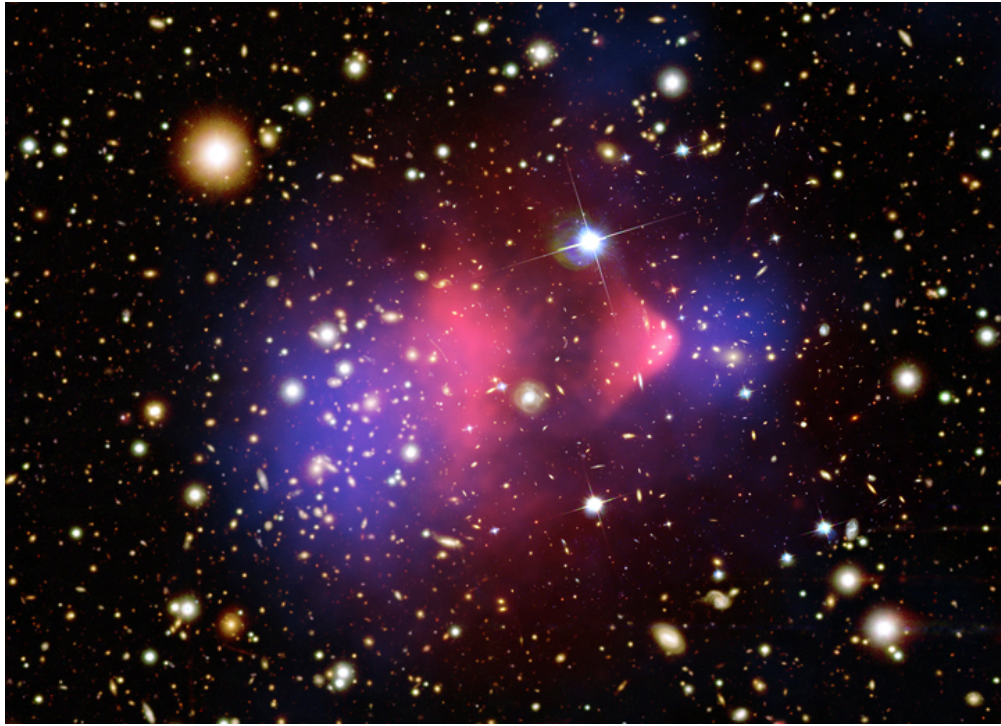


Figure 1.2: The bullet cluster [6, 7]; retrieved online from [8]. The X-ray image (in pink) indicates where the bulk of the baryonic matter is. The concentration of mass (in blue) is reconstructed from gravitational lensing. The discrepancy is proof that collisionless dark matter is the main source of matter in this galaxy cluster.

The CMB measurement is one of the best evidence for DM, but multiple other probes at different scales also confirm its existence. For example, cluster mergers, like the bullet cluster, shown in Figure 1.2, exhibit a clear separation between the bulk of the baryonic matter, detected through X-ray (in pink on the figure), and the bulk of the mass, detected through gravitational lensing (in blue on the figure). This proves that most of the matter in these galaxy clusters is non-baryonic [6, 7]. On an even smaller scale, rotation curves of individual galaxies show that the orbital velocities as a function of radial distance R from the galactic center saturate to a constant after a certain distance, instead of decaying like $1/\sqrt{R}$ as expected from the visible (baryonic) content of galaxies. This confirms that galaxies bathe in a halo of invisible (dark) matter; otherwise, such high velocities would simply disrupt them.

If we know for a fact that DM exists, we have not yet detected it, nor do we have any evidence about its fundamental nature. Many candidates for DM exist, and they span orders of magnitude in the mass of the individual constituents. In many cases, these DM candidates are new particles beyond the SM. Some models, collectively called dark sectors, include multiparticle extensions to the SM. For self-consistent studies of such extensions to the SM, one has to assume they were present in the early universe just like all SM particles. A good model will predict dark sector particle production in the early universe that matches the observed DM abundance when added together. Furthermore, their thermal history must be consistent with cosmological observations, such as primordial abundances of light elements from BBN or the CMB anisotropies power spectrum. Otherwise, when a model makes predictions that are in tension with these cosmological observables, we can put bounds on this model's parameters. Constraints can also come from astrophysical systems, by determining the consequences of these systems producing or interacting with these new particles.

1.3 The dark photon

One particularly interesting extension to the SM is the dark photon [9, 10]. This is a massive vector boson which mixes with the electroweak (EW) $U(1)$ gauge boson. It could constitute DM, but it could also simply be a state in the spectrum and part of a broader dark sector, acting as a portal between the SM and the dark sector. What makes it a compelling candidate for extending the SM is the fact that it couples to the photon through a dimension-4 operator. Therefore, from an effective field theory point of view, there is no reason for this interaction to be suppressed by a high-energy scale. Below the EW symmetry-breaking scale, the dark

photon mixes with the SM photon. The Lagrangian is

$$\mathcal{L} = -\frac{1}{4}F_{\mu\nu}F^{\mu\nu} - \frac{1}{4}V_{\mu\nu}V^{\mu\nu} + \frac{1}{2}(\sin \kappa)V_{\mu\nu}F^{\mu\nu} + \frac{1}{2}m_V^2(\cos^2 \kappa)V_\mu V^\mu + ej_\mu A_{SM}^\mu, \quad (1.9)$$

where V^μ is the dark photon field, m_V its Stueckelberg mass, and κ a dimensionless coupling constant called the kinetic mixing parameter. This parameter is small, $\kappa \lesssim 1$ and often $\kappa \ll 1$; otherwise, the dark photon interaction with the photon is so strong that we would have already detected it. Equation (1.9) is the exact Lagrangian, but due to the smallness of κ , this Lagrangian and the following equations in this section are often cited to first order in κ , using $\sin \kappa \simeq \tan \kappa \simeq \kappa$ and $\cos \kappa \simeq 1$.

It is often more convenient to redefine these fields in a different basis. First, there is the mass basis (or propagating modes), where the mass matrix is diagonal. The new fields are

$$\gamma_1 : A_1^\mu = A_{SM}^\mu - (\sin \kappa)V^\mu \quad (\text{Mostly photon}) \quad (1.10a)$$

$$\gamma_2 : A_2^\mu = (\cos \kappa)V^\mu \quad (\text{Mostly dark photon}) \quad (1.10b)$$

and the Lagrangian becomes

$$\mathcal{L} = -\frac{1}{4}F_{1,\mu\nu}F_1^{\mu\nu} - \frac{1}{4}F_{2,\mu\nu}F_2^{\mu\nu} + \frac{1}{2}m_V^2A_{2,\mu}A_2^\mu + ej_\mu(A_1^\mu + (\tan \kappa)A_2^\mu). \quad (1.11)$$

In this basis, each field is a well-defined propagating mode, but they both interact with SM currents, although A_2 's interaction is suppressed by a factor of $\tan \kappa \simeq \kappa$. The other interesting basis is the interaction basis, where the new fields are

$$\gamma : A^\mu = (\cos \kappa)A_{SM}^\mu \quad (\text{Active}) \quad (1.12a)$$

$$\gamma' : S^\mu = V^\mu - (\sin \kappa)A_{SM}^\mu \quad (\text{Sterile}) \quad (1.12b)$$

and the Lagrangian becomes

$$\begin{aligned} \mathcal{L} = & -\frac{1}{4}A_{\mu\nu}A^{\mu\nu} - \frac{1}{4}S_{\mu\nu}S^{\mu\nu} + \frac{1}{2}m_V^2(\sin^2\kappa)A_\mu A^\mu + \frac{1}{2}m_V^2(\cos^2\kappa)S_\mu S^\mu \\ & + m_V^2(\sin\kappa\cos\kappa)A_\mu S^\mu + e(\sec\kappa)j_\mu A^\mu. \end{aligned} \quad (1.13)$$

In this basis, only one of the fields, the active field, interacts with the SM currents. However, the mass matrix is not diagonal, and the active and sterile fields can oscillate into one another as they propagate, similarly to neutrino oscillations. In practice, since κ is small, the fields in these different bases, V^μ , A_2^μ and S^μ , are all the same at zeroth order in κ and are referred to as the dark photon in the literature.

In fact, multiple constraints exist on κ and m_V , as shown in Figure 1.3. Bounds from laboratory experiments are shown in red, those from astrophysical data in green, and those from cosmology in blue. I will now discuss these bounds and point out those that depend on the in-medium photon properties. Laboratory experiments can be grouped into general experiment categories. The names of the exact experiments corresponding to a given category are listed in Table 1.2. First, there are experiments placing bounds on the mass of the photon, or equivalently, testing for Coulomb's law. Indeed, if the photon has a non-zero mass m_A , the Coulomb potential is modified to $V(r) \propto \frac{1}{r}e^{-m_A r}$ [13]. Since the massive dark photon mediates some of the electromagnetic force between SM fermions, as we can see in the Lagrangian of Equation (1.11), these bounds on the photon mass can be translated to bounds on the dark photon parameters. Bounds on the photon mass also come from planetary magnetic fields, labeled here as Earth and Jupiter. Other bounds come from light shining through wall (LSW) experiments. Here, we rely on photon/dark photon oscillations in the active and sterile basis. The idea is that we send photons towards a “wall” that is opaque to photons but transparent to dark photons since they don't interact. We expect a certain amount of the photons to oscillate to dark photons before they reach the wall and

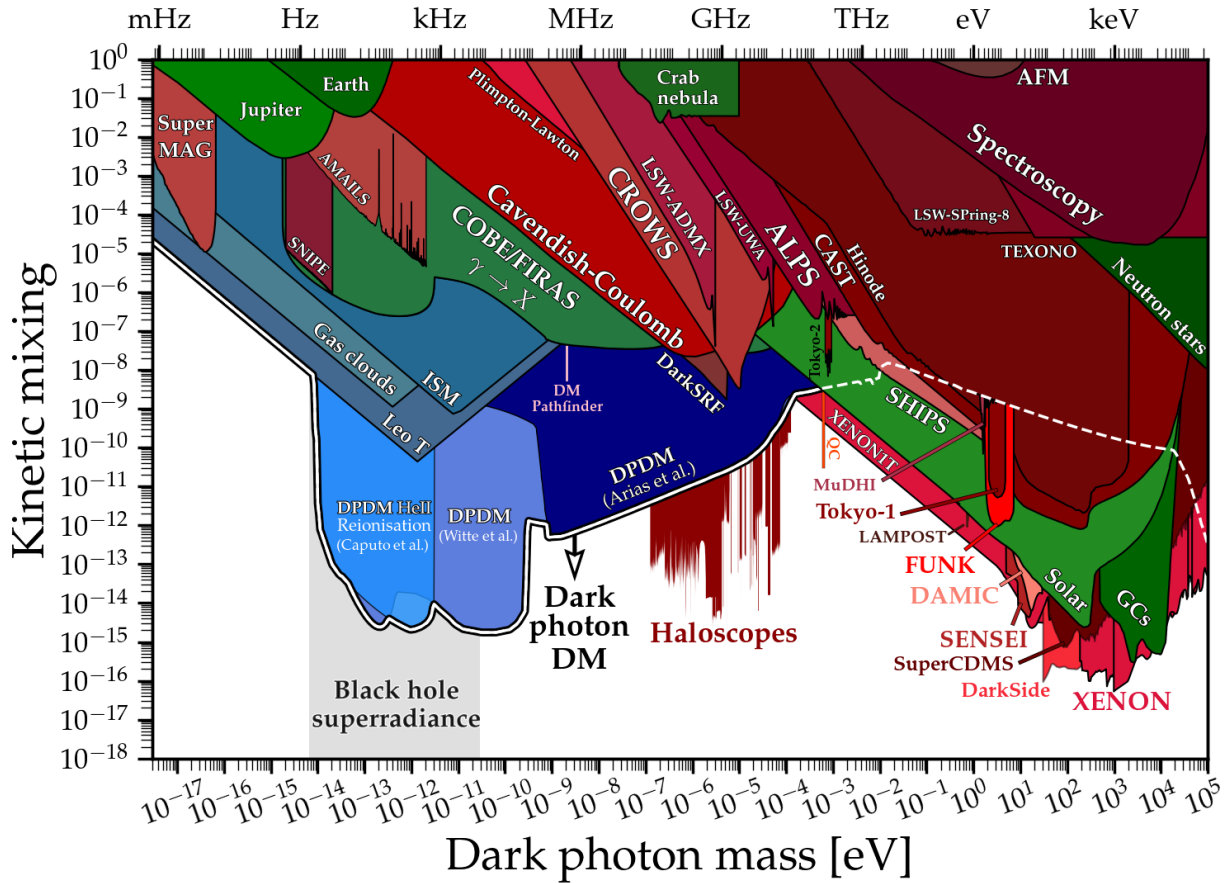


Figure 1.3: Limits on the dark photon [11]; updated version retrieved online from [12]. Red regions indicate laboratory experiment bounds, green regions indicate astrophysical bounds, and blue regions indicate cosmological bounds.

oscillate back to photons after they crossed it. Since the probability of conversion depends on the dark photon parameters, the absence of detection of photons behind the wall leads to constraints. There is a bound coming from the TEXONO experiment, which is a reactor neutrino experiment. Their 95% confidence interval of excess background events compared to SM expectations places a limit on the number of dark photon detection events in this experiment, which places bounds on the parameters. There is no environment where in-medium effects are relevant in any of these settings.

Then, there are the direct detection experiments. Those usually look for a direct interaction of DM with SM particles. The absence of events places bounds on the cross-section.

Haloscopes	Axion haloscopes	Helioscope
Dark E-field Radio	ADMX	CAST
SHUKET	HAYSTAC	CROWS
SQuAD	CAPP	
Tokyo-3	QUAX	
WISPD MX		
Direct detection	Coulomb law tests	Light shining through wall (LSW)
DAMIC	Cavendish-Coulomb	ALPS
FUNK	Plimpton-Lawton	LSW-SPring-8
SENSEI	(atomic) spectroscopy	LSW-UWA
SuperCDMS	atomic force microscopy (AFM)	LSW-ADMX
Tokyo-1, Tokyo-2	WISPD MX	
XENON1T, XENON100		
DarkSide		
LAMPOST		
MeDHI		
DM Pathfinder		

Table 1.2: Experiments placing bounds on the dark photon parameters space shown in Figure 1.3, grouped under broad experiment categories. See [11] for specific references for each of these.

In the case of the dark photon, this can be translated to bounds on the parameters. The bounds labeled Haloscopes are experiments looking for DM in our local halo, and include some dark photon direct detection experiments as well as some experiments designed to find axions but reinterpreted as dark photon searches. Although they were originally designed to look for DM from our halo, these experiments are also sensitive to dark photons coming to us from the sun. For example, the bounds from the SuperCDMS or XENON experiments take into account the solar production of dark photons [14, 15]. The production of dark photons inside the sun involves in-medium effects and, crucially, the photon self-energy. The last experimental bounds are helioscope experiments. These aim specifically at detecting dark photon emission from the sun, and the absence of a signal is once again used to place bounds on the parameters. These bounds obviously rely on the dark photon production rate in the

sun [16, 17]. Having an improved expression for the photon self-energy has the potential to substantially modify all these experimental bounds.

The blue DPDM limits stand for cosmological analysis of dark photons as dark matter. These constraints rely on dark photon production in the early universe, which includes in-medium effects through the photon self-energy. These are bounds where the photon self-energy plays a crucial role. The other blue limits also require dark photons as DM, and are constraints on heating of the interstellar medium (ISM), of the gas in the Leo T dwarf galaxy, and of the gas clouds at the galactic center of G357.8-4.7-55. These environments do not exhibit relevant in-medium properties.

For astrophysical bounds, there are “energy loss” bounds, which rely on the absence of anomalous energy loss from stars to place bounds on the parameters. These come from different types of stars, the sun (solar), neutron stars, red giants, and horizontal branch stars from globular clusters (GCs) [18]. The inside of stars is a thermal medium, and the photon self-energy plays a role in determining the production rate here. Finally, there is a bound on CMB photons oscillating to dark photons. These would create spectral distortions in the CMB, which are tightly constrained by COBE and FIRAS. All these bounds could also potentially be substantially modified when using improved expressions for the photon self-energy.

To see how in-medium effects affect processes involving the dark photon, we first expand the Lagrangian from Equation (1.13) to first order in κ , which yields the following interacting terms:

$$\mathcal{L} \supset \kappa m_V^2 A_\mu S^\mu + ej_\mu A^\mu. \quad (1.14)$$

Consider a generic process $i \rightarrow f + S$ as shown in Figure 1.4. We are considering the interaction basis for this derivation because the result arises more intuitively. Since the dark photon interacts only with the photon through oscillations, this kind of process always involves a photon propagator, which isn’t necessarily on shell. As discussed in more detail

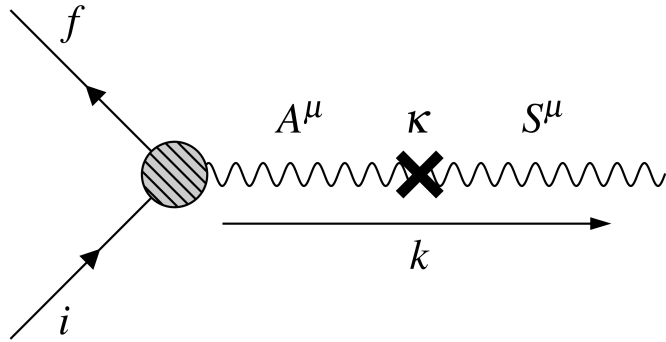


Figure 1.4: Feynman diagram of a generic dark photon production process, with initial states i and final states f . There is always a generally off-shell SM photon A^μ oscillating into a dark photon S^μ with coupling κ . Adapted from [19].

in Chapter 2, the in-medium photon has two transverse (T) and one longitudinal (L) mode. Furthermore, its propagator is modified with respect to the vacuum one:

$$D_a = \frac{i}{\omega^2 - k^2 - \Pi_a(\omega, k; T)}, \quad (1.15)$$

where $a = L, T$ and where the photon self-energy for a given mode Π_a can be thought of as a complex-valued ‘‘fudge factor’’ modifying the propagator for the purpose of this discussion. Note that the propagator is different for different modes, and has implicitly been decomposed in form factors here,

$$D^{\mu\nu} \sim \sum_a \epsilon_a^\mu \epsilon_a^{*\nu} D_a, \quad (1.16)$$

where ϵ_a is the polarization vector for a given mode. Therefore, the matrix element for the general process of Figure 1.4 is given by [19]

$$\mathcal{M}_a = \kappa m_V^2 [\mathcal{M}_{\text{QED}}^\mu] D_{\mu\nu} \epsilon_a^\nu, \quad (1.17)$$

where κm_V^2 comes from the photon/dark photon interaction coupling in Equation (1.14), $D_{\mu\nu}$ is the (generally off-shell) photon propagator, and $\mathcal{M}_{\text{QED}}^\mu$ encompasses everything happening

in the $i \rightarrow f$ portion of this diagram. Projecting on a specific mode $a = L, T$, we get

$$\mathcal{M}_a = \kappa m_V^2 \frac{i}{\omega^2 - k^2 - \Pi_a} [\mathcal{M}_{\text{QED}}^\mu \epsilon_\mu^a]. \quad (1.18)$$

Then, physical quantities like rates or cross-sections are proportional to

$$|\mathcal{M}_a|^2 = \frac{\kappa^2 m_V^4}{(\omega^2 - k^2 - \text{Re } \Pi_a)^2 + (\text{Im } \Pi_a)^2} |\mathcal{M}_{\text{QED}}^\mu \epsilon_\mu^a|^2. \quad (1.19)$$

Therefore, when computing rates or cross-sections involving dark photons, we can compute the usual QED matrix elements as if it were involving a photon, and multiply it by an effective mixing parameter, specific to each mode $a = L, T$ [19]:

$$\kappa_{\text{eff},a}^2(T) = \frac{\kappa^2 m_V^4}{(\omega^2 - k^2 - \text{Re } \Pi_a)^2 + (\text{Im } \Pi_a)^2}, \quad (1.20)$$

where the temperature dependence lies in the photon self-energy. The dark photon always interacts with SM particles through a photon, and this discussion has kept things general on the SM side of the process. Therefore, this effective mixing parameter can be used for any production process for the dark photon involving SM particles. As a simple example, this could be used to compute the rate of production from $e^+e^- \rightarrow \gamma'$ for a heavy dark photon ($m_V > 2m_e$). This effective mixing parameter clearly has a resonance structure. The real part determines the resonant temperature or temperatures, or, in the case of primordial production, the precise cosmological epoch when the resonant production of dark photons happens. The imaginary part quantifies the magnitude of this production around resonance. Because of the resonance structure, an accurate expression of the photon self-energy is needed. Even for hard momenta (for example, coming from a hard ultrarelativistic dark photon), the mass can match the photon self-energy and give rise to a resonance. Again, since, in general, the photon is off shell in the diagram of Figure 1.4, an off-shell expression

valid at all momenta is required for the self-energy.

In summary, the dark photon is an example of a well-motivated extension to the SM that includes qualitatively new circumstances and specifically involves the in-medium photon self-energy. This whole chapter motivates, in some detail, the need for computing the off-shell photon self-energy for one specific physical setting. Still, since the photon self-energy is a general and ubiquitous in-medium physical phenomenon, it is relevant in multiple other physical contexts.

Chapter 2

Plasma physics

To understand in-medium effects properly, we first need to understand a few basic concepts about plasma physics. A plasma is an ionized gas that can be pictured as a system of two fluids with opposite charges. The movement of these fluids produces charge separation, which gives rise to strong restoring forces. This is what generates oscillations in the overall charge density. It thus also generates oscillations in particle density and average velocity. Finally, the **E** and **B** fields oscillate as well, as a result of charge oscillations.

These collective excitations allow for a third, longitudinal polarization state for the electromagnetic field in medium, in addition to the two transverse modes also present in vacuum. This new longitudinal mode must be carried by the medium, as opposed to the transverse ones, and is thus qualitatively different. The plasma singles out a preferred inertial frame, namely the frame where the bulk velocity of the plasma is zero, often called the *medium rest frame*. Longitudinal and transverse modes are defined in the medium rest frame with respect to the propagation.

The purpose of this chapter is to present the equations of motion of plasmas and solve them for the dispersion relations or for the propagator of in-medium photons. First, I will discuss the classical, non-relativistic derivation of the plasma equations. Then, I will

turn to a general plasma in the context of zero-temperature QFT. I will assume statistical homogeneity and isotropy throughout this chapter.

2.1 Classical, non-relativistic plasmas

This section is based on chapter 10 of Reference [20]. Consider a plasma consisting of electrons and ions. Since the electrons are much lighter than the ions, the latter can effectively be treated as if they are at rest in the medium rest frame. We are thus interested in the motion of the electron fluid, described by a number density n and an average velocity \mathbf{v} , both functions of time and space. In the absence of external charge and current, the charge density and current density of this system are

$$\rho = e(n - n_0), \quad \mathbf{J} = env, \quad (2.1)$$

where n_0 is the constant equilibrium electron density. The plasma is governed by Maxwell's equations,

$$\begin{aligned} \nabla \cdot \mathbf{E} &= e(n - n_0) & \nabla \times \mathbf{E} + \partial_t \mathbf{B} &= 0 \\ \nabla \cdot \mathbf{B} &= 0 & \nabla \times \mathbf{B} - \partial_t \mathbf{E} &= env \end{aligned} \quad (2.2)$$

as well as the continuity and the Euler equations,

$$\partial_t n + \nabla \cdot (n\mathbf{v}) = 0, \quad (2.3)$$

$$\partial_t \mathbf{v} + (\mathbf{v} \cdot \nabla) \mathbf{v} = \frac{e}{m}(\mathbf{E} + \mathbf{v} \times \mathbf{B}) - \frac{1}{mn} \nabla p. \quad (2.4)$$

The Euler equation can be understood as Newton's second law for the electron mass density $\rho_m = mn$. On the left-hand side, the total time derivative has been expanded in partial derivatives. On the right-hand side, there is the Lorentz force, as well as an electron pressure term which describes the effects of the thermal kinetic energy of the electrons.

We can see that there is a solution with a static electron fluid, i.e., $n = n_0$, $\mathbf{v} = 0$, $p = 0$, and $\mathbf{E} = \mathbf{B} = 0$. We can expand around this solution to first order in $n - n_0 = \tilde{n}$, \mathbf{v} , \mathbf{E} , and \mathbf{B} . We find these linearized equations of motion:

$$\partial_t \tilde{n} + n_0 \nabla \cdot \mathbf{v} = 0 \quad (2.5a)$$

$$\partial_t \mathbf{v} - \frac{e}{m} \mathbf{E} + \frac{1}{mn_0} \left(\frac{\partial p}{\partial n} \right)_0 \nabla \tilde{n} = 0 \quad (2.5b)$$

$$\nabla \cdot \mathbf{E} - e \tilde{n} = 0 \quad (2.5c)$$

$$\nabla \cdot \mathbf{B} = 0 \quad (2.5d)$$

$$\nabla \times \mathbf{E} + \partial_t \mathbf{B} = 0 \quad (2.5e)$$

$$\nabla \times \mathbf{B} - \partial_t \mathbf{E} - en_0 \mathbf{v} = 0. \quad (2.5f)$$

Taking the time derivative of Equation (2.5a), and then plugging in Equation (2.5b), we find the equation of motion for the electron density,

$$\partial_t^2 \tilde{n} - 3 \langle u^2 \rangle \nabla^2 \tilde{n} + \omega_p^2 \tilde{n} = 0, \quad (2.6)$$

with

$$\langle u^2 \rangle = \frac{1}{3m} \left(\frac{\partial p}{\partial n} \right)_0, \quad (2.7)$$

$$\omega_p^2 = \frac{4\pi\alpha n_0}{m}, \quad (2.8)$$

where $\langle u^2 \rangle^{1/2}$ is the root mean square thermal velocity, ω_p is called the plasma frequency, and $\alpha = e^2/4\pi$ is the fine-structure constant. Furthermore, taking the time derivative of Equation (2.5f), and then plugging in Equations (2.5b) and (2.5c), we get an equation for the fields:

$$\partial_t^2 \mathbf{E} - 3 \langle u^2 \rangle \nabla (\nabla \cdot \mathbf{E}) + \omega_p^2 \mathbf{E} = \nabla \times \partial_t \mathbf{B}. \quad (2.9)$$

Going further, using Equation (2.5e) to get rid of the \mathbf{B} field, and using

$$\nabla \times (\nabla \times \mathbf{E}) = \nabla(\nabla \cdot \mathbf{E}) - \nabla^2 \mathbf{E}, \quad (2.10)$$

we get

$$\partial_t^2 \mathbf{E} - \nabla^2 \mathbf{E} - (3 \langle u^2 \rangle - 1) \nabla(\nabla \cdot \mathbf{E}) + \omega_p^2 \mathbf{E} = 0. \quad (2.11)$$

Equations (2.6) and (2.11) both have the structure of a wave equation and we can solve them by going to Fourier space, assuming plane wave solutions. Furthermore, we decompose the \mathbf{E} field in components longitudinal and transverse to the wave vector:

$$\mathbf{E}_L = \mathbf{E}_{\parallel} = \frac{\mathbf{k} \cdot \mathbf{E}}{k^2} \mathbf{k}, \quad \mathbf{E}_T = \mathbf{E}_{\perp} = \mathbf{E} - \mathbf{E}_{\parallel}. \quad (2.12)$$

This yields

$$(\omega^2 - \omega_p^2 - 3 \langle u^2 \rangle k^2) \tilde{n} = 0, \quad (2.13)$$

$$(\omega^2 - \omega_p^2 - 3 \langle u^2 \rangle k^2) \mathbf{E}_L + (\omega^2 - \omega_p^2 - k^2) \mathbf{E}_T = 0. \quad (2.14)$$

Recall that this is only valid to first order in electron average velocity, as well as in the field amplitudes and electron overdensities. Therefore, this is only valid for non-relativistic plasmas with small enough values of k and with electrons close to thermal equilibrium. The (decoupled) dispersion relations can be read off directly from Equation (2.14):

$$\omega^2 = \omega_p^2 + k^2 \quad \text{Transverse} \quad (2.15a)$$

$$\omega^2 = \omega_p^2 + 3 \langle u^2 \rangle k^2 \quad \text{Longitudinal} \quad (2.15b)$$

This is the main result of this section. The transverse modes are the same as the vacuum ones, except they have a modified dispersion relation with an effective mass of ω_p due to

in-medium effects, as opposed to their massless dispersion relation in vacuum. The longitudinal mode doesn't exist in vacuum and is therefore completely new. The dispersion relation yields the same solution for the energy as the electron density oscillation frequency from Equation (2.13). We thus see that this new mode arises from the collective, coherent oscillations of the background electron density in the propagation direction.

This section highlighted some key features of plasmas. First, plasmas exhibit charge density oscillations, and these are governed by the plasma frequency ω_p , which depends on temperature (through the equilibrium electron density in the non-relativistic case). These collective oscillations give rise to a new, longitudinal mode for the electromagnetic field, and to an effective mass for the transverse modes. The dispersion relations depend on the plasma frequency.

2.2 General plasmas

We now turn to a more general discussion of plasma physics in the context of QFT, without assuming any particular regime. Here, the formalism is the usual, zero-temperature QFT. Even if the polarization tensor $\Pi^{\mu\nu}$ is introduced, it still is a fudge factor that depends on the temperature. Indeed, there is no way to compute it without using FTFT, which is the subject of Chapter 3. For the present discussion, we just postulate its existence.

This section is mostly based on section 6.3 of Reference [2]. We are still assuming homogeneity and isotropy, as well as flat spacetime (special relativity). First, we start with a bit of notation. There is a preferred inertial frame, the medium rest frame, but we can still keep things Lorentz covariant if we define the plasma bulk velocity U^μ , which is $U^\mu = (1, \mathbf{0})$ in the medium rest frame. As usual, $U^2 = 1$. The photon field is denoted A^μ , and its momentum K^μ . In the medium rest frame, it is explicitly $K^\mu = (\omega, \mathbf{k})$. Note that

ω and $k = |\mathbf{k}|$ are Lorentz scalars, covariantly expressed as

$$\omega = U \cdot K, \quad k = \sqrt{(U \cdot K)^2 - K^2}. \quad (2.16)$$

The quantum electrodynamics (QED) Lagrangian for photons is

$$\mathcal{L} = -\frac{1}{4}F_{\mu\nu}F^{\mu\nu} + J_\mu A^\mu. \quad (2.17)$$

The equations of motion are Maxwell's equation in covariant form:

$$(\partial_\alpha \partial^\alpha \eta^{\mu\nu} - \partial^\mu \partial^\nu) A_\nu = J^\mu. \quad (2.18)$$

One can prescribe external currents J_{ext}^μ for a given physical situation and solve these equations of motions. In addition, the charged particles move in response to the electromagnetic fields, which generates an induced current J_{ind}^μ . For sufficiently weak fields, we can assume linear response, that is, the induced current depends linearly on the electromagnetic fields. In Fourier space, linear response is mathematically stated as $J_{\text{ind}}^\mu = \Pi^{\mu\nu}A_\nu$, where $\Pi^{\mu\nu}(K)$ is called the polarization tensor or the photon self-energy and depends on K in general. The total current is thus $J^\mu = J_{\text{ind}}^\mu + J_{\text{ext}}^\mu$. We get the following equation of motion:

$$-(K^2\eta^{\mu\nu} - K^\mu K^\nu + \Pi^{\mu\nu})A_\nu = J_{\text{ext}}^\mu \quad (2.19)$$

Gauge invariance under $A_\nu \rightarrow A_\nu + \lambda K_\nu$ leads to $\Pi^{\mu\nu}K_\nu = 0$. Current conservation for the external and total currents, $K_\mu J^\mu = K_\mu J_{\text{ext}}^\mu = 0$, leads to $K_\mu \Pi^{\mu\nu} = 0$. In a homogeneous and isotropic plasma, it turns out that $\Pi^{\mu\nu}$ is symmetric, so these conditions are redundant. Still, they hold in general for any polarization tensor, even in parity-violating medium, for example.

Next, we define a useful basis of orthogonal unit vectors and projectors. This will serve to decompose Minkowski space into the orthogonal longitudinal and transverse subspaces. Working in Lorenz gauge, $K_\mu A^\mu = 0$, we define first a gauge unit vector, $e_g \propto K^\mu$, which thus represents a non-propagating mode. Then, we define a longitudinal unit vector e_L , which is the unique unit vector orthogonal to e_g with a non-zero component in the direction of \mathbf{k} . This represents the longitudinal mode introduced in Section 2.1. The last two unit vectors represent the two transverse circular modes. We choose the circular polarization to preserve azimuthal symmetry around \mathbf{k} . Defining

$$\tilde{U}^\mu = U^\mu - \frac{\omega}{K^2} K^\mu \implies \tilde{U}^2 = -\frac{k^2}{K^2}, \quad (2.20)$$

we get the following explicit expressions for the unit vectors:

$$e_g^\mu = \frac{K^\mu}{\sqrt{K^2}} = \frac{(\omega, 0, 0, k)}{\sqrt{K^2}}, \quad (2.21a)$$

$$e_L^\mu = -\frac{\sqrt{K^2}}{k} \tilde{U}^\mu = \frac{(k, 0, 0, \omega)}{\sqrt{K^2}}, \quad (2.21b)$$

$$e_\pm^\mu = \frac{(0, 1, \pm i, 0)}{\sqrt{2}}. \quad (2.21c)$$

The gauge and longitudinal vectors e_g and e_L are first expressed in covariant form, and then component by component in the medium rest frame with \mathbf{k} pointing in the $\hat{\mathbf{z}}$ direction. The transverse vectors e_+ and e_- have only been introduced in this specific frame. For timelike ($K^2 > 0$) excitations, these are normalized such that $e_g \cdot e_g^* = 1$ and $e_a \cdot e_a^* = -1$ for $a = \pm, L$. For spacelike ($K^2 < 0$) excitations, e_g and e_L are purely imaginary instead of real, meaning $e_g \cdot e_g^* = -1$ and $e_L \cdot e_L^* = 1$. In both cases, $e_g \cdot e_g^* = |K^2|/K^2$ and $e_L \cdot e_L^* = -|K^2|/K^2$.

Therefore, we define the subspace projectors as $P_a^{\mu\nu} = e_a^\mu e_a^{*\nu}/(e_a \cdot e_a^*)$, i.e. explicitly:

$$P_g^{\mu\nu} = \frac{K^2}{|K^2|} e_g^\mu e_g^{*\nu} = \frac{K^\mu K^\nu}{K^2} \quad (2.22a)$$

$$P_L^{\mu\nu} = -\frac{K^2}{|K^2|} e_L^\mu e_L^{*\nu} = -\frac{K^2}{k^2} \tilde{U}^\mu \tilde{U}^\nu \quad (2.22b)$$

$$P_+^{\mu\nu} = -e_+^\mu e_+^{*\nu} \quad (2.22c)$$

$$P_-^{\mu\nu} = -e_-^\mu e_-^{*\nu} \quad (2.22d)$$

$$P_T^{\mu\nu} = P_+^{\mu\nu} + P_-^{\mu\nu} = \eta^{\mu\nu} + \frac{K^2}{k^2} \tilde{U}^\mu \tilde{U}^\nu - \frac{K^\mu K^\nu}{K^2}. \quad (2.22e)$$

The transverse projector comes from the fact that

$$\eta^{\mu\nu} = P_g^{\mu\nu} + P_L^{\mu\nu} + P_+^{\mu\nu} + P_-^{\mu\nu}. \quad (2.23)$$

Working in this basis, the most general form for the photon self-energy is

$$\Pi^{\mu\nu} = \sum_{a,b} \pi_{a,b} e_a^\mu e_b^{*\nu}, \quad (2.24)$$

where a and b run over all polarizations, $\{g, +, -, L\}$. From gauge invariance and current conservation, any term containing e_g must be exactly zero. Furthermore, since the medium is isotropic, the self-energy must have an azimuthal symmetry around \mathbf{k} . This means that the only surviving terms are those proportional to $e_a^\mu e_a^{*\nu}$. Thus, we can write:

$$\Pi^{\mu\nu} = - \sum_{a=\pm,L} \Pi_a P_a^{\mu\nu}, \quad (2.25)$$

where $\Pi_a = -P_a^{\mu\nu} \Pi_{\mu\nu}$. In the absence of external currents, the equation of motion becomes

$$(K^2(\eta^{\mu\nu} - P_g^{\mu\nu}) + \Pi^{\mu\nu}) A_\nu = 0. \quad (2.26)$$

Plugging in the decomposition of the metric and the self-energy in terms of the different projectors, we get

$$\sum_{a=\pm,L} (\omega^2 - k^2 - \Pi_a(\omega, k)) A_a^\mu = 0, \quad (2.27)$$

where $A_a^\mu = P_a^{\mu\nu} A_\nu$. These are clearly three decoupled degrees of freedom. For systems that are even under parity, the two transverse modes are degenerate. In this case, there are two dispersion relations, which can be read directly from Equation (2.27):

$$\omega^2 - k^2 = \Pi_a(\omega, k), \quad a = L, T. \quad (2.28)$$

We clearly see that the self-energy acts as an effective mass (squared) for the photon. The self-energy and the propagator are each fully determined by two form factors:

$$-\Pi^{\mu\nu} = \Pi_L P_L^{\mu\nu} + \Pi_T P_T^{\mu\nu}, \quad (2.29)$$

$$D^{\mu\nu} = \frac{i}{\omega^2 - k^2 - \Pi_L} P_L^{\mu\nu} + \frac{i}{\omega^2 - k^2 - \Pi_T} P_T^{\mu\nu}. \quad (2.30)$$

In practice, the Feynman rules are stated in a way consistent with the previous analysis such that the self-energy appearing in the propagator is given by

$$\Pi_a = -P_{\mu\nu}^a \Pi^{\mu\nu}, \quad a = \pm, L. \quad (2.31)$$

Therefore, in practice, the longitudinal and transverse self-energies are given by

$$\Pi_L = -P_{\mu\nu}^L \Pi^{\mu\nu}, \quad \Pi_T = -\frac{1}{2} P_{\mu\nu}^T \Pi^{\mu\nu}. \quad (2.32)$$

The factor of 1/2 for the transverse modes comes from the fact that we are averaging over two equivalent transverse modes, i.e., $-P_{\mu\nu}^T \Pi^{\mu\nu} = \Pi_+ + \Pi_- = 2\Pi_T$. It is straightforward to

evaluate these projectors in the medium rest frame:

$$\Pi_L = \frac{K^2}{k^2} \Pi^{00}, \quad \Pi_T = \frac{1}{2} \left(\delta_{ij} - \frac{k_i k_j}{k^2} \right) \Pi^{ij}. \quad (2.33)$$

Equation (2.33) is what I use in Chapters 4 and 5 to compute the self-energy of each mode. Now, we need a way to find an expression for $\Pi^{\mu\nu}$. Therefore, in the next chapter, we turn to the field theory formalism necessary to access the thermal photon self-energy.

Chapter 3

Finite temperature field theory

Usual QFT matrix elements computations assume that the particles propagate in vacuum. This can be more accurately referred to as zero-temperature quantum field theory, as opposed to finite temperature field theory. In FTFT, we are interested in computing thermal averages, like $\langle A^\mu A^\nu \rangle_\beta$, for example, where $\beta = 1/T$ is the inverse temperature. As discussed in Chapter 2, the surrounding thermal medium can significantly alter the propagation of particles, and it turns out that the propagator in FTFT is the main quantity where thermal corrections enter.

There are multiple formalisms to deal with quantum fields at finite temperatures. The imaginary-time formalism is a way to compute quantities for a system which is in thermal equilibrium. The core of this formalism is the realization that the density matrix of a quantum system in thermal equilibrium has the same functional form as a quantum evolution operator, where the inverse temperature β acts as an imaginary time. With this, we can formulate the theory as a QFT, and perform computations using the same tools we use for zero-temperature field theory. In particular, this includes perturbation theory with Feynman diagrams that are the same as in zero-temperature QFT. Since the system is in equilibrium, there is no time evolution and we can trade time with temperature in this description.

3.1 Path integral formulation of QFT

The best way to exhibit the parallel between zero-temperature QFT and FTFT is through the path integral formulation of these theories. In this section, I will first review some key elements of the path integral formulation of QFT. I will develop this formalism for a (bosonic) scalar field to illustrate its essential properties and then comment on the variations for fermions. This treatment can be formally generalized to any QFT. This section is mostly based on Reference [21].

For a system in thermal equilibrium, the Hamiltonian H is independent of time. Recall that the time-evolution operator from t_1 to t_2 is, for a time-independent Hamiltonian,

$$U(t_2, t_1) = e^{-i(t_2-t_1)H}. \quad (3.1)$$

This is a unitary operator since the Hamiltonian is Hermitian. As detailed in Section 3.2, the parallel between this operator and the density matrix is crucial when formulating FTFT.

Consider a real scalar field $\phi(\mathbf{x})$ with an initial field configuration $|\phi_1(\mathbf{x})\rangle$ at t_1 and a final field configuration $|\phi_2(\mathbf{x})\rangle$ at t_2 . Then, it can be shown that the overlap can be expressed as a path integral,

$$\langle \phi_2(\mathbf{x}) | U(t_2, t_1) | \phi_1(\mathbf{x}) \rangle = \int \mathcal{D}\phi \exp \left\{ i \int_{t_1}^{t_2} dt \int d^3x \mathcal{L}[\phi] \right\}, \quad (3.2)$$

where $\int \mathcal{D}\phi$ represents an infinite product of integrals of intermediate ϕ field configurations at times between t_1 and t_2 , but where the boundary conditions are held fixed with $\phi_1(\mathbf{x})$ at t_1 and $\phi_2(\mathbf{x})$ at t_2 . Note that this is true as well for a time-dependent Hamiltonian. From this identity, it can be shown that the time-ordered average of field operators is given by

$$\langle T\phi(x_1)\phi(x_2)\dots\phi(x_n) \rangle = \frac{\int \mathcal{D}\phi \phi(x_1)\phi(x_2)\dots\phi(x_n) e^{iS[\phi]}}{\int \mathcal{D}\phi e^{iS[\phi]}}. \quad (3.3)$$

Note that on the left-hand side, the ϕ 's are field operators, and this is a quantum average, but on the right-hand side, the ϕ 's are simply functions. The action here is the integral of the Lagrangian over all spacetime,

$$S[\phi] = \int d^4x \mathcal{L}[\phi]. \quad (3.4)$$

Furthermore, a compact way to package a given quantum field theory is to introduce the generating functional,

$$Z[J] = \int \mathcal{D}\phi \exp \left\{ iS[\phi] + i \int d^4x J(x)\phi(x) \right\}. \quad (3.5)$$

This generating function is analogous to the partition function of statistical mechanics, and thus makes the parallel between zero-temperature QFT and FTFT more straightforward. As the name suggests, we can generate any time-ordered expected value from this through functional differentiation,

$$\langle T\phi(x_1) \dots \phi(x_n) \rangle = \frac{(-i)^n}{Z[J]} \left. \frac{\delta}{\delta J(x_1)} \dots \frac{\delta}{\delta J(x_n)} Z[J] \right|_{J=0}. \quad (3.6)$$

To do perturbation theory, we then separate the Lagrangian into a free part and an interacting part $\mathcal{L} = \mathcal{L}_{\text{free}} + \mathcal{L}_{\text{int}}$. The free part is usually exactly solvable as the propagator. Taylor expanding $Z[J]$ in powers of \mathcal{L}_{int} , one can then extract Feynman rules from the theory.

For fermions, the fields ψ and $\bar{\psi}$, as well as the sources η and $\bar{\eta}$, are Grassmann-valued, meaning that they anticommute. We can still define a generating functional and we get correlation functions similarly through functional differentiation. For example, in a theory with a fermion and an anti-fermion, we get

$$Z[\eta, \bar{\eta}] = \int \mathcal{D}\psi \mathcal{D}\bar{\psi} \exp \left\{ iS[\psi, \bar{\psi}] + i \int d^4x (\bar{\eta}\psi(x) + \bar{\psi}(x)\eta) \right\}, \quad (3.7)$$

and the time-ordered two-point function for the free Dirac theory is [21]

$$\langle T\psi(x_1)\bar{\psi}(x_2) \rangle = \frac{1}{Z[\eta, \bar{\eta}]} \left(-i \frac{\delta}{\delta \bar{\eta}(x_1)} \right) \left(i \frac{\delta}{\delta \eta(x_2)} \right) Z[\eta, \bar{\eta}] \Big|_{\eta, \bar{\eta}=0} = S_F(x_1 - x_2). \quad (3.8)$$

Finally, we usually use Fourier transform and work in momentum space to compute amplitudes and physical quantities.

3.2 Imaginary time formalism

We now turn to the imaginary-time formalism of FTFT. This formalism stems from applying statistical mechanics to quantum fields. In this section, I will first review some key facts from statistical mechanics, and express the partition function as a path integral. From this, it will be straightforward to make the parallel between quantum fields at zero-temperature and at finite temperature, and to point out how thermal corrections appear. Once again, I will work with a single bosonic scalar field to illustrate some key features of this formalism. This section is mostly based on Chapter 1 of Reference [22].

The density matrix of a system in equilibrium with an effective (time-independant) Hamiltonian \mathcal{H} is given by

$$\rho(\beta) = e^{-\beta\mathcal{H}}. \quad (3.9)$$

The effective Hamiltonian can be the actual Hamiltonian $\mathcal{H} = H$ in the case of a canonical ensemble, or it can be $\mathcal{H} = H - \mu N$ in the case of the grand canonical ensemble, for example. Note that N is a conserved charge and therefore commutes with the Hamiltonian, meaning that \mathcal{H} commutes with itself and can therefore really be treated as an effective Hamiltonian without any complication. In any case, the partition function is defined as:

$$Z(\beta) = \text{Tr}[\rho(\beta)]. \quad (3.10)$$

Furthermore, the thermal average of any observable Q is defined as

$$\langle Q(\mathbf{x}) \rangle_\beta = \frac{1}{Z(\beta)} \text{Tr}[\rho(\beta)Q(\mathbf{x})]. \quad (3.11)$$

We can rewrite the density matrix using the time evolution operator previously introduced,

$$\rho(\beta) = e^{-\beta\mathcal{H}} = e^{-i(-i\beta)\mathcal{H}} = U(-i\beta, 0). \quad (3.12)$$

This is mathematically equivalent to evolving a system through imaginary time, from 0 to $-i\beta$, hence the name of this formalism.

Consider a real (bosonic) scalar field ϕ . We use the configurations of this field as a complete basis of the theory, $1 = \int d\phi |\phi\rangle \langle \phi|$, to evaluate the trace and compute the partition function. We get

$$\begin{aligned} Z(\beta) &= \text{Tr}[U(-i\beta, 0)] \\ &= \int d\phi_1 \langle \phi_1(\mathbf{x}) | U(-i\beta, 0) | \phi_1(\mathbf{x}) \rangle \\ &= \int_{\text{periodic}} \mathcal{D}\phi e^{i\mathcal{S}[\phi]}. \end{aligned} \quad (3.13)$$

In the second line, the trace is taken over configurations labeled ϕ_1 simply to distinguish it from the ϕ that appears in the Hamiltonian. The last line makes use of Equation (3.2). However, the initial and final field configurations are the same in this case, so this path integral covers all paths that are periodic in imaginary time over a period of $i\beta$. Furthermore, the effective action is

$$\mathcal{S} = S - i\beta\mu N = \int_0^{-i\beta} dt \int d^3x \mathcal{L}[\phi, \partial\phi] - i\beta\mu N. \quad (3.14)$$

Here, the time integration is constrained to a finite interval on the imaginary axis. The contour is shown in Figure 3.1. This contrasts with zero-temperature QFT, where the time

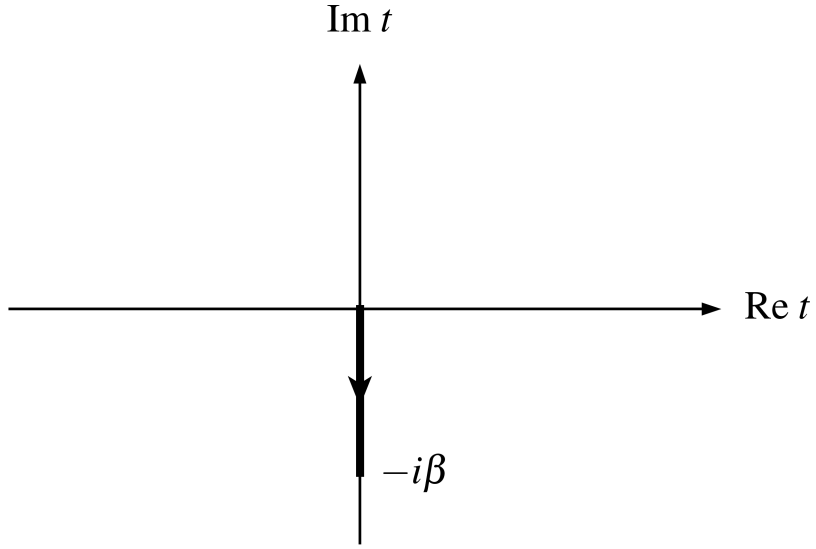


Figure 3.1: Schematic visualization of the contour for the path integral in the complex time plane. Adapted from [22].

integral covers all of real time.

It is common in this formalism to define a change of variable which amounts to performing a Wick rotation in the complex time plane:

$$\tau = it, \quad t = -i\tau. \quad (3.15)$$

In this picture, τ is real, and we are now in Euclidean space, with

$$Z(\beta) = \int_{per.} \mathcal{D}\phi e^{-S_E}, \quad (3.16)$$

where

$$S_E = S_E + \beta\mu N = \int_0^\beta d\tau \int d^3x \mathcal{L}[\phi, \partial\phi] + \beta\mu N. \quad (3.17)$$

Using this, it can be shown that we can express the average of an operator Q as

$$\langle Q \rangle_\beta = \frac{\int_{per.} \mathcal{D}\phi \ Q \ e^{\mathcal{S}_E}}{\int_{per.} \mathcal{D}\phi \ e^{\mathcal{S}_E}}. \quad (3.18)$$

Comparing this to Equation (3.3), the parallel to zero-temperature is clear. The partition function acts as the generating functional. We can once again separate the Lagrangian into a free part and an interaction part and do perturbation theory in powers of the interaction Lagrangian. Feynman rules in terms of momentum-conserving vertices and propagators can also be extracted directly from the Lagrangian. The key differences are the imaginary time (before Wick rotation), the finite contour for the time integration in the (effective) action, and the periodic nature of the path integral. As a consequence of this finite contour, when going to Fourier space, quantities computed with this formalism are only formally defined on discrete, purely imaginary frequencies $i\omega_n$, called Matsubara frequencies. One then has to proceed with the analytic continuation of these functions to evaluate them at real (physical) energies. The spatial integral of the action is real and continuous, so the spatial part of momentum is real and continuous as well, exactly like in zero-temperature QFT. For the purpose of perturbation theory, all of this means that the FTFT Feynman rules are exactly the same as the zero-temperature Feynman rules, except that the zeroth component of the momentum vector is now a discrete imaginary frequency. Energy integration should also be replaced with an infinite sum of discrete frequencies, i.e., we use the following replacement rule before Wick rotation:

$$\int \frac{d^4 p}{(2\pi)^4} M(p_0) \rightarrow \frac{i}{\beta} \sum_{n=-\infty}^{\infty} \int \frac{d^3 p}{(2\pi)^3} M(p_0 = i\omega_n). \quad (3.19)$$

The case of fermions is very similar, except that the boundary conditions change. For

fermions, the trace of a bosonic operator is roughly expressed as

$$\begin{aligned}\mathrm{Tr}\{A\} &= \mathrm{Tr}\{1A\} \sim \mathrm{Tr}\left[\int d\psi |\psi\rangle\langle\psi| A\right] \\ &= \mathrm{Tr}\left[\int d\psi \langle\psi| A |-\psi\rangle\right] = \int d\psi \langle\psi| A |-\psi\rangle.\end{aligned}\quad (3.20)$$

There are subtleties involving Grassmann integrals that affect the exact form of the identity operator. However, the essential point here is that there is an extra minus sign because fermionic states anticommute. Applied to the partition function, this clearly indicates that, for fermions, the path integral covers all paths with anti-periodic field configurations:

$$\begin{aligned}Z(\beta) &= \mathrm{Tr}[U(-i\beta, 0)] \\ &\sim \int d\psi_1 d\bar{\psi}_1 \langle\psi_1(\mathbf{x}), \bar{\psi}_1(\mathbf{x})| U(-i\beta, 0) |-\psi_1(\mathbf{x}), -\bar{\psi}_1(\mathbf{x})\rangle \\ &\sim \int_{anti-periodic} \mathcal{D}\psi \mathcal{D}\bar{\psi} e^{iS} = \int_{anti-periodic} \mathcal{D}\psi \mathcal{D}\bar{\psi} e^{-S_E}.\end{aligned}\quad (3.21)$$

Studying the propagator is a good way to demonstrate the (anti-)periodic boundary condition and, at the same time, to derive the exact form for the discrete Matsubara frequencies. Recall that a Heisenberg operator is defined as $A(t) = e^{i\mathcal{H}t} A_S e^{-i\mathcal{H}t}$ for any Schrodinger operator A_S . Then, a general two-point thermal average is, using Equation (3.11),

$$\begin{aligned}\langle A(t)B(t') \rangle &= \frac{1}{Z(\beta)} \mathrm{Tr}[\rho(\beta)A(t)B(t')] \\ &= \frac{1}{Z(\beta)} \mathrm{Tr}[e^{-\beta\mathcal{H}} A(t) e^{\beta\mathcal{H}} e^{-\beta\mathcal{H}} B(t')] \\ &= \frac{1}{Z(\beta)} \mathrm{Tr}[A(t + i\beta) e^{-\beta\mathcal{H}} B(t')] \\ &= \frac{1}{Z(\beta)} \mathrm{Tr}[e^{-\beta\mathcal{H}} B(t') A(t + i\beta)] \\ &= \langle B(t') A(t + i\beta) \rangle.\end{aligned}\quad (3.22)$$

In the second line, we inserted $1 = e^{\beta\mathcal{H}}e^{-\beta\mathcal{H}}$ in between the operators. In the third line, we used the fact that the density matrix is equivalent to the time-evolution operator but through imaginary time. Finally, we used the cyclicity of the trace to get the final result. This identity is called the Kubo–Martin–Schwinger (KMS) condition, and is equivalent to the fact that the system is in thermal equilibrium. The two-point Green’s function for a fermionic or bosonic field ϕ is a τ -ordered average,

$$\mathcal{G}(\tau - \tau') = \langle T_\tau \phi(\tau) \phi^\dagger(\tau') \rangle. \quad (3.23)$$

To be general, we could have written $\mathcal{G}(\tau, \tau')$, but this Green’s function only depends on the difference between the imaginary times. Because each time variable lies in $0 \leq \tau, \tau' \leq \beta$, we have $-\beta \leq \tau - \tau' \leq \beta$. Then, for $-\tau < 0$, we can use the KMS condition to write:

$$\begin{aligned} \mathcal{G}(-\tau) &= \langle \phi(0) \phi^\dagger(\tau) \rangle \\ &= \pm \langle \phi^\dagger(\tau) \phi(0) \rangle \\ &= \pm \langle \phi(\beta) \phi^\dagger(\tau) \rangle \\ &= \pm \mathcal{G}(-\tau + \beta). \end{aligned} \quad (3.24)$$

The second line comes from the commuting (+) and anticommuting (−) properties of bosonic and fermionic fields, respectively. The third line comes from the KMS condition. This two-point Green’s function is defined on a finite interval, and the Fourier transform thus involves discrete frequencies,

$$\mathcal{G}(\tau) = \frac{1}{\beta} \sum_n e^{-i\omega_n \tau} \mathcal{G}(\omega_n), \quad (3.25a)$$

$$\mathcal{G}(\omega_n) = \frac{1}{2} \int_{-\beta}^{\beta} d\tau e^{i\omega_n \tau} \mathcal{G}(\tau), \quad (3.25b)$$

where $\omega_n = n\pi/\beta$, $n = 0, \pm 1, \pm 2, \dots$. However, because of the (anti-)periodic condition, only the even frequencies survive for bosons, and odd frequencies for fermions. Indeed:

$$\begin{aligned}
 \mathcal{G}(\omega_n) &= \frac{1}{2} \int_{-\beta}^0 d\tau e^{i\omega_n \tau} \mathcal{G}(\tau) + \frac{1}{2} \int_0^\beta d\tau e^{i\omega_n \tau} \mathcal{G}(\tau) \\
 &= \pm \frac{1}{2} \int_{-\beta}^0 d\tau e^{i\omega_n \tau} \mathcal{G}(\tau + \beta) + \frac{1}{2} \int_0^\beta d\tau e^{i\omega_n \tau} \mathcal{G}(\tau) \\
 &= \pm \frac{1}{2} \int_0^\beta d\tilde{\tau} e^{i\omega_n (\tilde{\tau} - \beta)} \mathcal{G}(\tilde{\tau}) + \frac{1}{2} \int_0^\beta d\tau e^{i\omega_n \tau} \mathcal{G}(\tau) \\
 &= \frac{1}{2} (1 \pm e^{-i\omega_n \beta}) \int_0^\beta d\tau e^{i\omega_n \tau} \mathcal{G}(\tau) \\
 &= \frac{1}{2} (1 \pm (-1)^n) \int_0^\beta d\tau e^{i\omega_n \tau} \mathcal{G}(\tau),
 \end{aligned} \tag{3.26}$$

where the crucial step is the second line is making use of the KMS condition for the propagator. From this, we clearly see that the Matsubara frequencies are restricted to

$$\omega_n = \begin{cases} \frac{2n\pi}{\beta} & \text{for bosons,} \\ \frac{(2n+1)\pi}{\beta} & \text{for fermions.} \end{cases} \tag{3.27}$$

These are the Matsubara frequencies when there is no chemical potential. A chemical potential creates a shift in the Matsubara frequencies [23]. For example, take a fermionic Dirac field. Then the conserved current is $J^\mu = \bar{\psi} \gamma^\mu \psi$, and, from Noether's theorem, the conserved charge is

$$N = \int d^3x J^0 = \int d^3x \bar{\psi} \gamma^0 \psi. \tag{3.28}$$

The effective action before Wick rotation is

$$\mathcal{S} = S - i\beta\mu N = \int_0^{-i\beta} dt (L + \mu N) = \int_0^{-i\beta} dt \int d^3x \bar{\psi} (i\gamma^0(\partial_t - i\mu) - i\gamma^i \partial_i - m) \psi. \tag{3.29}$$

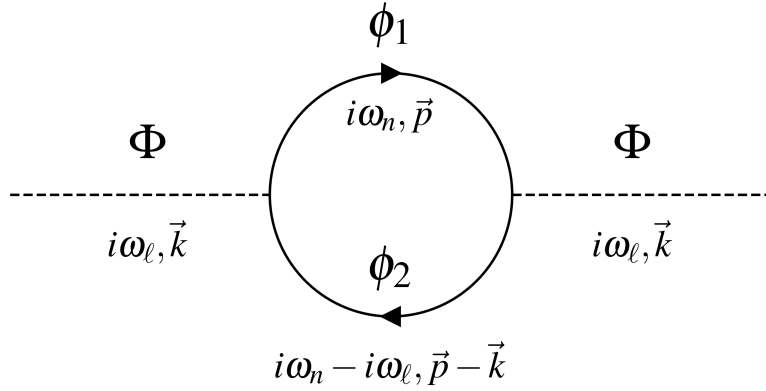


Figure 3.2: Feynman diagram of the boson self-energy in our toy model. Adapted from [24].

Then, going to Fourier space, we clearly see that the Matsubara frequencies shift,

$$\partial_t - i\mu = i\partial_\tau - i\mu \rightarrow \omega_n - i\mu. \quad (3.30)$$

Equivalently,

$$p_0 = i\omega_n \rightarrow p_0 = i\omega_n + \mu. \quad (3.31)$$

It can be shown that this shift in p_0 happens for bosons with a chemical potential as well.

3.3 Self-energies in imaginary-time formalism

Self-energies are one of the key objects that we want to compute in FTFT. They inform us about the dispersion of particles in a medium and provide all the thermal corrections to propagators. In this section, I will show some self-energy computations with a toy model that includes only bosonic scalar fields, in order to illustrate some key elements and properties of self-energies in FTFT. This section is mostly based on References [22] and [24].

Consider a theory with a three-point interaction,

$$\mathcal{L} \supset g\phi_1\phi_2\Phi. \quad (3.32)$$

We aim to compute the self-energy of a real scalar field Φ at one loop, represented in the Feynman diagram of Figure 3.2. The particles in the loop, ϕ_1 and ϕ_2 , are also two scalar fields. Defining $E_1 = \sqrt{p^2 + m_1^2}$ and $E_2 = \sqrt{(\mathbf{p} - \mathbf{k})^2 + m_1^2}$, we compute the self-energy prior to Wick rotation:

$$\begin{aligned}\Pi(i\omega_\ell, k) &= -g^2 T \sum_n \int d^3 p \frac{1}{(i\omega_n)^2 - p^2 - m_1^2} \frac{1}{(i\omega_n - i\omega_\ell)^2 - (\mathbf{p} - \mathbf{k})^2 - m_2^2} \\ &= -g^2 T \sum_n \int d^3 p \frac{1}{2E_1 2E_2} \left(\frac{1}{i\omega_n - E_1} - \frac{1}{i\omega_n + E_1} \right) \\ &\quad \times \left(\frac{1}{i\omega_n - i\omega_\ell - E_2} - \frac{1}{i\omega_n - i\omega_\ell + E_2} \right) \\ &= -g^2 T \frac{1}{(2\pi iT)^2} \sum_n \int d^3 p \frac{1}{2E_1 2E_2} \left(\frac{1}{n + iE_1/2\pi T} - \frac{1}{n - iE_1/2\pi T} \right) \quad (3.33) \\ &\quad \times \left(\frac{1}{n + i(E_2 + i\omega_\ell)/2\pi T} - \frac{1}{n - i(E_2 - i\omega_\ell)/2\pi T} \right),\end{aligned}$$

where

$$d^n p \equiv \frac{d^n p}{(2\pi)^n} \quad (3.34)$$

We then use the following identity to compute the infinite sum:

$$\sum_n \frac{1}{n + ix} \frac{1}{n + iy} = \frac{\pi}{x - y} (\coth(\pi x) - \coth(\pi y)). \quad (3.35)$$

This identity is a special case that can be generalized using the residue theorem (see Section 4.1.1 for more details). In general, summing over bosonic Matsubara frequencies results in coth functions, while summing over fermionic Matsubara frequencies results in tanh functions. Then, one can always use the following identities:

$$\coth(z) = -\coth(-z) = 1 + 2f_{\text{BE}}(2z), \quad (3.36a)$$

$$\tanh(z) = -\tanh(-z) = 1 - 2f_{\text{FD}}(2z), \quad (3.36b)$$

where,

$$f_{\text{BE}}(z) = \frac{1}{e^z - 1}, \quad f_{\text{FD}}(z) = \frac{1}{e^z + 1}. \quad (3.37)$$

Therefore, the frequency sum always brings out the appropriate thermal distribution for a given particle statistics. Furthermore, we use the following shift identities:

$$\tanh(z) = \tanh(z + \ell\pi i) \quad \ell \in \mathbb{Z}, \quad (3.38a)$$

$$\coth(z) = \coth(z + \ell\pi i) \quad \ell \in \mathbb{Z}, \quad (3.38b)$$

$$\coth(z) = \tanh(z + (2\ell + 1)\pi i/2) \quad \ell \in \mathbb{Z}. \quad (3.38c)$$

With these, we can get rid of imaginary frequencies in the thermal distributions. For example,

$$\coth\left(\frac{E_2 + i\omega_\ell}{2T}\right) = \coth\left(\frac{E_2}{2T}\right) = 1 + 2f_{\text{BE}}(E_2/T). \quad (3.39)$$

We finally get:

$$\begin{aligned} \Pi(i\omega_\ell, k) = g^2 \int d^3 p \frac{1}{2E_1 2E_2} & \left(\frac{1 + f_1 + f_2}{i\omega_\ell - E_1 - E_2} + \frac{f_1 - f_2}{i\omega_\ell + E_1 - E_2} \right. \\ & \left. + \frac{f_2 - f_1}{i\omega_\ell - E_1 + E_2} - \frac{1 + f_1 + f_2}{i\omega_\ell + E_1 + E_2} \right), \end{aligned} \quad (3.40)$$

where f_i is short for $f_{\text{BE}}(E_i/T)$. The fact that the Bose-Einstein distributions appear is not a coincidence. This one-loop computation in FTFT accounts for the fact that there are not only virtual particles in the loop, but also actual particles from the medium following a thermal distribution.

Note that the identity (3.38c) is crucial for cases where there are different types of particles in a loop. For example, take a fermion self-energy at one loop, represented by the diagram of Figure 3.3. We are summing over bosonic frequencies ω_n^B , so coth functions appear. However, the fermion propagator in the loop still gives rise to terms proportional to the appropriate

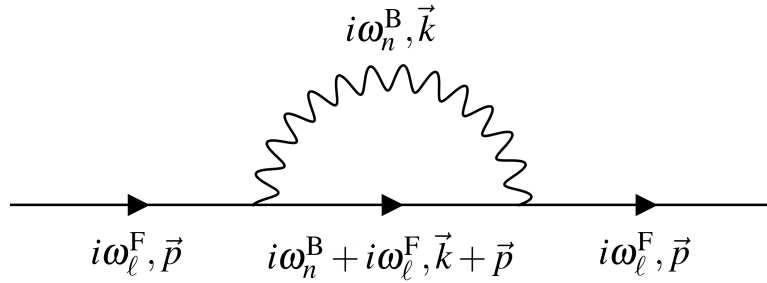


Figure 3.3: Feynman diagram of an example fermion self-energy.

thermal distribution:

$$\coth\left(\frac{E_{p+k} + i\omega_\ell^F}{2T}\right) = \tanh\left(\frac{E_{p+k}}{2T}\right) = 1 - 2f_{\text{FD}}(E_{p+k}/T). \quad (3.41)$$

3.4 The imaginary part of self-energies

This section is based on References [22] and [24] as well. We can extend the self-energy to a function on the full complex ω plane. With this, we can evaluate it at real values of the energies. The analytic continuation is Hermitian analytic,

$$\Pi(\omega)^* = \Pi(\omega^*). \quad (3.42)$$

We can see from this condition that the imaginary part of the self-energy evaluated at any complex energy $\tilde{\omega} = \omega + i\eta$ with ω real and η real and positive is

$$\begin{aligned} \text{Im } \Pi(\tilde{\omega}) &= \frac{1}{2i} [\Pi(\tilde{\omega}) - \Pi(\tilde{\omega})^*] \\ &= \frac{1}{2i} [\Pi(\tilde{\omega}) - \Pi(\tilde{\omega}^*)] \\ \text{Im } \Pi(\omega + i\eta) &= \frac{1}{2i} [\Pi(\omega + i\eta) - \Pi(\omega - i\eta)]. \end{aligned} \quad (3.43)$$

Taking the limit of $\eta \rightarrow 0$, there are discontinuities along the real axis which give us the imaginary part of the self-energy for a real ω :

$$\text{Disc}\Pi(\omega) = \lim_{\eta \rightarrow 0} [\Pi(\omega + i\eta) - \Pi(\omega - i\eta)] = 2i \text{Im } \Pi(\omega). \quad (3.44)$$

In our toy model, using Equation (3.40) with $i\omega_\ell \rightarrow \tilde{\omega}$, we see that $\text{Disc}\Pi(\omega)$ contains terms in the integral proportional to

$$\frac{1}{\omega + i\eta - E_1 - E_2} - \frac{1}{\omega - i\eta - E_1 - E_2}. \quad (3.45)$$

Using the following identity:

$$\frac{1}{x + i\eta} - \frac{1}{x - i\eta} \rightarrow -2\pi i\delta(x) \quad \text{as } \eta \rightarrow 0, \quad (3.46)$$

we get the following replacement rule in the integral to compute the discontinuity:

$$\frac{1}{\omega - E_1 - E_2} \rightarrow -2\pi i\delta(\omega - E_1 - E_2). \quad (3.47)$$

Therefore, we get, from Equation (3.40),

$$\begin{aligned} \text{Im } \Pi(\omega, \mathbf{k}) = -\pi g^2 \int d^3 p \frac{1}{2E_1 2E_2} & \left\{ [(1 + f_1)(1 + f_2) - f_1 f_2] \delta(\omega - E_1 - E_2) \right. \\ & + [f_1(1 + f_2) - f_2(1 + f_1)] \delta(\omega + E_1 - E_2) \\ & + [f_2(1 + f_1) - f_1(1 + f_2)] \delta(\omega - E_1 + E_2) \\ & \left. + [f_1 f_2 - (1 + f_1)(1 + f_2)] \delta(\omega + E_1 + E_2) \right\}. \end{aligned} \quad (3.48)$$

The integration measure is defined in Equation (3.34). Terms proportional to $f_1 f_2$ have been added and subtracted to better see the physical interpretation. Before we discuss that, we

do a few more steps. Here, $E_2^2 = (\mathbf{p} - \mathbf{k})^2 + m_2^2$, but since we are integrating over \mathbf{p} , we can change variables for $\mathbf{p} \rightarrow -\mathbf{p}$ in the second and fourth terms. We rewrite $\mathbf{p} \rightarrow \mathbf{p}_1$. Furthermore, we can use identities such as

$$1 = \int d^3 p_2 (2\pi)^3 \delta^3(\mathbf{k} - \mathbf{p}_1 - \mathbf{p}_2). \quad (3.49)$$

for the first term, and equivalent ones for the other terms, and write $E_2^2 = p_2^2 + m_2^2$ in every case. Finally, we rewrite the coupling as $g^2 = |\mathcal{M}|^2$ at tree-level for various 3-point processes of this theory. We get

$$\begin{aligned} \text{Im } \Pi = & -\frac{1}{2} \int \frac{d^3 p_1}{2E_1} \frac{d^3 p_2}{2E_2} (2\pi)^4 \times \\ & \left\{ [|\mathcal{M}_{\Phi \rightarrow \phi_1 \phi_2}|^2 (1 + f_1)(1 + f_2) - |\mathcal{M}_{\phi_1 \phi_2 \rightarrow \Phi}|^2 f_1 f_2] \delta^4(k - p_1 - p_2) \right. \\ & + [|\mathcal{M}_{\Phi \phi_1 \rightarrow \phi_2}|^2 f_1 (1 + f_2) - |\mathcal{M}_{\phi_2 \rightarrow \Phi \phi_1}|^2 f_2 (1 + f_1)] \delta^4(k + p_1 - p_2) \\ & + [|\mathcal{M}_{\Phi \phi_2 \rightarrow \phi_1}|^2 f_2 (1 + f_1) - |\mathcal{M}_{\phi_1 \rightarrow \Phi \phi_2}|^2 f_1 (1 + f_2)] \delta^4(k - p_1 + p_2) \\ & \left. + [|\mathcal{M}_{\Phi \phi_1 \phi_2 \rightarrow 0}|^2 f_1 f_2 - |\mathcal{M}_{0 \rightarrow \Phi \phi_1 \phi_2}|^2 (1 + f_1)(1 + f_2)] \delta^4(k + p_1 + p_2) \right\}. \end{aligned} \quad (3.50)$$

This form brings out the physical interpretation and can be generalized to any theory. The first term in the integral is the probability of a $\Phi \rightarrow \phi_1 \phi_2$ decay weighted with the appropriate stimulated emission factor for bosons $(1 + f_1)(1 + f_2)$, minus the probability of the inverse decay weighed with the appropriate statistical factors $f_1 f_2$ for boson absorption. Each one of the other three terms has a similar physical interpretation. We also see that the imaginary part can be expressed in terms of cutting rules, similar to the optical theorem in zero-temperature QFT. All the processes involved here are the result of cutting the self-energy loop in half, with loop particles put on shell.

This generalizes to arbitrary self-energy calculations. Also note that for fermions, the identity (3.36b) has a minus sign compared to the boson identity (3.36a). As a result,

fermions are weighted by the appropriate Pauli blocking factors ($1 - f_{\text{FD}}$) instead of stimulated emission. Finally, the cutting rules apply at any loop order. In general, the absorption and production rates for a particle Φ (boson or fermion) for which we are computing the self-energy are given by

$$\Gamma^A(\omega, T) = \frac{1}{2\omega} \sum_{i,f} \int d\tilde{\Omega}_{if} \langle |\mathcal{M}|_{\Phi+i \rightarrow f}^2 \rangle_{\text{spins}} \prod_{a \in \{i\}} f_a \prod_{b \in \{f\}} (1 \pm f_b), \quad (3.51\text{a})$$

$$\Gamma^P(\omega, T) = \frac{1}{2\omega} \sum_{i,f} \int d\tilde{\Omega}_{fi} \langle |\mathcal{M}|_{i \rightarrow f+\Phi}^2 \rangle_{\text{spins}} \prod_{a \in \{i\}} f_a \prod_{b \in \{f\}} (1 \pm f_b), \quad (3.51\text{b})$$

with a (+) sign if particle b is a bosons and a (−) if it's a fermions, and where

$$d\Pi = \frac{g}{2E} \frac{d^3 p}{(2\pi)^3} = g \frac{d^3 p}{2E}, \quad (3.52\text{a})$$

$$d\tilde{\Omega}_{if} = (2\pi)^4 \delta^{(4)} \left(k^\mu + \sum_{a \in \{i\}} p_a^\mu - \sum_{b \in \{f\}} p_b^\mu \right) \left(\prod_{a \in \{i\}} d\Pi_a \right) \left(\prod_{b \in \{f\}} d\Pi_b \right), \quad (3.52\text{b})$$

with k^μ the momentum of the Φ particle. Then, the imaginary part is given by

$$\text{Im } \Pi = -\omega(\Gamma^A \pm \Gamma^P), \quad (3.53)$$

with a (−) sign if Φ is a bosons and a (+) sign if it's a fermions. This holds for any theory. Interestingly, we can go further in the special case of CP invariant theories, where the matrix elements are the same for a process and its reverse. In this case, using detailed balance, one can show that

$$\Gamma^A = e^{\omega/T} \Gamma^P. \quad (3.54)$$

Therefore,

$$\text{Im } \Pi = -\omega(\Gamma^A \pm \Gamma^P) = -\omega(e^{\omega/T} \pm 1) \Gamma^P = -\omega(1 \pm e^{-\omega/T}) \Gamma^A. \quad (3.55)$$

In terms of Φ 's phase space density,

$$\text{Im } \Pi = -\frac{\omega}{f_\Phi(\omega)} \Gamma^P, \quad (3.56)$$

which is valid for bosons and fermions.

The function $\Gamma = \Gamma^A \pm \Gamma^P$ can be interpreted as a rate to achieve equilibrium. Indeed, take the distribution of Φ to be $f(\omega, t)$, which is initially close to, but not in, equilibrium. This function satisfies

$$\frac{df}{dt} = -f\Gamma^A + (1 + \sigma f)\Gamma^P, \quad (3.57)$$

where the first term is just the absorption rate with the appropriate statistical factor, and the second one is the production rate, also with appropriate stimulated emission ($\sigma = 1$) or Pauli blockade ($\sigma = -1$) depending on the particle type. Because it is close to equilibrium, we can approximate that the $\Gamma_{A,D}$ are independent of f (and of t), so we can write:

$$\frac{df}{dt} \left(f - \frac{\Gamma^P}{\Gamma^A - \sigma\Gamma^P} \right) = -(\Gamma^A - \sigma\Gamma^P) \left(f - \frac{\Gamma^P}{\Gamma^A - \sigma\Gamma^P} \right). \quad (3.58)$$

The solution is clearly an exponential,

$$f = \frac{\Gamma^P}{\Gamma^A - \sigma\Gamma^P} + c(\omega)e^{-(\Gamma^A - \sigma\Gamma^P)t}, \quad (3.59)$$

Using detailed balance, and defining $\Gamma(\omega) = (\Gamma^A - \sigma\Gamma^P)$,

$$f = \frac{1}{e^{\omega/T} - \sigma} + c(\omega)e^{-\Gamma(\omega)t}. \quad (3.60)$$

As $t \rightarrow \infty$, we see that $f \rightarrow 1/(e^{\omega/T} - \sigma)$, the equilibrium density, at the rate given by the imaginary part of the self-energy, $\Gamma(\omega) = -\text{Im } \Pi(\omega)/\omega$.

3.5 Forward scattering

I will now discuss briefly another formalism based on kinetic theory to find particle self-energies. It turns out that, at one loop, this formalism is equivalent to the imaginary-time formalism, at least for the photon self-energy. This formalism is more physically transparent, and helps with the physical interpretation of the self-energy. I will link the FTFT expression of the photon self-energy with forward scattering explicitly in Chapter 4. This section is based on Reference [2].

Consider a scalar field plane wave scattering off another particle at $r = 0$. Asymptotically,

$$\Phi(\mathbf{r}, t) \propto e^{-i\omega t} \left(e^{i\mathbf{k} \cdot \mathbf{r}} + \tilde{A}(\omega, \theta) \frac{e^{ikr}}{r} \right) \quad (3.61)$$

where $\tilde{A}(\omega, \theta)$ is the scattering amplitude, i.e., $d\sigma/d\Omega = |\tilde{A}(\omega, \theta)|^2$. In the forward direction, the scattered waves add up coherently and end up causing a phase shift in the wave, in other words, causing refraction. It can be shown that the index of refraction $n = k/\omega$ is given by

$$n^2 = 1 + \frac{4\pi}{k^2} n_\phi A(\omega), \quad (3.62)$$

where n_ϕ is the number density of scatterers ϕ , and $A(\omega)$ is the forward scattering amplitude $\tilde{A}(\omega, 0)$. The amplitude generally depends on the scatterer's momentum \mathbf{p} , and these scatterers actually follow a thermal distribution function $f(\mathbf{p})$, i.e. the Bose-Einstein or the Fermi-Dirac distribution in equilibrium. The index of refraction is then an appropriate average over the scatterers momentum. Allowing for multiple possible scatterers ϕ_i , we get

$$n^2 = 1 + \frac{4\pi}{k^2} \sum_i \int d^3 p \ f_i(\mathbf{p}) \ A_i(\omega, \mathbf{p}). \quad (3.63)$$

Rewriting this as a dispersion relation, we get

$$\omega^2 - k^2 = -\frac{4\pi}{n^2} \sum_i \int d^3p f_i(\mathbf{p}) A_i(\omega, \mathbf{p}). \quad (3.64)$$

In QFT, the amplitude is proportional to the matrix elements \mathcal{M} of the scattering. This is similar in structure to the self-energy derived in Section 3.3, see Equation (3.40). The parallel between FTFT and forward scattering is developed in more detail in Section 4.1.2 for the case of the photon self-energy at one loop.

Chapter 4

Photon self-energy on shell

The photon self-energy is an integral that can only be computed numerically because of the presence of the Fermi-Dirac distributions inside the integral. The computation can be made simpler if one assumes that the photons are on shell. Mathematically, the approximation is the same if one assumes that the photon momentum is soft. Furthermore, analytic approximations for both the longitudinal and the transverse self-energy have been published by Braaten and Segel in 1993 [1]. These can be used to describe the dispersion of actual photons propagating in the medium. They can also be used for off-shell photons with soft momentum — for example, to describe screening effects of static electric fields [2]. In this chapter, I will present details of the computation of the on-shell photon self-energy. In the first section, I will use the FTFT formalism presented in Chapter 3 to derive the general expression for the one-loop self-energy. Then, in the second section, I will review in detail the computation leading to the analytic approximation from Reference [1], assuming that the photons are on shell. While we label these expressions as on shell in the current chapter, one should keep in mind that they are also valid in the soft photon momentum limit.

4.1 One-loop photon self-energy integral

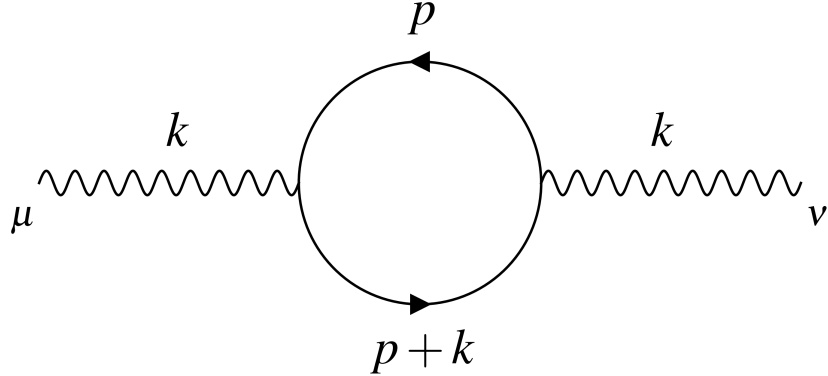


Figure 4.1: One-loop Feynman diagram of the photon self-energy.

The only one-loop diagram for the photon self-energy is presented in Figure 4.1. Using FTFT Feynman rules, this yields the following expression:

$$-i\Pi^{\mu\nu} = iT \sum_{n=-\infty}^{\infty} \int \frac{d^3 p}{(2\pi)^3} (-1) \frac{\text{Tr}[i(\not{p} + m)(-ie)\gamma^\mu i(\not{k} + m)(-ie)\gamma^\nu]}{(p^2 - m^2)((p+k)^2 - m^2)}, \quad (4.1)$$

where m is the mass of the electron, which can include thermal corrections, and where we are still using the Minkowski metric, i.e., we didn't proceed with Wick rotation. Therefore, $k_0 = i\omega_\ell$ and $p_0 = i\omega_n + \mu$, where ω_ℓ and ω_n are the Matsubara frequencies for bosons and fermions, respectively, and where μ is the chemical potential of the electrons. We can rewrite this as

$$\begin{aligned} \Pi^{\mu\nu} &= e^2 T \sum_n \int \frac{d^3 p}{(2\pi)^3} \frac{\text{Tr}[(\not{p} + m)\gamma^\mu (\not{k} + m)\gamma^\nu]}{(p^2 - m^2)((p+k)^2 - m^2)} \\ &= 4\pi\alpha \int \frac{d^3 p}{(2\pi)^3} T \sum_n f(p_0 = i\omega_n + \mu), \end{aligned} \quad (4.2)$$

where we define the following:

$$f(p_0) = \frac{\text{Tr}(p)}{(p^2 - m^2)((p+k)^2 - m^2)}, \quad \text{Tr}(p) = \text{Tr}[(\not{p} + m)\gamma^\mu (\not{k} + m)\gamma^\nu]. \quad (4.3)$$

4.1.1 Residue theorem exchange of poles trick

As stated in Chapter 3, the Matsubara frequency sums in loop computations generally give rise to the appropriate thermal distribution functions. In this section, I present a trick using the residue theorem which explains this fact. I present it in detail for the specific diagram I am computing, but this can be generalized straightforwardly [22, 23, 25].

To compute the infinite sum over the Matsubara frequencies, we use the fact that these can be related to the poles of the tanh function for fermions (or of the coth function for bosons). Indeed,

$$\coth(z) \text{ has simple poles at } z = in\pi, \quad n \in \mathbb{Z}, \quad \text{with residue 1,} \quad (4.4a)$$

$$\tanh(z) \text{ has simple poles at } z = i(2n+1)\pi/2, \quad n \in \mathbb{Z}, \quad \text{with residue 1.} \quad (4.4b)$$

In other words, $\coth(z)$ has poles at $i\omega_n^B/2T$ and $\tanh(z)$ has poles at $i\omega_n^F/2T$. Thus, whatever the function form of $f(p_0)$, if it has no poles on the imaginary axis along $\text{Re}(p_0) = \mu$, then this infinite sum is essentially the sum of all residues of the product of f with the appropriate tanh function. This residue sum can be transformed into a contour integral:

$$\begin{aligned} T \sum_n f(p_0 = i\omega_n + \mu) &= T \sum_{\substack{\text{residues at} \\ \text{poles of tanh}}} f(p_0) \frac{1}{2T} \tanh\left(\frac{p_0 - \mu}{2T}\right) \\ &= \frac{1}{2\pi i} \oint_C dp_0 f(p_0) \frac{1}{2} \tanh\left(\frac{p_0 - \mu}{2T}\right), \end{aligned} \quad (4.5)$$

where the contour C is schematically represented on the left of Figure 4.2, extending to infinity in the imaginary direction. The infinitesimally small sides at $\mu \pm i\infty$ do not contribute to the integral. Therefore, provided f goes to zero at infinity, we can instead close the contour with big semicircles at $\pm\infty$ which do not contribute to the integral either. The tanh (or coth) function does not have any other pole, so this new, equivalent contour C' instead picks up the poles of f [25]. For a general Feynman diagram, these are the poles of the propagators

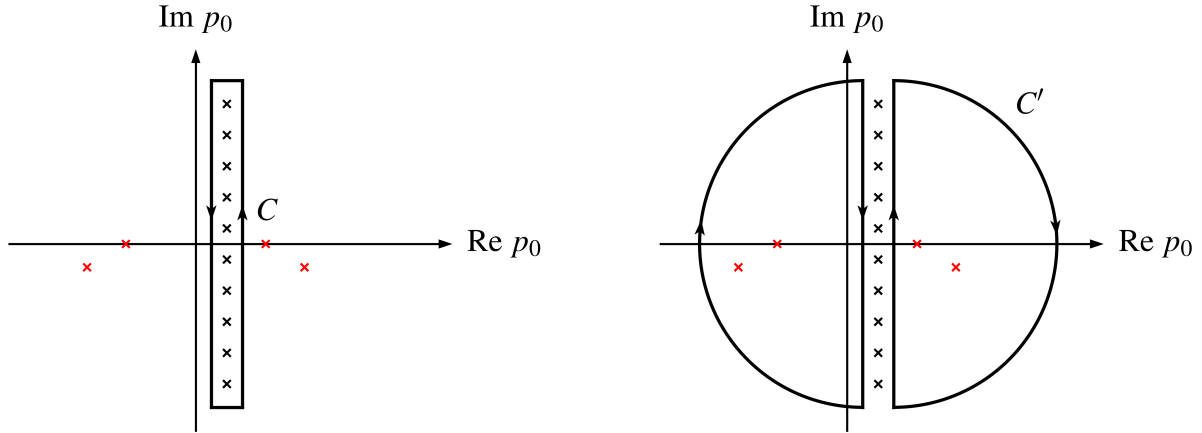


Figure 4.2: Schematic visualization of the contours in the complex p_0 plane that are involved in the “exchange of poles” trick. On the left, the contour C is infinitesimally narrow in the real direction and extends to infinity in the imaginary direction; it encloses an infinite number of poles (the poles of \tanh at $p_0 = i\omega_n + \mu$). On the right, the semicircles of C' are closed at infinity and the contour now simply encloses the four poles of the fermion propagators.

from the loop. This is schematically represented on the right side of Figure 4.2. It leads to:

$$\begin{aligned} T \sum_n f(p_0 = i\omega_n + \mu) &= \frac{1}{2\pi i} \oint_{C'} dp_0 f(p_0) \frac{1}{2} \tanh \left(\frac{p_0 - \mu}{2T} \right) \\ &= - \sum_{\substack{\text{residues at} \\ \text{poles of } f}} f(p_0) \frac{1}{2} \tanh \left(\frac{p_0 - \mu}{2T} \right). \end{aligned} \quad (4.6)$$

This is quite general, and explains why the appropriate function, \coth or \tanh , always appears when doing the frequency sum for bosons and fermions, respectively. In our specific case, f has four simple poles. We can write

$$f(p_0) = \frac{\text{Tr}(p)}{(p_0 + E_p)(p_0 - E_p)(p_0 + k_0 + E_{p+k})(p_0 + k_0 - E_{p+k})}, \quad (4.7)$$

where $E_q = \sqrt{\mathbf{q}^2 + m^2} > 0$. The trace in the numerator has no poles. Evaluating the

residues, we get

$$\begin{aligned}
 -2T \sum_n f(p_0 = i\omega_n + \mu) = & -\frac{1}{2E_p} \frac{\text{Tr}(p)}{((p+k)^2 - m^2)} \tanh\left(\frac{p_0 - \mu}{2T}\right) \Big|_{p_0=-E_p} \\
 & + \frac{1}{2E_p} \frac{\text{Tr}(p)}{((p+k)^2 - m^2)} \tanh\left(\frac{p_0 - \mu}{2T}\right) \Big|_{p_0=E_p} \\
 & - \frac{1}{2E_{p+k}} \frac{\text{Tr}(p)}{(p^2 - m^2)} \tanh\left(\frac{p_0 - \mu}{2T}\right) \Big|_{p_0+k_0=-E_{p+k}} \\
 & + \frac{1}{2E_{p+k}} \frac{\text{Tr}(p)}{(p^2 - m^2)} \tanh\left(\frac{p_0 - \mu}{2T}\right) \Big|_{p_0+k_0=E_{p+k}}.
 \end{aligned} \tag{4.8}$$

To be very explicit, now that the frequency sum is done, the values of p_0 on the right-hand side are not Matsubara frequencies anymore, but are evaluated at specific values for each of the four terms.

4.1.2 Equivalence with forward scattering

It is possible to write the one-loop integral as forward scattering. This can help bring about a physical interpretation of the in-medium self-energy. We use the fact that the tanh function is odd, $\tanh(z) = -\tanh(-z)$. We also use its periodicity, Equation (3.38a), combined with the fact that that k_0 is quantized with boson Matsubara frequencies, and we get

$$\begin{aligned}
 -2T \sum_n f(p_0 = i\omega_n + \mu) = & \frac{1}{2E_p} \frac{\text{Tr}(p)}{((p+k)^2 - m^2)} \tanh\left(\frac{-p_0 + \mu}{2T}\right) \Big|_{p_0=-E_p} \\
 & + \frac{1}{2E_p} \frac{\text{Tr}(p)}{((p+k)^2 - m^2)} \tanh\left(\frac{p_0 - \mu}{2T}\right) \Big|_{p_0=E_p} \\
 & + \frac{1}{2E_{p+k}} \frac{\text{Tr}(p)}{(p^2 - m^2)} \tanh\left(\frac{-p_0 - k_0 + \mu}{2T}\right) \Big|_{p_0+k_0=-E_{p+k}} \\
 & + \frac{1}{2E_{p+k}} \frac{\text{Tr}(p)}{(p^2 - m^2)} \tanh\left(\frac{p_0 + k_0 - \mu}{2T}\right) \Big|_{p_0+k_0=E_{p+k}}.
 \end{aligned} \tag{4.9}$$

Then, we use this identity,

$$\frac{1}{2E_p} \delta(p_0 \mp E_p) = \theta(\pm p_0) \delta(p^2 - m^2), \quad (4.10)$$

to get, for the full self-energy:

$$\begin{aligned} \Pi^{\mu\nu} = & -4\pi\alpha \int \frac{d^3p}{(2\pi)^3} \int \frac{dp_0}{2} \left[\theta(-p_0) \delta(p^2 - m^2) \frac{\text{Tr}(p)}{((p+k)^2 - m^2)} \tanh\left(\frac{-p_0 + \mu}{2T}\right) \right. \\ & + \theta(p_0) \delta(p^2 - m^2) \frac{\text{Tr}(p)}{((p+k)^2 - m^2)} \tanh\left(\frac{p_0 - \mu}{2T}\right) \\ & + \theta(-p_0 - k_0) \delta((p+k)^2 - m^2) \frac{\text{Tr}(p)}{(p^2 - m^2)} \tanh\left(\frac{-p_0 - k_0 + \mu}{2T}\right) \\ & \left. + \theta(p_0 + k_0) \delta((p+k)^2 - m^2) \frac{\text{Tr}(p)}{(p^2 - m^2)} \tanh\left(\frac{p_0 + k_0 - \mu}{2T}\right) \right]. \end{aligned} \quad (4.11)$$

We now shift the integration variables for the last two terms $p \rightarrow p - k$, and then reverse the sign of these integration variables in the first and third terms, $p \rightarrow -p$. This yields

$$\begin{aligned} \Pi^{\mu\nu} = & -4\pi\alpha \int \frac{d^3p}{(2\pi)^3} \int \frac{dp_0}{2} \left[\theta(p_0) \delta(p^2 - m^2) \frac{\text{Tr}(-p)}{((p-k)^2 - m^2)} \tanh\left(\frac{p_0 + \mu}{2T}\right) \right. \\ & + \theta(p_0) \delta(p^2 - m^2) \frac{\text{Tr}(p)}{((p+k)^2 - m^2)} \tanh\left(\frac{p_0 - \mu}{2T}\right) \\ & + \theta(p_0) \delta(p^2 - m^2) \frac{\text{Tr}(-p - k)}{((p+k)^2 - m^2)} \tanh\left(\frac{p_0 + \mu}{2T}\right) \\ & \left. + \theta(p_0) \delta(p^2 - m^2) \frac{\text{Tr}(p - k)}{((p-k)^2 - m^2)} \tanh\left(\frac{p_0 - \mu}{2T}\right) \right]. \end{aligned} \quad (4.12)$$

Finally, we use the identity (3.36b). Using these, we express each tanh in the self-energy in terms of the Fermi-Dirac distribution f_{FD} .

For the on-shell expression, the self-energy only has a real part. In this case, we can leave out the part proportional to 1 (as opposed to the parts proportional to the phase space distributions) since this term is the zero-temperature QFT correction and should be dealt

with by renormalization. This yields, for the temperature-dependent part of the self-energy:

$$\begin{aligned} \Pi^{\mu\nu} = 4\pi\alpha \int \frac{d^3p}{(2\pi)^3} \int dp_0 \theta(p_0) \delta(p^2 - m^2) \times \\ \left\{ f_{\text{FD}}\left(\frac{p_0 - \mu}{T}\right) \left[\frac{\text{Tr}(p)}{((p+k)^2 - m^2)} + \frac{\text{Tr}(p-k)}{((p-k)^2 - m^2)} \right] \right. \\ \left. + f_{\text{FD}}\left(\frac{p_0 + \mu}{T}\right) \left[\frac{\text{Tr}(-p-k)}{((p+k)^2 - m^2)} + \frac{\text{Tr}(-p)}{((p-k)^2 - m^2)} \right] \right\}. \end{aligned} \quad (4.13)$$

We define the following short forms for the electron and positron distributions:

$$f(E) = f_{\text{FD}}\left(\frac{E - \mu}{T}\right) = \frac{1}{e^{(E-\mu)/T} + 1}, \quad \bar{f}(E) = f_{\text{FD}}\left(\frac{E + \mu}{T}\right) = \frac{1}{e^{(E+\mu)/T} + 1}. \quad (4.14)$$

Writing the traces explicitly, the self-energy is:

$$\begin{aligned} \Pi^{\mu\nu} = 4\pi\alpha \int \frac{d^3p}{(2\pi)^3} \int dp_0 \theta(p_0) \delta(p^2 - m^2) \times \\ \left\{ f(E_p) \left[\frac{\text{Tr}[(\not{p} + m)\gamma^\mu(\not{p} + \not{k} + m)\gamma^\nu]}{((p+k)^2 - m^2)} + \frac{\text{Tr}[(\not{p} - \not{k} + m)\gamma^\mu(\not{p} + m)\gamma^\nu]}{((p-k)^2 - m^2)} \right] \right. \\ \left. + \bar{f}(E_p) \left[\frac{\text{Tr}[(\not{p} + \not{k} - m)\gamma^\mu(\not{p} - m)\gamma^\nu]}{((p+k)^2 - m^2)} + \frac{\text{Tr}[(\not{p} - m)\gamma^\mu(\not{p} - \not{k} - m)\gamma^\nu]}{((p-k)^2 - m^2)} \right] \right\}. \end{aligned} \quad (4.15)$$

The delta function puts one of the fermions in the loop on shell. Doing the p_0 integral yields

$$\begin{aligned} \Pi^{\mu\nu} = 4\pi\alpha \int \frac{d^3p}{(2\pi)^3} \frac{1}{2E_p} \times \\ \left\{ f(E_p) \left[\frac{\text{Tr}[(\not{p} + m)\gamma^\mu(\not{p} + \not{k} + m)\gamma^\nu]}{((p+k)^2 - m^2)} + \frac{\text{Tr}[(\not{p} - \not{k} + m)\gamma^\mu(\not{p} + m)\gamma^\nu]}{((p-k)^2 - m^2)} \right] \right. \\ \left. + \bar{f}(E_p) \left[\frac{\text{Tr}[(\not{p} + \not{k} - m)\gamma^\mu(\not{p} - m)\gamma^\nu]}{((p+k)^2 - m^2)} + \frac{\text{Tr}[(\not{p} - m)\gamma^\mu(\not{p} - \not{k} - m)\gamma^\nu]}{((p-k)^2 - m^2)} \right] \right\}, \end{aligned} \quad (4.16)$$

which is, schematically,

$$\begin{aligned}
 \text{Diagram: } & \text{A circular loop with two external wavy lines labeled } p \text{ and } k. \\
 & = \int \frac{d^3 p}{(2\pi)^3} \frac{1}{2E_p} \left\{ f(E_p) \left[\begin{array}{c} \text{Diagram: Two wavy lines } p+k \text{ meeting at a vertex, with a horizontal line } k \text{ connecting them.} \\ + \end{array} \right. \right. \\
 & \quad \left. \left. + \bar{f}(E_p) \left[\begin{array}{c} \text{Diagram: Two wavy lines } p+k \text{ meeting at a vertex, with a horizontal line } k \text{ connecting them.} \\ + \end{array} \right. \right] \right\}. \tag{4.17}
 \end{aligned}$$

In this form, the expression makes contact with the forward scattering physical interpretation of Section 3.5: the finite temperature part of the self-energy is one where the photon propagates in a momentum eigenstate, but where forward scattering happens with the real, on-shell electrons and positrons that constitute the plasma. These forward scatterings are appropriately weighted by the phase space distribution of these electrons and positrons, namely the Fermi-Dirac distribution when assuming thermal equilibrium.

Finally, we now explicitly evaluate the Dirac traces. First, notice that the expressions in brackets for electrons and positrons are the same. Indeed, the one for the positron is mathematically equivalent to the one for the electron with the replacement $m \rightarrow -m$. However, these expressions only depend on m^2 because of Dirac trace properties. We can write:

$$\begin{aligned}
 \Pi^{\mu\nu} &= 16\pi\alpha \int \frac{d^3 p}{(2\pi)^3} \frac{1}{2E_p} (f(E_p) + \bar{f}(E_p)) \\
 &\times \left[\frac{\frac{1}{4} \text{Tr}[(\not{p} + m)\gamma^\mu(\not{p} + \not{k} + m)\gamma^\nu]}{((p+k)^2 - m^2)} + \frac{\frac{1}{4} \text{Tr}[(\not{p} - \not{k} + m)\gamma^\mu(\not{p} + m)\gamma^\nu]}{((p-k)^2 - m^2)} \right]. \tag{4.18}
 \end{aligned}$$

The expression in brackets evaluates to:

$$\begin{aligned}
 [...] &= \frac{2p^\mu p^\nu + (k^\mu p^\nu + k^\nu p^\mu) - \eta^{\mu\nu}(p \cdot k)}{k^2 + 2(p \cdot k)} + \frac{2p^\mu p^\nu - (k^\mu p^\nu + k^\nu p^\mu) + \eta^{\mu\nu}(p \cdot k)}{k^2 - 2(p \cdot k)} \\
 &= \frac{(2k^2)2p^\mu p^\nu - 4(p \cdot k)(k^\mu p^\nu + k^\nu p^\mu) + 4(p \cdot k)^2\eta^{\mu\nu}}{(k^2)^2 - 4(p \cdot k)^2}. \tag{4.19}
 \end{aligned}$$

We finally get

$$\begin{aligned} \Pi^{\mu\nu} = 16\pi\alpha \int \frac{d^3p}{(2\pi)^3} \frac{1}{2E_p} & [f(E_p) + \bar{f}(E_p)] \\ & \times \frac{(p \cdot k)(k^\mu p^\nu + k^\nu p^\mu) - (k^2)p^\mu p^\nu - (p \cdot k)^2 \eta^{\mu\nu}}{(p \cdot k)^2 - \frac{1}{4}(k^2)^2}, \end{aligned} \quad (4.20)$$

which is the starting point of the computation in Braaten and Segel [1]. This is where we proceed to analytic continuation to evaluate this for photons with real frequencies.

Note that electrons and positrons are the lightest fermions that can enter this loop. In the early universe period under consideration in Chapter 1, muons and heavier fermions are non-relativistic, so their contributions are subdominant as they are suppressed by a factor of $1/m_{\text{fer}}^2$ from the propagators. However, this whole computation doesn't explicitly depend on the nature of the fermions in the loop. They were assumed to be electrons but the mass m remains a free parameter. This expression is valid for any spin- $\frac{1}{2}$ fermion that runs in the loop, and one could extend all these results to an arbitrary plasma.

4.2 On-shell analytic approximations

4.2.1 Removing the $(K^2)^2$ term in the denominator

This section is based on Braaten and Segel [1]. The computations are presented differently, in a way which better generalizes to the off-shell computations of Chapter 5. Let us state again the expression for the self-energy, now using the notation with uppercase letters for 4-vectors and lowercase letters for 3-vectors,

$$\Pi^{\mu\nu}(K) = 16\pi\alpha \int \frac{d^3p}{2E} [f + \bar{f}] \frac{(P \cdot K)(P^\mu K^\nu + K^\mu P^\nu) - K^2 P^\mu P^\nu - (P \cdot K)^2 g^{\mu\nu}}{(P \cdot K)^2 - (K^2)^2/4}, \quad (4.21)$$

where f stands for $f(E)$, and similarly for \bar{f} . In the medium rest frame, $K^\mu = (\omega, \mathbf{k})$, $P^\mu = (E, \mathbf{p})$, $k = |\mathbf{k}|$, $p = |\mathbf{p}|$, $K^2 = \omega^2 - k^2$, $E^2 = p^2 + m^2$, and $P \cdot K = E\omega - \mathbf{p} \cdot \mathbf{k} = E\omega - pk \cos \theta$. Recall that the medium's bulk velocity is $U^\mu = (1, \mathbf{0})$ in its rest frame, and that all quantities above are Lorentz scalars, i.e., $\omega = (U \cdot K)$, etc.

The denominator in this expression goes to zero when both the electrons (or positrons) in the loop go on shell, and the self-energy develops an imaginary part. This would mean a regime where the decay $\gamma \rightarrow e^+e^-$ is allowed. For on-shell photons, that decay is never kinematically allowed. In fact, the electrons (and positrons) also have thermal corrections to their mass in-medium [26]:

$$m(T) = \frac{m_e}{2} + \sqrt{\frac{m_e^2}{4} + m_{\text{eff}}^2(T)}, \quad (4.22)$$

with

$$m_{\text{eff}}^2(T) = \frac{\alpha}{\pi} \int_0^\infty dE \ E \left[\frac{1}{e^{(E-\mu)/T} + 1} + \frac{1}{e^{(E+\mu)/T} + 1} + 2 \frac{1}{e^{E/T} - 1} \right], \quad (4.23)$$

where $m_e = 0.511$ MeV is the bare mass. The thermal correction $m_{\text{eff}}^2(T)$ is such that we never have $K^2 > 4m^2$, i.e., that the decay $\gamma \rightarrow e^+e^-$ is always forbidden. This imaginary part in the self-energy is therefore an artifact in this case. Fortunately, for on-shell photons, K^2 is of the order of ω_p^2 and is small compared to typical electron energies, which means we always have $|\omega^2 - k^2| \ll E|\omega - \mathbf{v} \cdot \mathbf{p}|$, i.e., $|K^2| \ll |P \cdot K|$. The $(K^2)^2$ term in the denominator thus contributes to corrections that are numerically comparable to α^2 in the on-shell case and can therefore be dropped [1]. This simplifies the integral greatly and has the added advantage of removing the imaginary part arising from the non-physical decay $\gamma \rightarrow e^+e^-$. Crucially, this whole argument relies on the smallness of K^2 which is always true on shell. It is also the case that K^2 is small in the soft momentum limit by definition. Therefore, the on-shell expressions derived in this section are also valid for soft off-shell photons. However, for general off-shell particles, K^2 can be anything.

Recall the self-energy of the L and T modes are, in the medium frame:

$$\Pi_L = \frac{K^2}{k^2} \Pi^{00} = \frac{K^2}{k^2} \Pi_L^{\text{BS}}, \quad \Pi_T = \frac{1}{2} \left(\delta_{ij} - \frac{k_i k_j}{k^2} \right) \Pi^{ij} = \Pi_T^{\text{BS}}. \quad (4.24)$$

The superscript “BS” refers to Reference [1], which uses the Coulomb gauge. The only difference is the normalization for the L modes, and one can easily convert between these two gauges with Equation (4.24). The integrand in Equation (4.21) is only a function of p and $\cos \theta$, due to azimuthal symmetry. In that case,

$$16\pi\alpha \int \frac{d^3 p}{2E} = \frac{4\alpha}{\pi} \int_0^\infty dp \frac{p^2}{E} \frac{1}{2} \int_{-1}^1 d \cos \theta, \quad (4.25)$$

and, introducing G_a with $a = T, L$,

$$\Pi_a(K) = \frac{4\alpha}{\pi} \int_0^\infty dp \frac{p^2}{E} (f + \bar{f}) \frac{1}{2} \int_{-1}^1 d \cos \theta G_a(p, \cos \theta), \quad (4.26)$$

with

$$G_L = \frac{K^2}{k^2} \left[-1 + \frac{2E\omega}{(P \cdot K)} - \frac{K^2 E^2}{(P \cdot K)^2} \right], \quad (4.27a)$$

$$G_T = -\frac{K^2}{2k^2} \left[-\frac{\omega^2 + k^2}{K^2} + \frac{2E\omega}{(P \cdot K)} + \frac{p^2 k^2 - E^2 \omega^2}{(P \cdot K)^2} \right]. \quad (4.27b)$$

Let us define the following parameter, which is actually the index of refraction:

$$n = \frac{k}{\omega}. \quad (4.28)$$

This is a convenient parameter because it turns out that the on-shell photon self-energy depends on ω and k only in this specific ratio and not on each of these variables independently.

We also define these new integration variables:

$$v = \frac{p}{E} \implies E = \frac{m}{\sqrt{1-v^2}} \quad p = \frac{mv}{\sqrt{1-v^2}}, \quad (4.29a)$$

$$u = \frac{P \cdot K}{E\omega} = 1 - nv \cos \theta. \quad (4.29b)$$

The change to u is straightforward. The change to v instead of p yields:

$$dp = \frac{m}{(1-v^2)^{3/2}} dv \quad \text{and} \quad \int_0^\infty dp \frac{p^2}{E} = m^2 \int_0^1 dv \frac{v^2}{(1-v^2)^2}. \quad (4.30)$$

Then,

$$\Pi_a = m^2 \frac{4\alpha}{\pi} \int_0^1 dv (f + \bar{f}) F_a(v), \quad (4.31)$$

where we introduce

$$F_a(v) = \frac{v^2}{(1-v^2)^2} \frac{1}{2nv} \int_{1-nv}^{1+nv} du G_a, \quad (4.32)$$

and where G_a becomes

$$G_L = \frac{1-n^2}{n^2} \left[-1 + \frac{2}{u} - \frac{1-n^2}{u^2} \right], \quad (4.33a)$$

$$G_T = -\frac{1-n^2}{2n^2} \left[-\frac{1+n^2}{1-n^2} + \frac{2}{u} - \frac{1-n^2 v^2}{u^2} \right]. \quad (4.33b)$$

Integrating over u , we are left with:

$$F_L^{\text{On}} = \frac{v^2}{(1-v^2)^2} \frac{1-n^2}{n^2} \left[-1 + \frac{1}{nv} \log \frac{1+nv}{1-nv} - \frac{1-n^2}{1-n^2 v^2} \right], \quad (4.34a)$$

$$F_T^{\text{On}} = -\frac{v^2}{(1-v^2)^2} \frac{1-n^2}{2n^2} \left[-\frac{2}{1-n^2} + \frac{1}{nv} \log \frac{1+nv}{1-nv} \right]. \quad (4.34b)$$

These correspond to Equations (A16) and (A17) in Reference [1]. The “On” superscript (for on shell) has been added to distinguish these from the expressions derived in Chapter 5.

4.2.2 Integration by parts and sharp peak approximation

In the general case, the plasma frequency is given by [1, 2]

$$\omega_p^2 = \frac{4\alpha}{\pi} \int_0^\infty dp \frac{p^2}{E} \left(1 - \frac{1}{3}v^2\right) [f + \bar{f}]. \quad (4.35)$$

We can re-express this as an integral over v :

$$\omega_p^2 = m^2 \frac{4\alpha}{\pi} \int_0^1 dv \frac{v^2}{(1-v^2)^2} \left(1 - \frac{1}{3}v^2\right) (f + \bar{f}). \quad (4.36)$$

Integration by parts of this last expression yields:

$$\omega_p^2 = -m^2 \frac{4\alpha}{3\pi} \int_0^1 dv \frac{v^3}{1-v^2} \frac{d}{dv} (f + \bar{f}) \equiv \int_0^1 dv \frac{d\omega_p^2}{dv}. \quad (4.37)$$

The boundary term vanishes. We define the following:

$$\tilde{J}_a(v) = \int_0^v dv' F_a(v') \quad \text{and} \quad J_a(v) = \frac{3(1-v^2)}{v^3} \tilde{J}_a(v), \quad (4.38)$$

and integrate by parts the self-energy as well:

$$\begin{aligned} \Pi_a &= m^2 \frac{4\alpha}{\pi} \int_0^1 dv (f + \bar{f}) F_a(v) \\ &= -m^2 \frac{4\alpha}{\pi} \int_0^1 dv \tilde{J}_a(v) \frac{d}{dv} (f + \bar{f}) \\ &= -m^2 \frac{4\alpha}{3\pi} \int_0^1 dv J_a(v) \frac{v^3}{1-v^2} \frac{d}{dv} (f + \bar{f}) \\ &= \int_0^1 dv J_a(v) \frac{d\omega_p^2}{dv}. \end{aligned} \quad (4.39)$$

The boundary terms vanish too, at $v = 0$ by definition of $\tilde{J}_a(v)$ and at $v = 1$ because of the phase space. Recall that $f(z) \sim \tanh(z)$, so the derivative of the phase space should be

sharply peaked around some velocity v_* , and therefore $d\omega_p^2/dv$ should be sharply peaked as well. If this peak is sharp and narrow enough, in other words, if $J_a(v; K)$ is slow-varying enough around this peak, then we can approximate $J_a(v) \simeq J_a(v_*) = const.$, and take it out of the integral:

$$\begin{aligned}\Pi_a &\simeq J_a(v_*) \left(-m^2 \frac{4\alpha}{3\pi} \int_0^1 dv \frac{v^3}{1-v^2} \frac{d}{dv} (f + \bar{f}) \right) \\ &\implies \Pi_a(K) \simeq \omega_p^2 J_a(v_*; K).\end{aligned}\quad (4.40)$$

Performing the integration by parts, we get

$$J_L^{\text{On}}(v) = \frac{3}{v^2} \left(\frac{1-n^2}{n^2} \right) \left[\frac{1}{2nv} \log \left(\frac{1+nv}{1-nv} \right) - 1 \right], \quad (4.41a)$$

$$J_T^{\text{On}}(v) = \frac{3}{2v^2} \left[\frac{1}{n^2} - \left(\frac{1-n^2v^2}{n^2} \right) \frac{1}{2nv} \log \left(\frac{1+nv}{1-nv} \right) \right], \quad (4.41b)$$

and using the approximation, we get

$$\Pi_L^{\text{On}} = \omega_p^2 \frac{3}{v_*^2} \left(\frac{1-n^2}{n^2} \right) \left[\frac{1}{2nv_*} \log \left(\frac{1+nv_*}{1-nv_*} \right) - 1 \right], \quad (4.42a)$$

$$\Pi_T^{\text{On}} = \omega_p^2 \frac{3}{2v_*^2} \left[\frac{1}{n^2} - \left(\frac{1-n^2v_*^2}{n^2} \right) \frac{1}{2nv_*} \log \left(\frac{1+nv_*}{1-nv_*} \right) \right]. \quad (4.42b)$$

These match with Equations (A45) and (A46) in Reference [1], modulo the normalization for the L mode.

Figure 4.3 shows $J(v)$ and $d\omega_p^2/dv$ as a function of v , for some values of the parameters n , $x = m/T$, and $y = \mu/T$. We can see that $J(v)$ is indeed slow-varying enough for both L and T modes. Furthermore, we can see that $d\omega_p^2/dv$ is indeed always peaked around some velocity, different for each regime. In the classical case (for example, $x = 10$ and $y = 0$ in the figure), this peak is fairly wide. However, the fact that $J(v)$ is indeed effectively constant for a wide range of velocities means that the approximation is still valid.

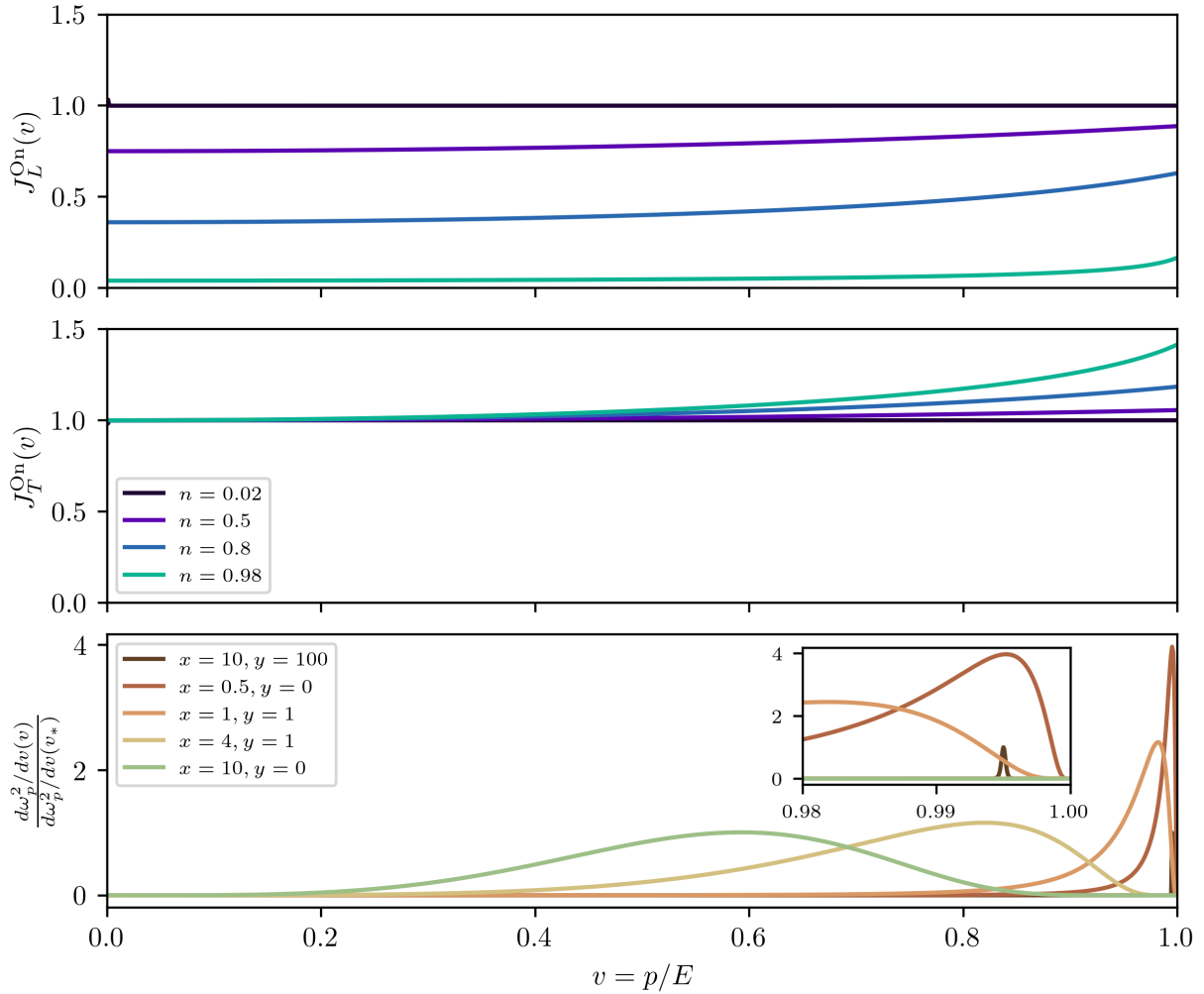


Figure 4.3: Plots of $J(v)$ for some values of n (top and middle), and plots of $d\omega_p^2/dv$ for some values of $x = m/T$ and $y = \mu/T$ (bottom), as a function of v . The two top panels show that $J(v)$ is indeed quite flat, and the bottom one that $d\omega_p^2/dv$ is sharply peaked.

The peak velocity is approximately given by [1]

$$v_* = \frac{\omega_1}{\omega_p}, \quad (4.43)$$

with

$$\omega_1^2 = \frac{4\alpha}{\pi} \int_0^\infty dp \frac{p^2}{E} \left(\frac{5}{3}v^2 - v^4 \right) [f + \bar{f}]. \quad (4.44)$$

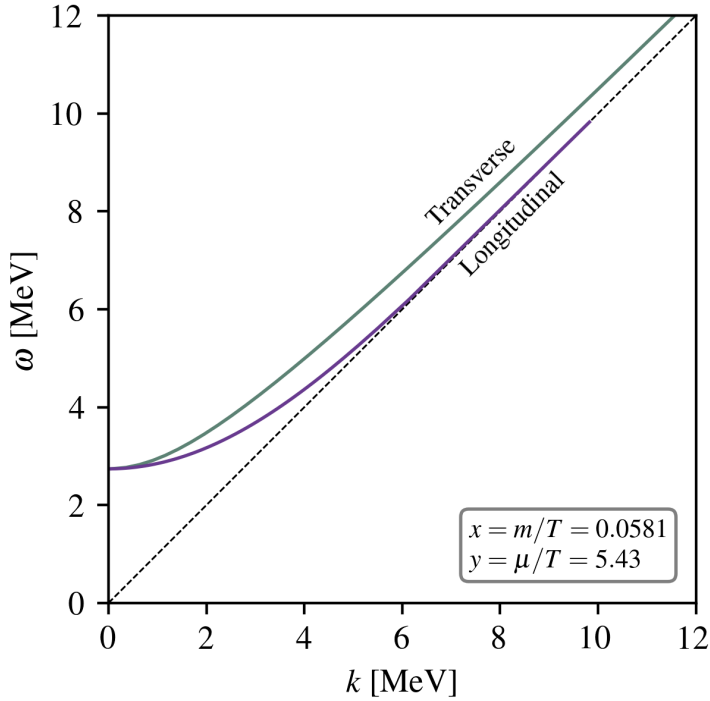


Figure 4.4: Dispersion relations for both photon modes on shell, using the analytical approximations; adapted from [1]. The longitudinal one stops when it crosses the light cone, shown in a dashed line. The values of x and y are the same as those from Figure 1 in [1]. The thermal correction of the electron mass wasn't taken into account.

Indeed, we can verify that this is self-consistent. Changing the integration variable to v in Equation (4.44) and integrating by parts yields

$$\omega_1^2 = -m^2 \frac{4\alpha}{3\pi} \int_0^1 dv \frac{v^5}{1-v^2} \frac{d}{dv} (f + \bar{f}). \quad (4.45)$$

Then,

$$\begin{aligned} \omega_p^2 - \omega_1^2 &= -m^2 \frac{4\alpha}{3\pi} \int_0^1 dv \frac{v^3 - v^5}{1-v^2} \frac{d}{dv} (f + \bar{f}) \\ &= \int_0^1 dv (1-v^2) \frac{d\omega_p^2}{dv}. \end{aligned} \quad (4.46)$$

Calling v_{peak} the exact velocity where $d\omega_p^2/dv$ has its maximum, we can use the sharp peak approximation, i.e., evaluate $1-v^2$ at v_{peak} and take it out of the integral. The rest integrates

to ω_p^2 , and we get the final result:

$$\omega_p^2(1 - v_*^2) \simeq \omega_p^2(1 - v_{\text{peak}}^2). \quad (4.47)$$

This v_* is thus not exactly at the peak but it is close to it (which explains why some of the maximums are greater than one in the bottom part of Figure 4.3, even if these are normalized to the value at v_*).

Braaten and Segel derived these expressions explicitly for on-shell, timelike photons. The self-energy is entirely real in this regime by design, to avoid the non-physical $\gamma \rightarrow e^+e^-$ decay. They derive a cutoff momentum k_1 for the longitudinal self-energy when the dispersion relation crosses the light cone (the transverse one never crosses it). The dispersion relation (2.28) provides an implicit equation for $\omega(k)$. These are shown in Figure 4.4 for some values of $x = m/T$ and $y = \mu/T$, with the longitudinal one stopping at k_1 . Since the self-energy only depends on n in this case, we can obtain a simple parametric representation of the dispersion relation:

$$\omega(n) = \sqrt{\frac{\Pi_a(n)}{1 - n^2}}, \quad k(n) = n \omega(n), \quad a = L, T. \quad (4.48)$$

The on-shell dispersion relations live on a line in phase space as shown in Figure 4.4. The general expressions for the self-energy that also include off-shell photons, discussed in the next chapter, extend this to the whole ω and k plane.

Chapter 5

General photon self-energy

In this chapter, I will derive analytical approximations in a similar way to what Braaten and Segel did except I will not assume that the photons are on shell or that the momentum is soft. I will thus compute a more general expression for $J(v)$ and, assuming it's flat enough, take it out of the integral evaluating it at the typical electron velocity v_* to find $\Pi_a \simeq \omega_p^2 J(v_*)$. This computation is much more complicated than the on-shell one. Furthermore, the on-shell expressions only depended on the ratio $n = \omega/k$. Here, these expressions will depend separately on ω and k . I will instead parametrize them in terms of n and g first for the initial computations, and in terms of n and ξ for the final results. These parameters are defined as:

$$n = \frac{k}{\omega}, \quad g = \frac{K^2}{2m\omega} = \frac{\omega^2 - k^2}{2m\omega},$$
$$\xi = \frac{\sqrt{|\omega^2 - k^2|}}{2m} = \begin{cases} g/\sqrt{1 - n^2} & \text{timelike,} \\ -g/\sqrt{n^2 - 1} & \text{spacelike.} \end{cases} \quad (5.1)$$

The first parameter, n , is the index of refraction. This is a convenient parameter, because it makes it easy to delineate between timelike ($0 < n < 1$) and spacelike ($n > 1$) photons. The parameter ξ represents the ratio of the photon's "gap mass" to twice the electron mass.

It is defined in such a way that it is always real and positive. For timelike photons, this is particularly convenient, because the $\xi > 1$ versus $\xi < 1$ regions of phase space represent the regimes where a $\gamma \rightarrow e^+e^-$ process is allowed or forbidden, respectively. Furthermore, only the $(K^2)^2$ term in the denominator is proportional to ξ , so it turns out that one can recover the on-shell expression in the limit $\xi \rightarrow 0$. Finally, the parameters n and ξ cover all of phase space, and are completely independent, except for the special case of $n = 1$ where ξ must be zero to be consistent. We can invert these relations if necessary, for $n \neq 1$:

$$\omega = \frac{2m\xi}{\sqrt{|1-n^2|}}, \quad k = n\omega. \quad (5.2)$$

Finally, the parameter g is simply used in intermediate calculations, until the need to compute things case-by-case presents itself.

I will derive the real and imaginary parts separately, because integration by parts involves boundary terms for the imaginary part but not the real part. Furthermore, it will be convenient to express the final expressions case by case for three regimes: timelike light photons ($0 < n < 1, 0 < \xi < 1$), timelike heavy photons ($0 < n < 1, \xi > 1$), and spacelike photons ($n > 1$). Furthermore, note that k is positive, since it's the magnitude of the momentum vector \mathbf{k} . On the other hand, ω can be positive or negative. Since it is known that the real part of self-energy is even and the imaginary part is odd [24],

$$\text{Re}[\Pi(-\omega)] = \text{Re}[\Pi(\omega)] \quad \text{Im}[\Pi(-\omega)] = -\text{Im}[\Pi(\omega)] \quad (5.3)$$

we will assume $\omega > 0$ (equivalently $n > 0$) without loss of generality. Finally, throughout this chapter, the a subscript stands for modes L or T.

5.1 Real part

Once again we start from this expression,

$$\Pi^{\mu\nu} = 16\pi\alpha \int \frac{d^3p}{2E} [f + \bar{f}] \frac{(P \cdot K)(P^\mu K^\nu + K^\mu P^\nu) - K^2 P^\mu P^\nu - (P \cdot K)^2 g^{\mu\nu}}{(P \cdot K)^2 - (K^2)^2/4}. \quad (5.4)$$

This time, we must keep the $(K^2)^2$ term in the denominator. We could remove it for on-shell photons because the thermal corrections to the electron (and positron) mass always guarantee that the decay $\gamma \rightarrow e^+e^-$ is forbidden. For off-shell photons, and without assuming soft momentum, this “decay” is just a vertex in a Feynman diagram, and is, of course, allowed. Therefore, we must work with the general expression to find the self-energy that is valid in all regimes, including off shell.

Recall that we aim to compute $J(v)$, and the steps to do so are

$$F_a(v) = \int_{1-nv}^{1+nv} du G_a, \quad (5.5a)$$

$$J_a(v) = \frac{3(1-v^2)}{v^3} \int_0^v dv' F_a(v'). \quad (5.5b)$$

Switching to parameters n and g , defined just above, and using the following:

$$h = \frac{K^2}{2E\omega} = g\sqrt{1-v^2}, \quad (5.6)$$

we get for G_a :

$$G_L = \left(\frac{1-n^2}{n^2} \right) \frac{-u^2 + 2u - (1-n^2)}{u^2 - h^2}, \quad (5.7a)$$

$$G_T = -\left(\frac{1-n^2}{2n^2} \right) \frac{-u^2(1+n^2)/(1-n^2) + 2u - (1-n^2v^2)}{u^2 - h^2}, \quad (5.7b)$$

which is of the general form

$$G_a = B_a \frac{A_a u^2 + 2u + C_a}{u^2 - h^2}. \quad (5.8)$$

Computing F_a , we get

$$\begin{aligned} 4nv \frac{(1-v^2)^2}{v^2} \frac{F}{B} &= 2 \int_{1-nv}^{1+nv} du \frac{Au^2 + 2u + C}{u^2 - h^2} \\ &= \int_{1-nv}^{1+nv} du \left(\frac{Au + 2 - C/h}{u + h} + \frac{Au + 2 + C/h}{u - h} \right) \\ &= \int_{1-nv+h}^{1+nv+h} du \left(A + \frac{2 - Ah - C/h}{u} \right) + \int_{1-nv-h}^{1+nv-h} du \left(A + \frac{2 + Ah + C/h}{u} \right) \\ &= 4nvA + \left(2 - Ah - \frac{C}{h} \right) \log \frac{1 + nv + h}{1 - nv + h} + \left(2 + Ah + \frac{C}{h} \right) \log \frac{1 + nv - h}{1 - nv - h} \\ \frac{(1-v^2)^2}{v^2} \frac{F}{B} &= A + \frac{1}{2nv} \log \frac{(1+nv)^2 - h^2}{(1-nv)^2 - h^2} + \left(\frac{Ah}{4nv} + \frac{C}{4nvh} \right) \log \frac{1 - (nv - h)^2}{1 - (nv + h)^2}. \end{aligned} \quad (5.9)$$

The full expressions are, in terms of n and g , are

$$\begin{aligned} F_T &= \left[\frac{1+n^2}{2n^2} \right] \frac{v^2}{(1-v^2)^2} \\ &\quad + \left[\frac{1-n^2}{4n^3} \right] \frac{v}{(1-v^2)^2} \log \frac{(1-nv)^2 - g^2(1-v^2)}{(1+nv)^2 - g^2(1-v^2)} \\ &\quad + \left[-\frac{(1+n^2)g^2 + n^2(1-n^2)}{8n^3g} \right] \frac{v}{(1-v^2)^{3/2}} \log \frac{1 - (nv + g\sqrt{1-v^2})^2}{1 - (nv - g\sqrt{1-v^2})^2} \\ &\quad + \left[-\frac{(1-n^2)^2}{8n^3g} \right] \frac{v}{(1-v^2)^{5/2}} \log \frac{1 - (nv + g\sqrt{1-v^2})^2}{1 - (nv - g\sqrt{1-v^2})^2}, \end{aligned} \quad (5.10)$$

$$\begin{aligned} F_L &= \left[-\frac{1-n^2}{n^2} \right] \frac{v^2}{(1-v^2)^2} \\ &\quad + \left[-\frac{1-n^2}{2n^3} \right] \frac{v}{(1-v^2)^2} \log \frac{(1-nv)^2 - g^2(1-v^2)}{(1+nv)^2 - g^2(1-v^2)} \\ &\quad + \left[\frac{g(1-n^2)}{4n^3} \right] \frac{v}{(1-v^2)^{3/2}} \log \frac{1 - (nv + g\sqrt{1-v^2})^2}{1 - (nv - g\sqrt{1-v^2})^2} \\ &\quad + \left[\frac{(1-n^2)^2}{4n^3g} \right] \frac{v}{(1-v^2)^{5/2}} \log \frac{1 - (nv + g\sqrt{1-v^2})^2}{1 - (nv - g\sqrt{1-v^2})^2}. \end{aligned} \quad (5.11)$$

Next, we want to compute J_a . Recall that

$$\tilde{J}_a(v) = \int_0^v dv' F_a(v') \quad \text{and} \quad J_a(v) = \frac{3(1-v^2)}{v^3} \tilde{J}_a(v). \quad (5.12)$$

Therefore, implicitly defining the $C_{a,i}$'s as the terms in brackets in Equations (5.10) and (5.11), this can be expressed as

$$\tilde{J}_a(v) = C_{a,1}I_1 + C_{a,2}I_2 + C_{a,3}I_3 + C_{a,4}I_4, \quad (5.13)$$

where we have four indefinite integrals to solve:

$$I_1 = \int dv \frac{v^2}{(1-v^2)^2} \quad (5.14a)$$

$$I_2 = \int dv \frac{v}{(1-v^2)^2} \log \frac{(1-nv)^2 - g^2(1-v^2)}{(1+nv)^2 - g^2(1-v^2)} \quad (5.14b)$$

$$I_3 = \int dv \frac{v}{(1-v^2)^{3/2}} \log \frac{1 - (nv + g\sqrt{1-v^2})^2}{1 - (nv - g\sqrt{1-v^2})^2} \quad (5.14c)$$

$$I_4 = \int dv \frac{v}{(1-v^2)^{5/2}} \log \frac{1 - (nv + g\sqrt{1-v^2})^2}{1 - (nv - g\sqrt{1-v^2})^2}. \quad (5.14d)$$

These integrals are, using integration by parts once again for I_2 , I_3 and I_4 :

$$I_1 = \frac{1}{4} \left(\frac{2v}{1-v^2} - \log \frac{1+v}{1-v} \right) \quad (5.15)$$

$$I_2 = \frac{1}{2(1-v^2)} \log \frac{(1-nv)^2 - g^2(1-v^2)}{(1+nv)^2 - g^2(1-v^2)} + \frac{n(1-n^2-2g^2)}{(1-n^2)^2} \int dv \frac{2}{1-v^2} \quad (5.16)$$

$$+ \frac{g^2+n^2(-1+n^2+g^2)}{2(1-n^2)^2} \int dv \left[\frac{2((g^2+n^2)v+n)}{(1+nv)^2 - g^2(1-v^2)} - \frac{2((g^2+n^2)v-n)}{(1-nv)^2 - g^2(1-v^2)} \right] \\ - \frac{2gn}{(1-n^2)^2} \int dv \left[\frac{g(-1+n^2+g^2)}{(1+nv)^2 - g^2(1-v^2)} + \frac{g(-1+n^2+g^2)}{(1-nv)^2 - g^2(1-v^2)} \right]$$

$$I_3 = \frac{1}{\sqrt{1-v^2}} \log \frac{1 - (nv + g\sqrt{1-v^2})^2}{1 - (nv - g\sqrt{1-v^2})^2} \quad (5.17)$$

$$\begin{aligned}
 & -\frac{2gn}{1-n^2} \int dv \frac{2}{1-v^2} \\
 & + \frac{g}{1-n^2} \int dv \left[\frac{2((g^2+n^2)v+n)}{(1+nv)^2-g^2(1-v^2)} - \frac{2((g^2+n^2)v-n)}{(1-nv)^2-g^2(1-v^2)} \right] \\
 & - \frac{2n}{1-n^2} \int dv \left[\frac{g(-1+n^2+g^2)}{(1+nv)^2-g^2(1-v^2)} + \frac{g(-1+n^2+g^2)}{(1-nv)^2-g^2(1-v^2)} \right] \\
 I_4 = & \frac{1}{3(1-v^2)^{3/2}} \log \frac{1-(nv+g\sqrt{1-v^2})^2}{1-(nv-g\sqrt{1-v^2})^2} \\
 & - \frac{2gn}{3(1-n^2)} \int dv \frac{1+v^2}{(1-v^2)^2} \\
 & - \frac{gn(2g^2(3+n^2)-3(1-n^4))}{3(1-n^2)^3} \int dv \frac{2}{1-v^2} \\
 & + \frac{g(g^2+3n^2(-1+n^2+g^2))}{3(1-n^2)^3} \int dv \left[\frac{2((g^2+n^2)v+n)}{(1+nv)^2-g^2(1-v^2)} - \frac{2((g^2+n^2)v-n)}{(1-nv)^2-g^2(1-v^2)} \right] \\
 & + \frac{2n(3g^2+n^2(-1+g^2+n^2)}{3(n^2-1)^3} \int dv \left[\frac{g(-1+n^2+g^2)}{(1+nv)^2-g^2(1-v^2)} + \frac{g(-1+n^2+g^2)}{(1-nv)^2-g^2(1-v^2)} \right]
 \end{aligned} \tag{5.18}$$

This computation has been reduced to solving four new, more straightforward integrals.

The first two yield

$$\int dv \frac{1+v^2}{(1-v^2)^2} = \frac{v}{1-v^2}, \tag{5.19}$$

$$\int dv \frac{2}{1-v^2} = \log \frac{1+v}{1-v}. \tag{5.20}$$

The first term of the third integral is:

$$\int dv \frac{2((g^2+n^2)v+n)}{(1+nv)^2-g^2(1-v^2)} = \log ((1+nv)^2-g^2(1-v^2)), \tag{5.21}$$

and the second term is the same with $n \rightarrow -n$. The last integral is also straightforward but has some subtleties. The first term of this integral is:

$$I_{\tan}(n) = \int dv \frac{g(-1+n^2+g^2)}{(1+nv)^2-g^2(1-v^2)} = \int dv \frac{g(g^2+n^2)(-1+n^2+g^2)}{((g^2+n^2)v+n)^2-g^2(-1+n^2+g^2)}, \tag{5.22}$$

and the second term is $I_{\tan}(-n)$. We make a change in variables:

$$w = (g^2 + n^2)v + n \quad dw = (g^2 + n^2)dv$$

$$I_{\tan}(n) = \int dw \frac{g(-1 + n^2 + g^2)}{w^2 - g^2(-1 + n^2 + g^2)}. \quad (5.23)$$

The next steps depend on the sign of $(-1 + n^2 + g^2)$. For spacelike photons, i.e. $n > 1$, this is always positive. For timelike photons, $n < 1$, recall that $g = \xi\sqrt{1 - n^2}$. Then

$$(-1 + n^2 + g^2) = (1 - n^2)(\xi^2 - 1). \quad (5.24)$$

This is positive for heavier photons, $\xi > 1$, and negative for lighter photons, $\xi < 1$. For the case of timelike light photons, define $-1 + n^2 + g^2 = -a^2 < 0$, then:

$$z = \frac{w}{ga} \quad dz = \frac{dw}{ga}$$

$$I_{\tan}(n) = - \int dw \frac{ga^2}{w^2 + g^2a^2} = -a \int dz \frac{1}{1 + z^2}$$

$$= -\sqrt{1 - n^2 - g^2} \tan^{-1} \frac{(g^2 + n^2)v + n}{g\sqrt{1 - n^2 - g^2}}. \quad (5.25)$$

For timelike heavy photons or spacelike photons, define $-1 + n^2 + g^2 = \alpha^2 > 0$, then:

$$I_{\tan}(n) = -\frac{\alpha}{2} \int dw \frac{-2g\alpha}{w^2 - g^2\alpha^2} = -\frac{\alpha}{2} \int dw \left[\frac{1}{w + g\alpha} - \frac{1}{w - g\alpha} \right]$$

$$= -\frac{\alpha}{2} [\log(w + g\alpha) - \log(w - g\alpha)]$$

$$= -\frac{\sqrt{-1 + n^2 + g^2}}{2} \log \frac{((g^2 + n^2)v + n + g\sqrt{-1 + n^2 + g^2})}{((g^2 + n^2)v + n - g\sqrt{-1 + n^2 + g^2})}. \quad (5.26)$$

This explains why the final expressions are better expressed as a case-by-case expression for the real part.

5.1.1 Final analytic expressions

Timelike, light photons

For the case of timelike, light photons (i.e. $0 < n < 1, 0 < \xi < 1$), we get:

$$\begin{aligned} J_L(v; n, \xi) = & -\frac{2(1-n^2)}{n^2 v^2} + \frac{(1-v^2)\xi^2}{v^3} \log\left(\frac{1+v}{1-v}\right) \\ & + \frac{3(1-n^2)+(1-3n^2)(1-v^2)\xi^2}{4n^3 v^3} \log\left(\frac{(1+nv)^2-(1-n^2)(1-v^2)\xi^2}{(1-nv)^2-(1-n^2)(1-v^2)\xi^2}\right) \\ & - \frac{(1-n^2)^{3/2}(1+3(1-v^2)\xi^2)}{4n^3 v^3 \xi \sqrt{1-v^2}} \log\left(\frac{1-(nv-\sqrt{1-n^2}\sqrt{1-v^2}\xi)^2}{1-(nv+\sqrt{1-n^2}\sqrt{1-v^2}\xi)^2}\right) \\ & - \frac{(1-v^2)(1+2\xi^2)\sqrt{1-\xi^2}}{2v^3 \xi} \left[\tan^{-1}\left(\frac{(\xi^2(1-n^2)+n^2)v-n}{(1-n^2)\xi\sqrt{1-\xi^2}}\right) \right. \\ & \quad \left. + \tan^{-1}\left(\frac{(\xi^2(1-n^2)+n^2)v+n}{(1-n^2)\xi\sqrt{1-\xi^2}}\right) \right] \end{aligned} \quad (5.27)$$

$$\begin{aligned} J_T(v; n, \xi) = & \frac{n^2+2}{2n^2 v^2} + \frac{(1-v^2)\xi^2}{v^3} \log\left(\frac{1+v}{1-v}\right) \\ & - \frac{3(1-n^2 v^2)+(1+3n^2)(1-v^2)\xi^2}{8n^3 v^3} \log\left(\frac{(1+nv)^2-(1-n^2)(1-v^2)\xi^2}{(1-nv)^2-(1-n^2)(1-v^2)\xi^2}\right) \\ & + \frac{\sqrt{1-n^2}(1-3n^2 v^2+2n^2+3(1+n^2)(1-v^2)\xi^2)}{8n^3 v^3 \xi \sqrt{1-v^2}} \\ & \quad \times \log\left(\frac{1-(nv-\sqrt{1-n^2}\sqrt{1-v^2}\xi)^2}{1-(nv+\sqrt{1-n^2}\sqrt{1-v^2}\xi)^2}\right) \\ & - \frac{(1-v^2)(1+2\xi^2)\sqrt{1-\xi^2}}{2v^3 \xi} \left[\tan^{-1}\left(\frac{(\xi^2(1-n^2)+n^2)v-n}{(1-n^2)\xi\sqrt{1-\xi^2}}\right) \right. \\ & \quad \left. + \tan^{-1}\left(\frac{(\xi^2(1-n^2)+n^2)v+n}{(1-n^2)\xi\sqrt{1-\xi^2}}\right) \right] \end{aligned} \quad (5.28)$$

Note that the simplification with the arctan identity

$$\arctan(x) + \arctan(y) = \arctan\left(\frac{x+y}{1-xy}\right) \quad (5.29)$$

is only valid when $xy < 1$. But, in this case, there are values where $xy > 1$, and the self-energy develops a non-physical kink if we reduce the expression with this identity.

Timelike, heavy photons

For the case of timelike, heavy photons (i.e. $0 < n < 1, \xi \geq 1$), we get:

$$\begin{aligned}
 J_L(v; n, \xi) = & -\frac{2(1-n^2)}{n^2 v^2} + \frac{(1-v^2)\xi^2}{v^3} \log\left(\frac{1+v}{1-v}\right) \\
 & + \frac{3(1-n^2) + (1-3n^2)(1-v^2)\xi^2}{4n^3 v^3} \log \left| \frac{(1+nv)^2 - (1-n^2)(1-v^2)\xi^2}{(1-nv)^2 - (1-n^2)(1-v^2)\xi^2} \right| \\
 & - \frac{(1-n^2)^{3/2}(1+3(1-v^2)\xi^2)}{4n^3 v^3 \xi \sqrt{1-v^2}} \log \left| \frac{1 - (nv - \sqrt{1-n^2}\sqrt{1-v^2}\xi)^2}{1 - (nv + \sqrt{1-n^2}\sqrt{1-v^2}\xi)^2} \right| \\
 & - \frac{(1-v^2)(1+2\xi^2)\sqrt{\xi^2-1}}{4v^3 \xi} \log \left| \frac{(v((1-n^2)\xi^2+n^2)+(1-n^2)\xi\sqrt{\xi^2-1})^2 - n^2}{(v((1-n^2)\xi^2+n^2)-(1-n^2)\xi\sqrt{\xi^2-1})^2 - n^2} \right| \quad (5.30) \\
 J_T(v; n, \xi) = & \frac{n^2+2}{2n^2 v^2} + \frac{(1-v^2)\xi^2}{v^3} \log\left(\frac{1+v}{1-v}\right) \\
 & - \frac{3(1-n^2 v^2) + (1+3n^2)(1-v^2)\xi^2}{8n^3 v^3} \log \left| \frac{(1+nv)^2 - (1-n^2)(1-v^2)\xi^2}{(1-nv)^2 - (1-n^2)(1-v^2)\xi^2} \right| \\
 & + \frac{\sqrt{1-n^2}(1-3n^2 v^2 + 2n^2 + 3(1+n^2)(1-v^2)\xi^2)}{8n^3 v^3 \xi \sqrt{1-v^2}} \\
 & \times \log \left| \frac{1 - (nv - \sqrt{1-n^2}\sqrt{1-v^2}\xi)^2}{1 - (nv + \sqrt{1-n^2}\sqrt{1-v^2}\xi)^2} \right| \\
 & - \frac{(1-v^2)(1+2\xi^2)\sqrt{\xi^2-1}}{4v^3 \xi} \log \left| \frac{(v((1-n^2)\xi^2+n^2)+(1-n^2)\xi\sqrt{\xi^2-1})^2 - n^2}{(v((1-n^2)\xi^2+n^2)-(1-n^2)\xi\sqrt{\xi^2-1})^2 - n^2} \right| \quad (5.31)
 \end{aligned}$$

The only difference between the heavy and the light cases, apart from the absolute values for the log arguments, is the last term, which comes from I_{\tan} . Note that the expressions for the light photons are valid for the heavy photons if we take the real part only. Indeed, $\sqrt{1-\xi^2}$ is purely imaginary for heavy photons, and the last term is $\sim i \tan^{-1}(ix) \sim \tanh^{-1}(x) \sim \log(1+x) - \log(1-x)$. Then, taking the real part gives the last term of the heavy expression. However, the expression for the heavy case is not valid for the light case, because there is a change of branch cut happening at some point and the real part develops a non-physical kink.

In the end, I favored these case-by-case expressions to avoid dealing with complex expressions from which we need to take the real part, which can lead to branch cut complications.

Spacelike photons

For spacelike photons ($n > 1$), we get:

$$J_L(v; n, \xi) = \frac{2(n^2 - 1)}{n^2 v^2} - \frac{(1 - v^2)\xi^2}{v^3} \log\left(\frac{1 + v}{1 - v}\right) \\ + \frac{3(1 - n^2) - (1 - 3n^2)(1 - v^2)\xi^2}{4n^3 v^3} \log \left| \frac{(1 + nv)^2 - (n^2 - 1)(1 - v^2)\xi^2}{(1 - nv)^2 - (n^2 - 1)(1 - v^2)\xi^2} \right| \\ - \frac{(n^2 - 1)^{3/2}(1 - 3(1 - v^2)\xi^2)}{4n^3 v^3 \xi \sqrt{1 - v^2}} \log \left| \frac{1 - (nv - \sqrt{n^2 - 1}\sqrt{1 - v^2}\xi)^2}{1 - (nv + \sqrt{n^2 - 1}\sqrt{1 - v^2}\xi)^2} \right| \quad (5.32)$$

$$- \frac{(1 - v^2)(1 - 2\xi^2)\sqrt{\xi^2 + 1}}{4v^3 \xi} \log \left| \frac{(v((n^2 - 1)\xi^2 + n^2) + (n^2 - 1)\xi\sqrt{\xi^2 + 1})^2 - n^2}{(v((n^2 - 1)\xi^2 + n^2) - (n^2 - 1)\xi\sqrt{\xi^2 + 1})^2 - n^2} \right|$$

$$J_T(v; n, \xi) = \frac{n^2 + 2}{2n^2 v^2} - \frac{(1 - v^2)\xi^2}{v^3} \log\left(\frac{1 + v}{1 - v}\right) \\ - \frac{3(1 - n^2 v^2) - (1 + 3n^2)(1 - v^2)\xi^2}{8n^3 v^3} \log \left| \frac{(1 + nv)^2 - (n^2 - 1)(1 - v^2)\xi^2}{(1 - nv)^2 - (n^2 - 1)(1 - v^2)\xi^2} \right| \\ + \frac{\sqrt{n^2 - 1}(-1 + 3n^2 v^2 - 2n^2 + 3(1 + n^2)(1 - v^2)\xi^2)}{8n^3 v^3 \xi \sqrt{1 - v^2}} \quad (5.33)$$

$$\times \log \left| \frac{1 - (nv - \sqrt{n^2 - 1}\sqrt{1 - v^2}\xi)^2}{1 - (nv + \sqrt{n^2 - 1}\sqrt{1 - v^2}\xi)^2} \right| \\ - \frac{(1 - v^2)(1 - 2\xi^2)\sqrt{\xi^2 + 1}}{4v^3 \xi} \log \left| \frac{(v((n^2 - 1)\xi^2 + n^2) + (n^2 - 1)\xi\sqrt{\xi^2 + 1})^2 - n^2}{(v((n^2 - 1)\xi^2 + n^2) - (n^2 - 1)\xi\sqrt{\xi^2 + 1})^2 - n^2} \right|$$

This is similar to the heavy timelike case, except for some sign differences due to the sign of $n^2 - 1$ and the different definition of ξ in terms of g . Once again, I favored a case-by-case approach instead of having the parameter ξ be imaginary for spacelike photons and dealing with complex analysis subtleties.

5.1.2 Limits

These expressions are not well-defined for some values of the parameters, and we have to take limits in these cases. Furthermore, we want to show that with $\xi \rightarrow 0$ we recover the on-shell equations of Chapter 4.

Limits on ξ

Taking the limit $\xi \rightarrow 0$ of the timelike-light expression or of the spacelike expression, we recover $J^{\text{On}}(v)$, as we should:

$$J_L \rightarrow \frac{3}{v^2} \left(\frac{1-n^2}{n^2} \right) \left[\frac{1}{2nv} \log \left| \frac{1+nv}{1-nv} \right| - 1 \right] \quad (5.34a)$$

$$J_T \rightarrow \frac{3}{2v^2} \left[\frac{1}{n^2} - \left(\frac{1-n^2v^2}{n^2} \right) \frac{1}{2nv} \log \left| \frac{1+nv}{1-nv} \right| \right] \quad (5.34b)$$

The $\xi = 1$ case is only a limit for timelike light expression, and it yields the timelike heavy expression evaluated at $\xi = 1$. Thus, $J(v; n, \xi)$ remains continuous at $\xi = 0$ and at $\xi = 1$ despite the case-by-case definition.

Limits on n

The $n \rightarrow 0$ limit, equivalent to $k = 0$, is, for light timelike photons:

$$J_{L,T} \rightarrow \frac{1}{v^2} + \frac{(1-v^2)\xi^2}{v^3} \log \left(\frac{1+v}{1-v} \right) - \frac{(1-v^2)(1+2\xi^2)\sqrt{1-\xi^2}}{v^3\xi} \tan^{-1} \left(\frac{v\xi}{\sqrt{1-\xi^2}} \right) \quad (5.35)$$

and for heavy timelike photons:

$$J_{L,T} \rightarrow \frac{1}{v^2} + \frac{(1-v^2)\xi^2}{v^3} \log \left(\frac{1+v}{1-v} \right) - \frac{(1-v^2)(1+2\xi^2)\sqrt{\xi^2-1}}{2v^3\xi} \log \left| \frac{v\xi + \sqrt{\xi^2-1}}{v\xi - \sqrt{\xi^2-1}} \right| \quad (5.36)$$

The $n \rightarrow \infty$ limit, equivalent to $\omega = 0$, is, for spacelike photons:

$$\begin{aligned} J_L &\rightarrow \frac{2}{v^2} - \frac{(1-v^2)\xi^2}{v^3} \log\left(\frac{1+v}{1-v}\right) \\ &\quad - \frac{1-3(1-v^2)\xi^2}{2v^3\xi\sqrt{1-v^2}} \log\left|\frac{v-\sqrt{1-v^2}\xi}{v+\sqrt{1-v^2}\xi}\right| \\ &\quad - \frac{(1-v^2)(1-2\xi^2)\sqrt{\xi^2+1}}{2v^3\xi} \log\left|\frac{v\sqrt{\xi^2+1}+\xi}{v\sqrt{\xi^2+1}-\xi}\right| \end{aligned} \quad (5.37)$$

$$\begin{aligned} J_T &\rightarrow \frac{1}{2v^2} - \frac{(1-v^2)\xi^2}{v^3} \log\left(\frac{1+v}{1-v}\right) \\ &\quad - \frac{2-3v^2-3\xi^2(1-v^2)}{4v^3\xi\sqrt{1-v^2}} \log\left|\frac{v-\sqrt{1-v^2}\xi}{v+\sqrt{1-v^2}\xi}\right| \\ &\quad - \frac{(1-v^2)(1-2\xi^2)\sqrt{\xi^2+1}}{2v^3\xi} \log\left|\frac{v\sqrt{\xi^2+1}+\xi}{v\sqrt{\xi^2+1}-\xi}\right| \end{aligned} \quad (5.38)$$

Finally, the $n \rightarrow 1$ limit, equivalent to $\omega = k$, results in the Braaten and Segel expression (evaluated at $n = 1$) for all three cases. Recall that, for consistency, if $n = 1$, then $\xi = 0$, so this limiting case makes sense. Once again, $J(v; n, \xi)$ is continuous at $n = 1$ despite the case-by-case approach.

Limits on v

Taking the limit $v \rightarrow 0$ yields:

$$J_L \rightarrow \frac{1-n^2}{1-|1-n^2|\xi^2} \quad J_T \rightarrow \frac{1}{1-|1-n^2|\xi^2} \quad (5.39)$$

Finally, in the limit $v \rightarrow 1$, we recover $J^{\text{On}}(v)$ once again, for all three cases.

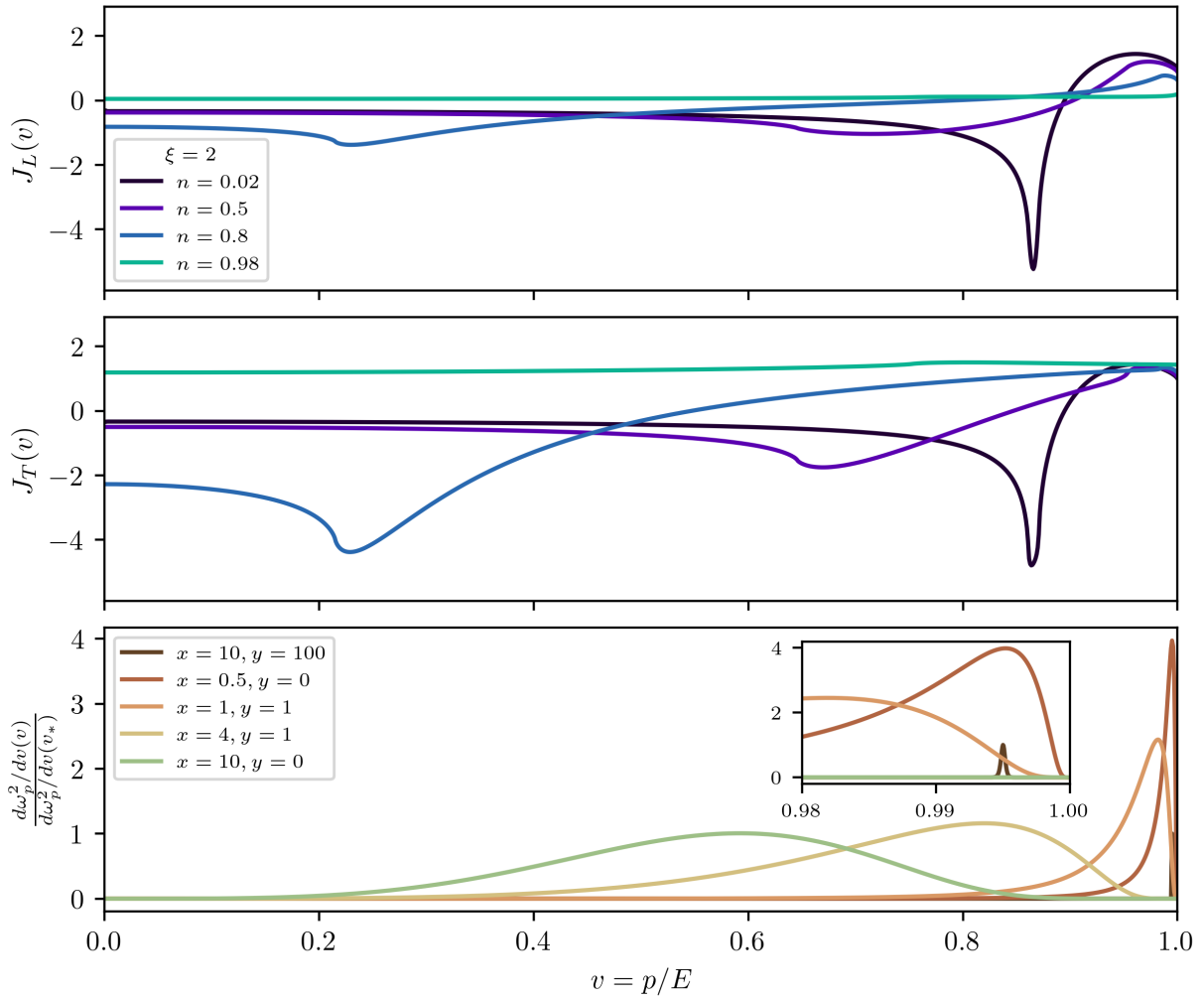


Figure 5.1: Plots of $J(v)$ for $\xi = 2$ and some values of n (top and middle), and plots of $d\omega_p^2/dv$ for some values of x and y (bottom), as a function of v . The bottom panel is the same as in Figure 4.3. This time, $J(v)$ is less flat than in the on-shell case.

5.1.3 Comparing analytic approximations to numerical results

We now turn to the analytic approximation of the real part of the self-energy. Recall that this approximation is given by

$$\Pi_a = \int_0^1 dv J_a(v) \frac{d\omega_p^2}{dv} \simeq \omega_p^2 J_a(v^*) \quad (5.40)$$

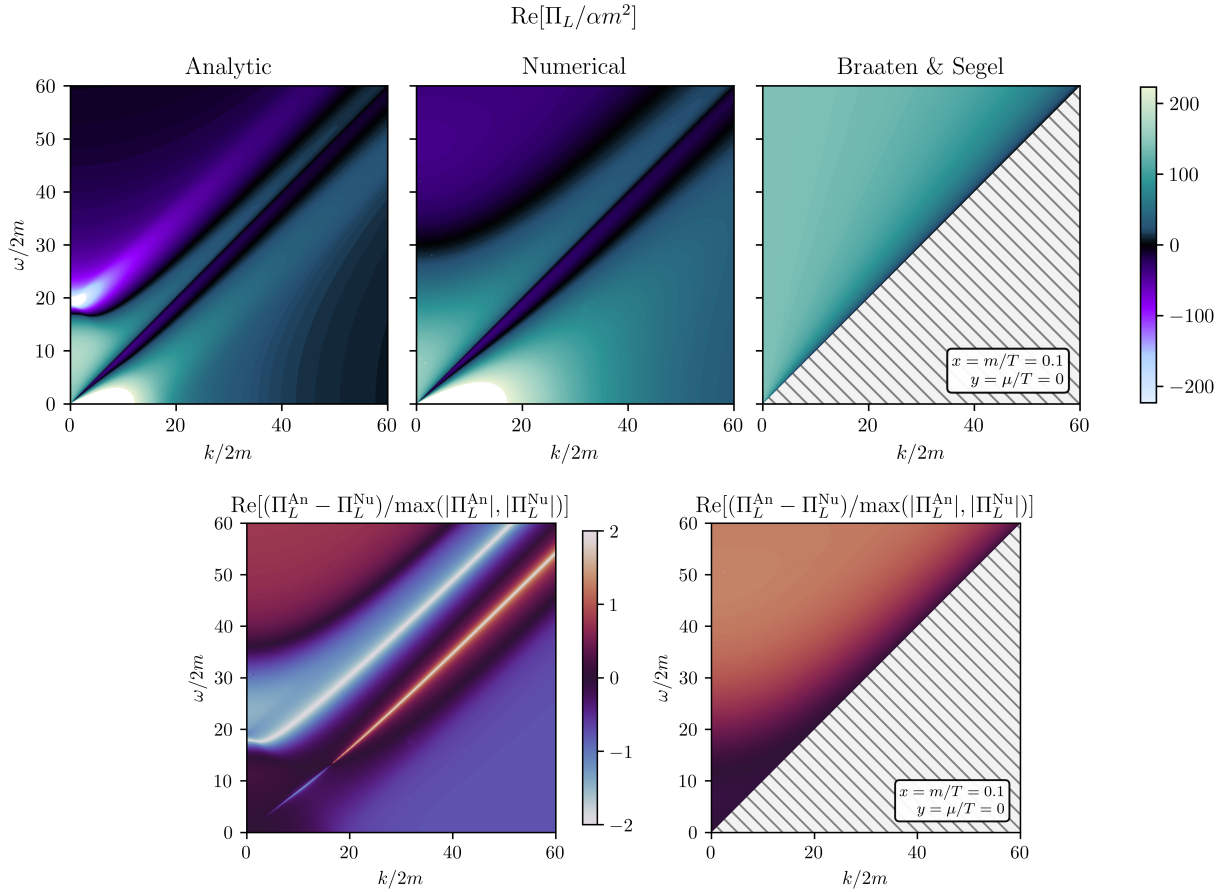


Figure 5.2: Plots of the real part of the self-energy as a function of ω and k for L modes in the regime where $x = 0.1$ and $y = 0$. The self-energy is computed with the new analytic approximation $\Pi_a \simeq \omega_p^2 J(v_*)$ (top left panel), with the numerical integral of $F_a(v)$ (top middle panel), and with the expression from Braaten and Segel [1] (top right panel). The bottom panels show a ratio to assess the discrepancy between the approximations and the numerical evaluation, with the new analytic approximation on the bottom left and the one from Braaten and Segel [1] on the bottom right.

provided that, around v^* , $J(v)$ is flat enough and that $d\omega_p^2/dv$ is sharply peaked enough.

In Figure 5.1, $J(v)$ is plotted for $\xi = 2$, and some values of n which are the same as in the on-shell plots of Figure 4.3. The values of $x = m/T$ and $y = \mu/T$ for the plots of $d\omega_p^2/dv$ in the bottom panel are also the same as in Figure 4.3. The function $J(v)$ is visually not as flat as in the on-shell case. Take for example $J(v)$ for $n = 0.02$ and $d\omega_p^2/dv$ for $x = 4, y = 1$. The maximum of $d\omega_p^2/dv$, at v_* , is aligned with a deep negative kink in $J(v)$. Therefore,

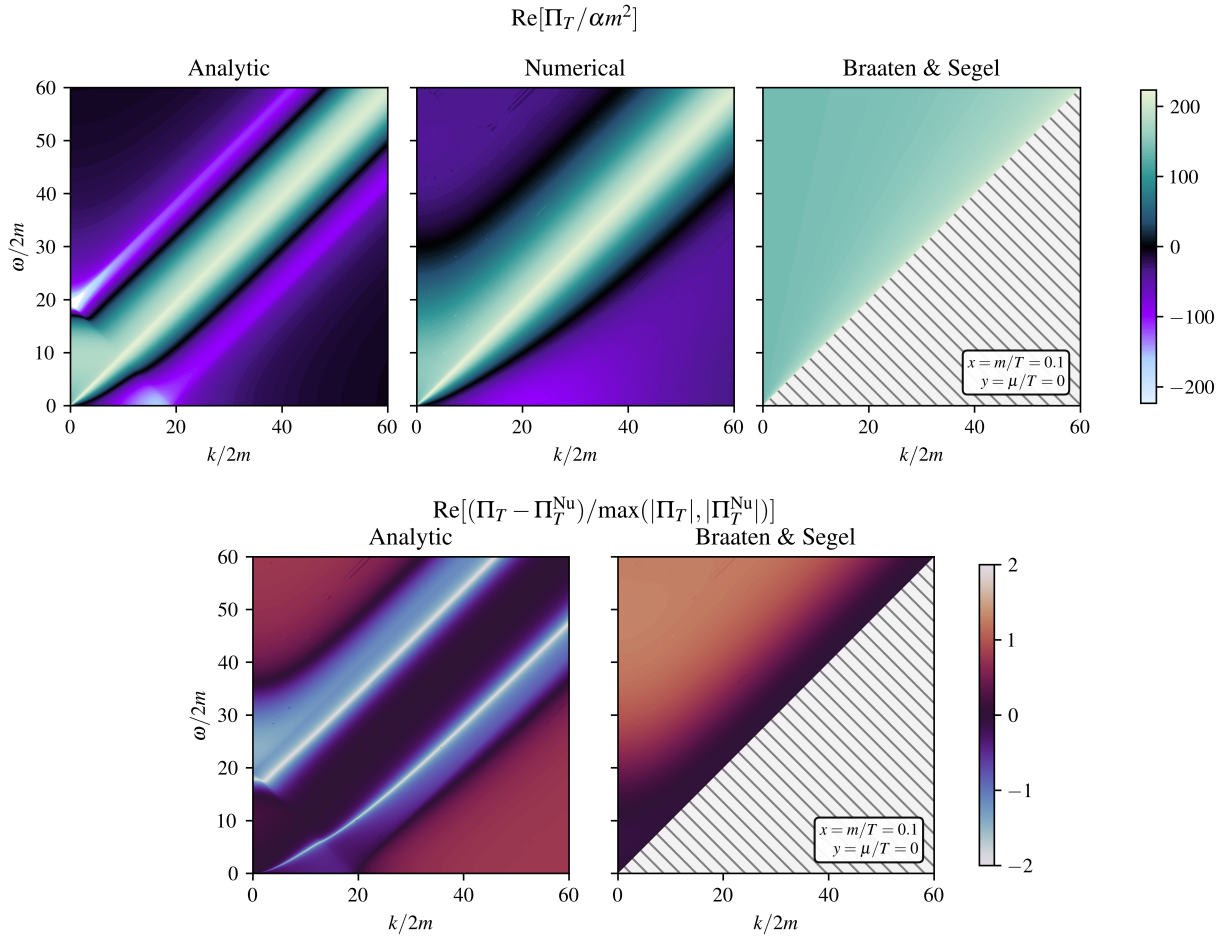


Figure 5.3: Plots of the real part of the self-energy as a function of ω and k for T modes in the regime where $x = 0.1$ and $y = 0$. The display is the same as Figure 5.2.

evaluating $J(v_*)$ and taking that out of the integral surely underestimates the actual value of the self-energy for these values of the parameters. However, for other values of n , the kink is elsewhere (e.g., $n = 0.8$), or altogether absent (e.g., $n = 0.98$). Therefore, there are some precise values of the parameters (x, y, n and ξ , or equivalently T, μ, ω and k), where this approximation is not accurate, but it is a good approximation otherwise.

Figures 5.2, 5.3, 5.4, and 5.5 show the real part of the self-energy in the ω and k plane, for two different regimes (i.e., values of $x = m/T$ and $y = \mu/T$), and for L and T modes. The energy and momentum are in units of $2m$. This was chosen to remain agnostic on the exact

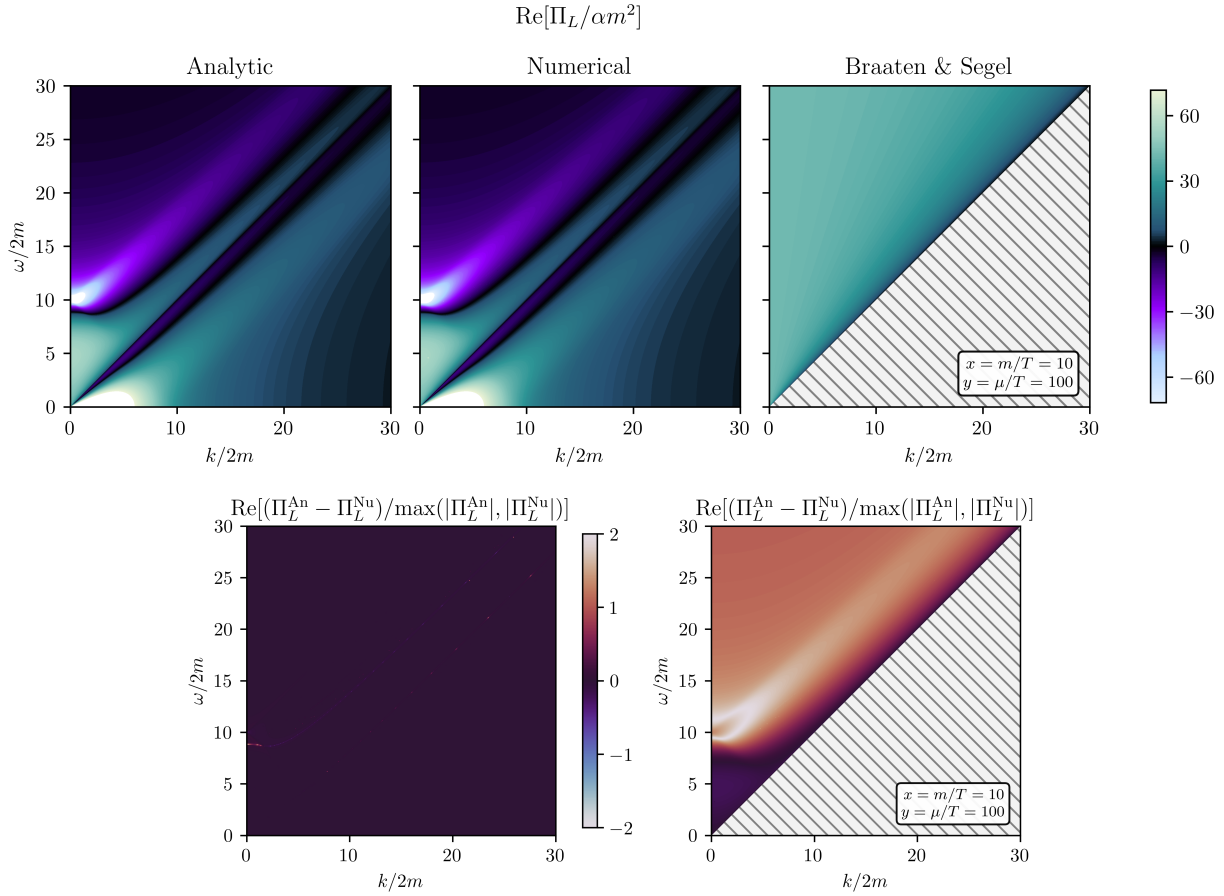


Figure 5.4: Plots of the real part of the self-energy as a function of ω and k for L modes in the regime where $x = 10$, $y = 100$. The display is the same as Figure 5.2.

thermal correction to the fermion mass (or even to the type of fermions in the loop). The self-energy is in units of αm^2 for the same reason. In each plot, the analytical approximation is on the top left panel, the numerical evaluation of the self-energy is in the top middle one, and the value of the expression from Braaten and Segel is on the top right one. The numerical integral can be considered to be the actual value of the self-energy, modulo some small numerical uncertainties (the error bars of which were too small to appear on plots). To quantify the discrepancy between each analytical approximation and the numerical value, the ratio $(\Pi - \Pi^{\text{Nu}})/\max(|\Pi|, |\Pi^{\text{Nu}}|)$ is shown on the bottom panels¹, with Π being the analytic

¹The more intuitive ratio $(\Pi - \Pi^{\text{Nu}})/|\Pi^{\text{Nu}}|$ exaggeratedly brings focus on regions of phase space where the numerical self-energy is extremely small. This artifact is due to the fact that the analytic and numerical

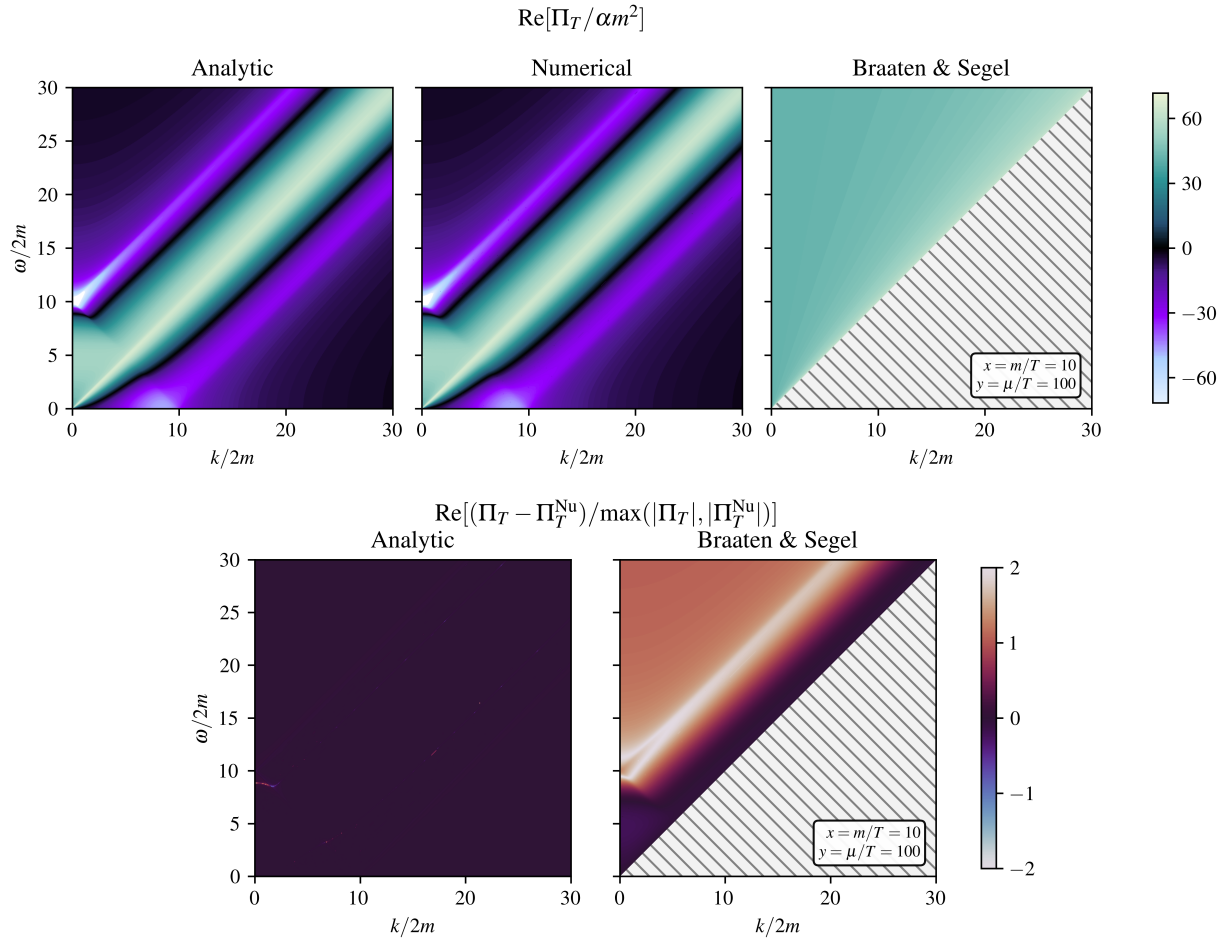


Figure 5.5: Plots of the real part of the self-energy as a function of ω and k for T modes in the regime where $x = 10$, $y = 100$. The display is the same as Figure 5.2.

approximation I developed on the left, and the one from Braaten and Segel on the right.

The first thing that is striking is that the Braaten and Segel expression only approximates the self-energy correctly in the region close to the on-shell line, i.e., in the neighborhood of $\omega \sim k$. This is not a quantitative statement, but more a qualitative observation that the ratio plots on the bottom right panel in each of these figures show that the Braaten and Segel expressions faithfully approximate the numerical result only in a region surrounding the $\omega = k$ line, where the on-shell dispersion relation lines lie, see for example Figure 4.4.

expressions both cross zero, but not at the exact same values. The ratio $(\Pi - \Pi^{\text{Nu}})/\max(|\Pi|, |\Pi^{\text{Nu}}|)$ was chosen because it correctly accounts for the discrepancies while avoiding these problems.

Quantitatively, we know that the Braaten and Segel expression holds in regions of phase space where the momentum is soft, i.e. where $\xi \ll 1$ (which is indeed close to the $\omega = k$ line), from the fact that we recover these expressions from the new analytic ones in the limit $\xi \rightarrow 0$ (see Section 5.1.2). However, the accuracy of these expressions in regions where $\xi \gtrsim 1$ depends on the regime, i.e. the values of T and μ , and no general quantitative statement can be made in that case. Another striking observation is the fact that the self-energy even becomes negative in some of the off-shell regions, something that isn't captured at all by the Braaten and Segel expressions.

The analytic expressions seem to better approximate the numerical result than Braaten and Segel, but their validity can differ depending on the values of the parameters. In Figures 5.2 and 5.3, there are some visible discrepancies between the analytic and numerical computations. For example, consider the top panels of Figure 5.2, which shows L modes for $x = 0.1$ and $y = 0$. We see that, at k close to 0 and $\omega/2m \simeq 20$, the analytic approximation gives a highly negative value for the self-energy, while the numerical integral shows that it is actually very positive. The bottom left panel indeed shows that the analytic expression overestimates or underestimates the numerical one in this region and in a lot of parameter space. The same comments apply for Figure 5.3, showing T modes for the same regime. Note that I have verified that the discrepancy isn't due to errors in the expression for the analytic approximation, see Appendix A for details.

Figures 5.4 and 5.5 show a regime where the analytic approximation follows much more closely the numerical computation. In both figures, the bottom left panel indeed shows that there are extremely few discrepancies. Again, the bottom right one clearly shows that the Braaten and Segel expression is only valid in a region close to the on-shell dispersion relation.

The accuracy of the analytic approximation to reproduce the numerical evaluation of the self-energy seems to depend on the regime, i.e., on the value of T and μ . As pointed out, there can be significant discrepancies when evaluating the self-energy at a specific value of

ω , k , T and μ . In the case presented here, it is the more relativistic case ($x \ll 1$) which is less accurate. These discrepancies between the analytic and numerical evaluations comes from the fact that $J(v)$ is not generally flat, as can be seen in Figure 4.3. However, despite these discrepancies, we can see from the top panels of Figures 5.2 to 5.5 that the general structure in phase space is captured by these analytical approximations compared to Braaten and Segel. This crucially includes the negative self-energy in some parts of phase space. Thus, one could expect that using this analytical approximation to integrate over big regions of phase space still gives an accurate result despite the discrepancies. This is also the kind of situation when analytic approximations are most useful to reduce computing time. In summary, one should probably not use these analytic approximations to compute the self-energy for a single specific value of the parameters. However, the use of these analytic approximations for integration over phase space is still very promising. A more quantitative statement about this would require using these approximations in an actual example, something we leave for future work.

5.2 Imaginary part

To compute the imaginary part, we use the cutting rules presented in Chapter 3. More specifically, we use Equation (3.53) combined with Equation (3.51) applied to the Feynman diagram of Figure 4.1. The only cut possible is cutting the fermion loop in half. From this, there are eight processes contributing to the imaginary part: four photon absorption processes and four photon emission processes. However, the matrix elements are the same

for each process and its reverse due to CP invariance. We get:

$$\begin{aligned} \text{Im } \Pi = -\frac{1}{2} \int \frac{d^3 p_1}{2E_1} \frac{d^3 p_2}{2E_2} (2\pi)^4 & \left\{ \delta^{(4)}(k^\mu - p_1^\mu - p_2^\mu) \left| \mathcal{M}_{\gamma \rightarrow e_1^- e_2^+} \right|^2 [(1-f_1)(1-\bar{f}_2) - f_1 \bar{f}_2] \right. \\ & + \delta^{(4)}(k^\mu + p_1^\mu - p_2^\mu) \left| \mathcal{M}_{\gamma e_1^+ \rightarrow e_2^+} \right|^2 [\bar{f}_1(1-\bar{f}_2) - (1-\bar{f}_1)\bar{f}_2] \\ & + \delta^{(4)}(k^\mu + p_1^\mu - p_2^\mu) \left| \mathcal{M}_{\gamma e_1^- \rightarrow e_2^-} \right|^2 [f_1(1-f_2) - (1-f_1)f_2] \\ & \left. + \delta^{(4)}(k^\mu + p_1^\mu + p_2^\mu) \left| \mathcal{M}_{\gamma e_1^- e_2^+ \rightarrow 0} \right|^2 [f_1 \bar{f}_2 - (1-f_1)(1-\bar{f}_2)] \right\}, \end{aligned} \quad (5.41)$$

where f_i is short for $f(E_i)$. The first process represents the decay of a photon to a positron-electron pair, and is only kinematically allowed for timelike photons with positive energy $\omega > 0$ and with $K^2 > 4m^2$. The last process is an absorption to vacuum, and is only allowed for timelike photons with negative energy $\omega < 0$ and, again, with $K^2 > 4m^2$. The second and third processes correspond to Cherenkov absorption, for positrons and electrons, respectively. Cherenkov absorption $\gamma e \rightarrow e$ is only allowed for spacelike photons, i.e. with $K^2 < 0$. From here, we can judiciously integrate either p_1 or p_2 using the 3D delta functions, depending on whether the term is proportional to f_1 or f_2 . The remaining momentum switches name to just \mathbf{p} . We resolve the remaining energy delta functions with

$$\delta(\omega - E_p - E_{k-p}) = \frac{E_{k-p}}{pk} \delta(\cos \theta - \cos \theta_1) \Theta(K^2 - 4m^2) \Theta(\omega) \quad (5.42)$$

for the first one, and similar expressions for the other three terms. Here, $\Theta(x)$ is the Heaviside step function, which keeps track of the regime of validity for each process as discussed above. The angle θ is defined through $\mathbf{p} \cdot \mathbf{k} = pk \cos \theta$, and the explicit values of $\cos \theta_i$ for each of the four processes is given by

$$\cos \theta_1 = \cos \theta_3 = \frac{-K^2 + 2E\omega}{2pk}, \quad \cos \theta_2 = \cos \theta_4 = \frac{K^2 + 2E\omega}{2pk}. \quad (5.43)$$

We then integrate the azimuthal angle to get

$$\begin{aligned} \text{Im } \Pi = -\frac{1}{16\pi k} \int dp \frac{p}{E_p} d\cos\theta & \left\{ \delta(\cos\theta - \cos\theta_1) |\mathcal{M}_-|^2 [1 - f_p - \bar{f}_p] \Theta(K^2 - 4m^2) \Theta(\omega) \right. \\ & + \delta(\cos\theta - \cos\theta_2) |\mathcal{M}_+|^2 [f_p + \bar{f}_p] \Theta(-K^2) \\ & + \delta(\cos\theta - \cos\theta_3) |\mathcal{M}_-|^2 [f_p + \bar{f}_p] \Theta(-K^2) \\ & \left. + \delta(\cos\theta - \cos\theta_4) |\mathcal{M}_+|^2 [1 - f_p - \bar{f}_p] \Theta(K^2 - 4m^2) \Theta(-\omega) \right\}, \end{aligned} \quad (5.44)$$

with these explicit matrix elements:

$$|\mathcal{M}_-|^2 = 16\pi\alpha P_{\mu\nu}^a (P^\mu K^\nu + P^\nu K^\mu - 2P^\mu P^\nu - (P \cdot K)\eta^{\mu\nu}), \quad (5.45a)$$

$$|\mathcal{M}_+|^2 = 16\pi\alpha P_{\mu\nu}^a (P^\mu K^\nu + P^\nu K^\mu + 2P^\mu P^\nu - (P \cdot K)\eta^{\mu\nu}). \quad (5.45b)$$

To evaluate these at $\cos\theta = \cos\theta_i$ for $i = 1 \dots 4$, we only need to know that the delta functions are equivalent to the following replacement rules:

$$P \cdot K = K^2/2 \quad \text{for } \theta_1 \text{ and } \theta_3, \quad (5.46a)$$

$$P \cdot K = -K^2/2 \quad \text{for } \theta_2 \text{ and } \theta_4. \quad (5.46b)$$

Using these, we get explicit expressions for the L and T matrix elements:

$$|\mathcal{M}_-^L|^2 = 8\pi\alpha \frac{K^2}{k^2} (4E\omega - 4E^2 - K^2) \quad (5.47a)$$

$$|\mathcal{M}_+^L|^2 = 8\pi\alpha \frac{K^2}{k^2} (4E\omega + 4E^2 + K^2) \quad (5.47b)$$

$$|\mathcal{M}_-^T|^2 = 8\pi\alpha \left[K^2 + 2m^2 - \frac{K^2}{2k^2} (4E\omega - 4E^2 - K^2) \right] \quad (5.47c)$$

$$|\mathcal{M}_+^T|^2 = 8\pi\alpha \left[-K^2 - 2m^2 - \frac{K^2}{2k^2} (4E\omega + 4E^2 + K^2) \right] \quad (5.47d)$$

Furthermore, the delta functions place bounds on the allowed values of p (or equivalently, E_p). These bounds can be derived using the explicit expressions for θ_i from Equation (5.43) and evaluating them at $\cos \theta_i = \pm 1$. This yields:

$$\begin{aligned} \text{Im } \Pi = -\frac{1}{16\pi k} & \left\{ \int_{E_{+-}}^{E_{++}} dE |\mathcal{M}_-|^2 [1 - f_p - \bar{f}_p] \Theta(K^2 - 4m^2) \Theta(\omega) \right. \\ & + \int_{E_{-+}}^{\infty} dE |\mathcal{M}_+|^2 [f_p + \bar{f}_p] \Theta(-K^2) \\ & + \int_{E_{++}}^{\infty} dE |\mathcal{M}_-|^2 [f_p + \bar{f}_p] \Theta(-K^2) \\ & \left. + \int_{E_{--}}^{E_{-+}} dE |\mathcal{M}_+|^2 [1 - f_p - \bar{f}_p] \Theta(K^2 - 4m^2) \Theta(-\omega) \right\}, \end{aligned} \quad (5.48)$$

where

$$E_{\pm\pm} = \frac{\omega}{2} \left[\pm 1 \pm n \sqrt{1 - \frac{4m^2}{K^2}} \right]. \quad (5.49)$$

Notice the bounds of integration are different for each of the four processes. To express these with dimensionless parameters, including the previously defined n and g , we further define

$$D_{\pm} = \frac{|\mathcal{M}_{\pm}|^2}{16\pi\alpha m \omega n}, \quad \gamma = \frac{E}{m} = \frac{1}{\sqrt{1 - v^2}}, \quad (5.50)$$

so that

$$\begin{aligned} \text{Im } \Pi = -\alpha m^2 & \left\{ \int_{\gamma_{+-}}^{\gamma_{++}} d\gamma D_- [1 - f_p - \bar{f}_p] \Theta(K^2 - 4m^2) \Theta(\omega) \right. \\ & + \int_{\gamma_{-+}}^{\infty} d\gamma D_+ [f_p + \bar{f}_p] \Theta(-K^2) \\ & + \int_{\gamma_{++}}^{\infty} d\gamma D_- [f_p + \bar{f}_p] \Theta(-K^2) \\ & \left. + \int_{\gamma_{--}}^{\gamma_{-+}} d\gamma D_+ [1 - f_p - \bar{f}_p] \Theta(K^2 - 4m^2) \Theta(-\omega) \right\}. \end{aligned} \quad (5.51)$$

Explicitly,

$$D_{\pm}^L = \pm \frac{1-n^2}{n^3} \left(g \pm 2\gamma + \frac{1-n^2}{g} \gamma^2 \right), \quad (5.52a)$$

$$D_{\pm}^T = \mp \left(\frac{1-n^2+2g^2}{2ng} + \frac{1-n^2}{2n^3} \left(g \pm 2\gamma + \frac{1-n^2}{g} \gamma^2 \right) \right), \quad (5.52b)$$

and

$$\gamma_{\pm\pm} = \frac{g}{1-n^2} \left[\pm 1 \pm n \sqrt{1 - \frac{1-n^2}{g^2}} \right]. \quad (5.53)$$

Once again, we integrate by parts to get an analytical approximation. First, we define

$$\Gamma(\gamma) = \int_0^\gamma d\gamma' D_-(\gamma') \quad \text{and} \quad \tilde{\Gamma}(\gamma) = \int_0^\gamma d\gamma' D_+(\gamma') \quad (5.54)$$

which are, explicitly:

$$\Gamma_L = -\frac{1-n^2}{n^3} \left(g\gamma - \gamma^2 + \frac{1-n^2}{3g} \gamma^3 \right), \quad (5.55a)$$

$$\tilde{\Gamma}_L = +\frac{1-n^2}{n^3} \left(g\gamma + \gamma^2 + \frac{1-n^2}{3g} \gamma^3 \right), \quad (5.55b)$$

and

$$\Gamma_T = + \left(\frac{1-n^2+2g^2}{2ng} \gamma + \frac{1-n^2}{2n^3} \left(g\gamma - \gamma^2 + \frac{1-n^2}{3g} \gamma^3 \right) \right), \quad (5.56a)$$

$$\tilde{\Gamma}_T = - \left(\frac{1-n^2+2g^2}{2ng} \gamma + \frac{1-n^2}{2n^3} \left(g\gamma + \gamma^2 + \frac{1-n^2}{3g} \gamma^3 \right) \right). \quad (5.56b)$$

So far this is valid for any sign of ω and any value of K^2 . We will now restrict ourselves to $\omega > 0$, once again without loss of generality, since the imaginary part of the self-energy is simply odd under $\omega \rightarrow -\omega$. This eliminates the fourth integral automatically. Furthermore, we will again split this into cases, timelike and spacelike photons. With these assumptions,

we can also conveniently define:

$$\gamma_+ = \frac{g}{1-n^2} \left[1 + n \sqrt{1 - \frac{1-n^2}{g^2}} \right], \quad (5.57a)$$

$$\gamma_- = \left| \frac{g}{1-n^2} \left[1 - n \sqrt{1 - \frac{1-n^2}{g^2}} \right] \right|. \quad (5.57b)$$

Indeed, both γ_{+-} and γ_{-+} are equal to γ_- for the cases at hand.

5.2.1 Final analytic expressions

Timelike photons

For timelike photons, $K^2 > 0$, only the first integral survives. We get

$$\text{Im } \Pi = -\alpha m^2 \int_{\gamma_-}^{\gamma_+} d\gamma D_- [1 - f_p - \bar{f}_p] \Theta(K^2 - 4m^2). \quad (5.58)$$

In terms of ξ , the Heaviside function has support only when $\xi > 1$. This is logical because this is the regime where the decay $\gamma \rightarrow e^+e^-$ is allowed. This is precisely the imaginary part (non-physical for on-shell photons) that Braaten and Segel avoided with their approximation. Therefore, the imaginary part is exactly zero for timelike light photons ($0 < n < 1, \xi < 1$). For timelike heavy photons ($\xi > 1$), we integrate by parts, but the boundary terms do not vanish:

$$\text{Im } \Pi = -\alpha m^2 [\Gamma(\gamma_+) (1 - f_+ - \bar{f}_+) - \Gamma(\gamma_-) (1 - f_- - \bar{f}_-)] - \alpha m^2 \int_{\gamma_-}^{\gamma_+} d\gamma \Gamma(\gamma) \frac{d}{d\gamma} (f + \bar{f}). \quad (5.59)$$

Here, f_{\pm} are shorthands for f evaluated at γ_{\pm} . We then once again change to integration over v and use the sharp peak approximation:

$$\begin{aligned}\text{Im } \Pi - (\text{boundary terms}) &= -\alpha m^2 \int_{v_-}^{v_+} dv \Gamma(\gamma) \frac{d}{dv} (f + \bar{f}) \\ &\simeq -\alpha m^2 \Gamma(\gamma_*) \int_{v_-}^{v_+} dv \frac{d}{dv} (f + \bar{f}) \\ &= -\alpha m^2 \Gamma(\gamma_*) [f_+ + \bar{f}_+ - f_- - \bar{f}_-],\end{aligned}\quad (5.60)$$

i.e., in summary

$$\text{Im } \Pi \simeq -\alpha m^2 \{ [\Gamma(\gamma_+) - \Gamma(\gamma_-)] + (f_+ + \bar{f}_+) [\Gamma(\gamma^*) - \Gamma(\gamma_+)] + (f_- + \bar{f}_-) [\Gamma(\gamma_-) - \Gamma(\gamma^*)] \}. \quad (5.61)$$

Here, $\gamma^* = 1/\sqrt{1-v^*}$, but if it falls out of the integration limits, we need to take it to be one of those limits instead, since this is where the integrand will have the most support. Thus we define

$$\bar{\gamma}^* = \begin{cases} \gamma_- & \text{if } \gamma^* < \gamma_- \\ \gamma^* = \frac{1}{\sqrt{1-v_*^2}} & \text{if } \gamma_- \leq \gamma^* \leq \gamma_+ \\ \gamma_+ & \text{if } \gamma^* > \gamma_+ \end{cases} \quad (5.62)$$

Finally, the difference $\Gamma(\gamma_+) - \Gamma(\gamma_-)$ can be evaluated to a concise expression. We finally get this expression for the timelike heavy photons:

$$\begin{aligned}\text{Im } \Pi \simeq -\alpha m^2 &\left\{ \frac{2}{3} (1 + 2\xi^2) \sqrt{1 - \frac{1}{\xi^2}} \right. \\ &\left. + (f_+ + \bar{f}_+) [\Gamma(\bar{\gamma}^*) - \Gamma(\gamma_+)] + (f_- + \bar{f}_-) [\Gamma(\gamma_-) - \Gamma(\bar{\gamma}^*)] \right\}.\end{aligned}\quad (5.63)$$

Note that there are implicit $a = L, T$ subscripts in all the expressions of this section, but they have been omitted to avoid clutter.

Spacelike photons

In this case, only the second and third integral survive:

$$\begin{aligned} \text{Im } \Pi = -\alpha m^2 & \left\{ + \int_{\gamma_-}^{\infty} d\gamma D_+ [f_p + \bar{f}_p] \Theta(-K^2) \right. \\ & \left. + \int_{\gamma_+}^{\infty} d\gamma D_- [f_p + \bar{f}_p] \Theta(-K^2) \right\}. \end{aligned} \quad (5.64)$$

Using the same steps as in the timelike case, we get

$$\text{Im } \Pi \simeq -\alpha m^2 \left\{ (f_+ + \bar{f}_+) [\Gamma(\gamma_+^*) - \Gamma(\gamma_+)] + (f_- + \bar{f}_-) [\tilde{\Gamma}(\gamma_-^*) - \tilde{\Gamma}(\gamma_-)] \right\}, \quad (5.65)$$

where this time the prescription is

$$\gamma_{\pm}^* = \begin{cases} \gamma_{\pm} & \text{if } \gamma^* < \gamma_{\pm} \\ \gamma^* = \frac{1}{\sqrt{1 - v_*^2}} & \text{if } \gamma^* \geq \gamma_{\pm} \end{cases} \quad (5.66)$$

5.2.2 Limits

The only formal limits we need to consider are on the value of n . First, for the timelike (heavy) photons, we take $n \rightarrow 0$. This is equivalent to $k \rightarrow 0$, meaning we are in the rest frame of the photon. In this case, the delta function imposes a value on p instead of $\cos \theta$. However, we can't define $\cos \theta$ as the angle between \mathbf{p} and \mathbf{k} anymore. In fact, this also means that there is no distinction between L and T modes anymore in this limit. The matrix elements for the decay must therefore be averaged over all three degrees of freedom. It can be evaluated exactly to:

$$\text{Im } \Pi_{L,T}(n \rightarrow 0) = -\alpha m^2 \frac{2}{3} (1 + 2\xi^2) \sqrt{1 - \frac{1}{\xi^2}} (1 - f(E = \omega/2) - \bar{f}(E = \omega/2)). \quad (5.67)$$

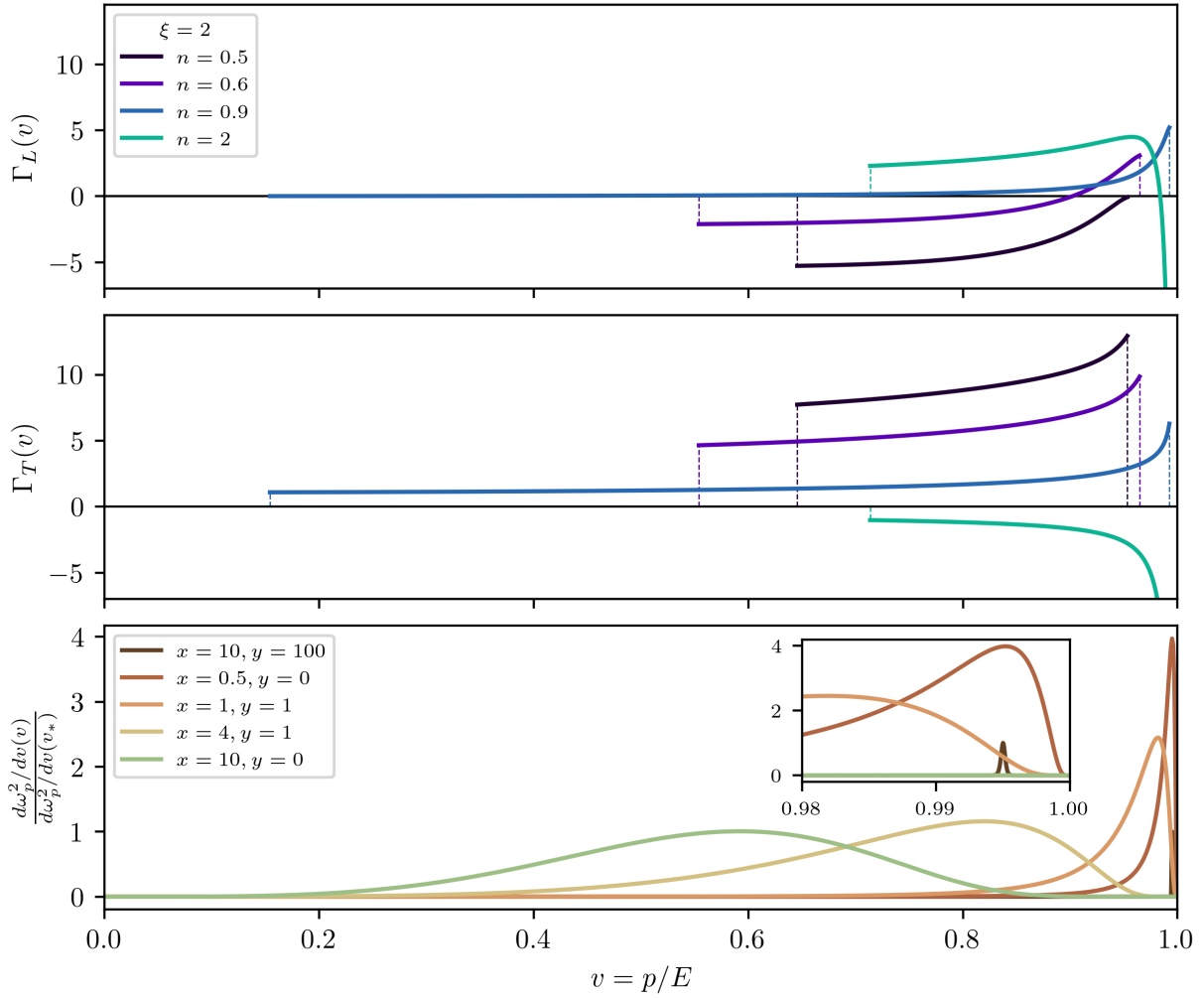


Figure 5.6: Plots of $\Gamma(v)$ for $\xi = 2$ and some values of n (top and middle), and plots of $d\omega_p^2/dv$ for some values of x and y (bottom), as a function of v . For n corresponding to timelike photons, $n < 1$, $\Gamma(v)$ is only plotted in the relevant interval v_- to v_+ , shown in dashed vertical lines. For the spacelike photons, $\Gamma(v)$ is plotted from v_- to 1. The bottom panel is the same as in Figure 4.3.

It is possible to get this result directly from Equation (5.63) instead by evaluating it at $f_{\pm} = f(E = \omega/2)$. Then, this expression only depends on the difference $\Gamma(\gamma_+) - \Gamma(\gamma_-)$, which is independent of n .

For spacelike photons, taking $n \rightarrow 1$ takes γ_+ and γ_- to infinity, and the integral for the imaginary part just vanishes, so $\text{Im } \Pi_{L,T}(n \rightarrow 1) = 0$. The approximation is still valid,

because in this case $\gamma_* < \gamma_{\pm} = \infty$ so both terms vanish. Taking $n \rightarrow \infty$ is equivalent to taking $\omega \rightarrow 0$. In this case, both γ_+ and γ_- evaluate to the same value, so the imaginary part becomes only one integral of $D_+ + D_-$. However, it turns out that $D_+ + D_- = 0$ when $\omega = 0$, so $\text{Im } \Pi_{L,T}(n \rightarrow \infty) = 0$.

Taking $\xi \rightarrow 1$ for the timelike case isn't a limit, but it is worth pointing out that the imaginary part vanishes because $\gamma_+ = \gamma_-$ in this case. The case of $\xi \rightarrow 0$ for the spacelike photons is equivalent to $n \rightarrow 1$, which has already been discussed.

Finally, taking $v_* = 0$ is well-defined; it just means that $\gamma_* = 1$ and there is no complication. Taking $v_* \rightarrow 1$ means taking $\gamma_* \rightarrow \infty$. In the timelike case, this means that $\gamma_* > \gamma_+$, so the approximation is still well defined. The spacelike case, however, isn't well-defined unfortunately, and goes to infinity. This is an artifact more than a physical fact. Taking $v = 1$ means that electrons are exactly relativistic and one should then also take the limit $m \rightarrow 0$, which changes the computation completely (for example γ isn't a well-defined integration variable anymore). In reality, v is never exactly 1 for electrons and positrons, and all of this only means that the limit $v \rightarrow 1$ isn't a helpful mathematical limit here.

5.2.3 Comparing analytic approximations to numerical results

Figure 5.6 shows $\Gamma(v)$ as a function of v for $\xi = 2$ and some values of n . It is similar to Figure 5.1. The point is to assess if taking $\Gamma(v_*)$ out of the integral is a good approximation. We can see from this plot that Γ is relatively flat, especially for lower values of v . It is much less flat for v close to 1. However, when v_* is close to 1, this is compensated by the fact that $d\omega_p^2/dv$ is much narrower, as can be seen in the lower panel. Overall, this suggests that the approximation should work correctly, and that it might be better in some regimes than others, like for the real part.

Figures 5.7, 5.8, 5.9, and 5.10 show the imaginary part of the self-energy for the same regimes and modes as Figures 5.2, 5.3, 5.4, and 5.5 respectively. The dashed region indicates

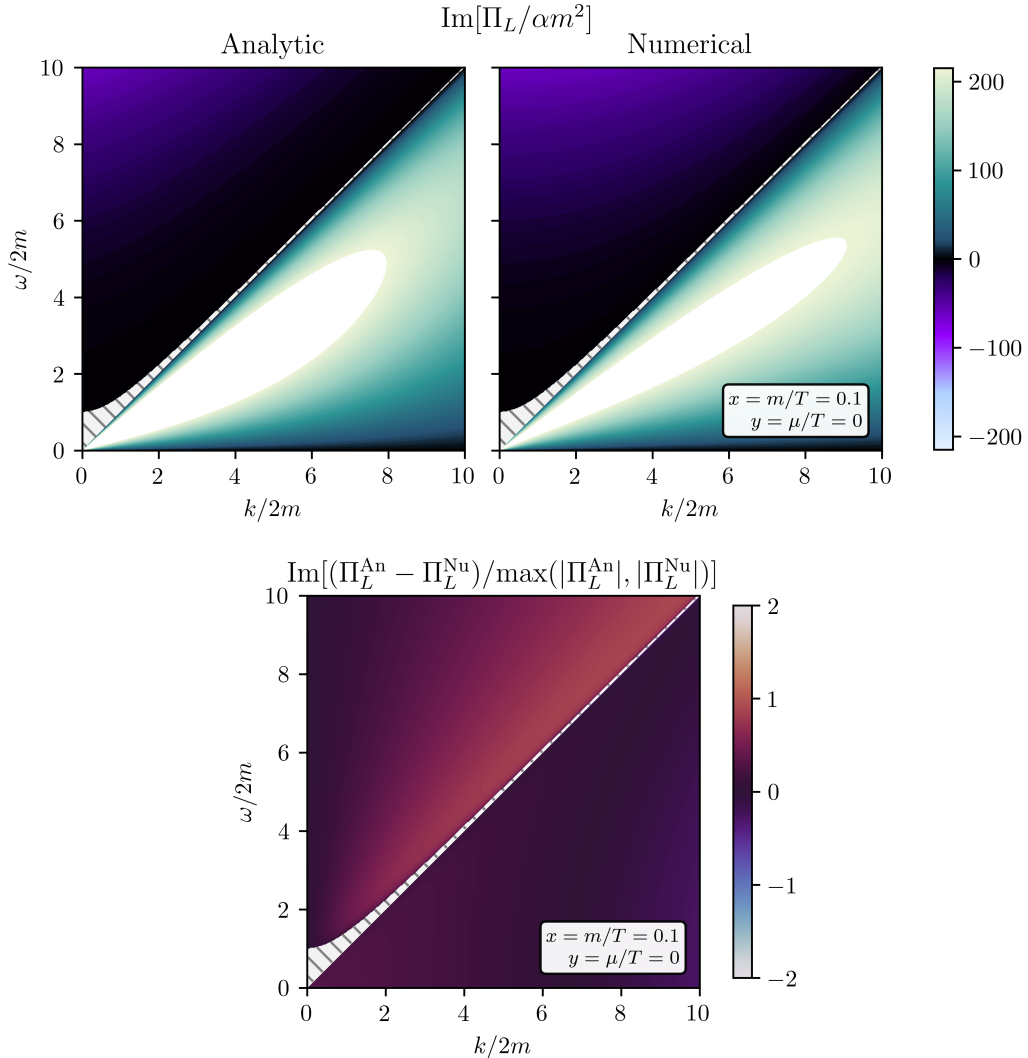


Figure 5.7: Plots of the imaginary part of the self-energy as a function of ω and k for L modes in the regime where $x = 0.1$ and $y = 0$. The self-energy is computed with the analytic approximation (top left panel) and the numerical integral of $D(v)$ (top right panel). The bottom panels show a ratio to assess the discrepancy between the analytic approximation and the numerical evaluation. The dashed region indicates where the imaginary part is exactly zero, due to kinematics arguments.

the region of phase space where the self-energy is exactly zero because none of the four processes involved is kinematically allowed. This is the region of light, timelike photons. The Braaten and Segel expressions do not have an imaginary part by design, and they are correct only for timelike photons in this dashed region, which is close to the on-shell region.

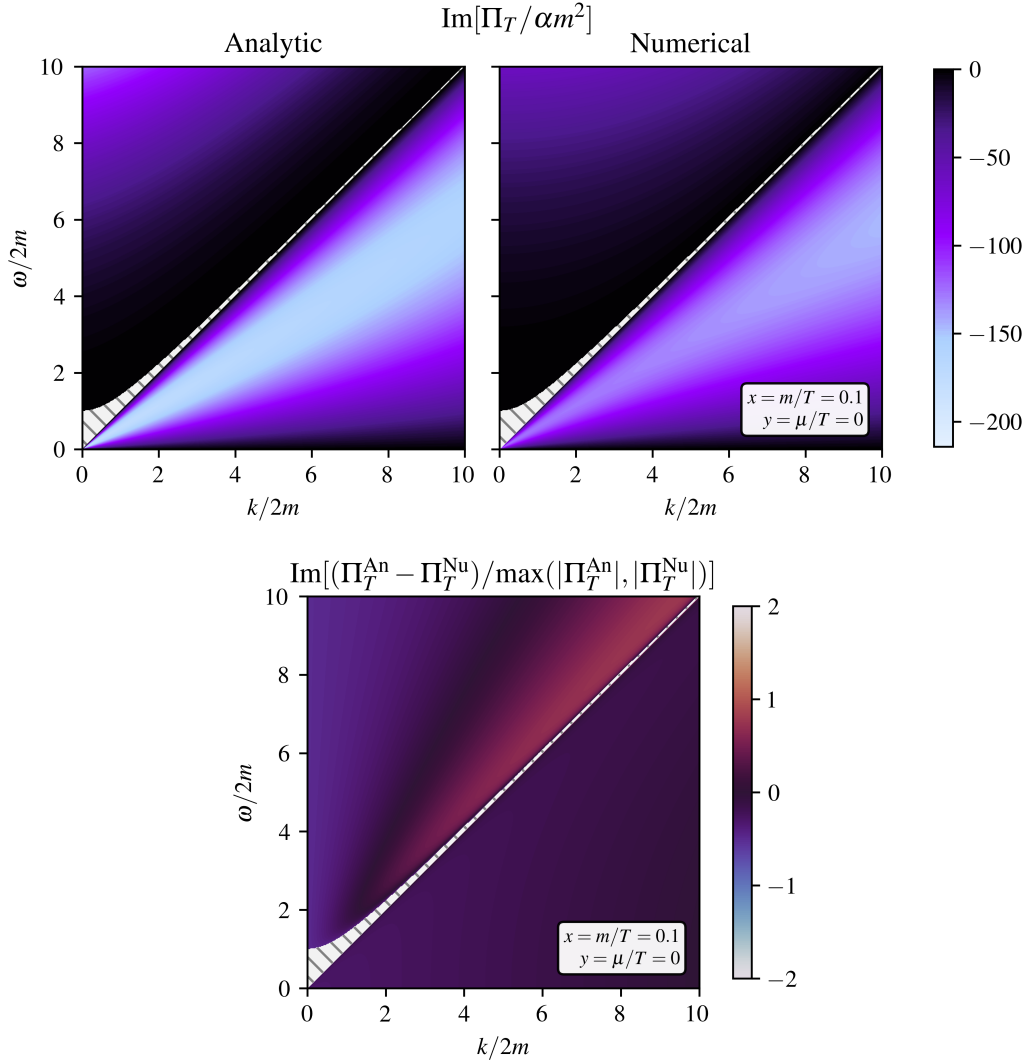


Figure 5.8: Plots of the imaginary part of the self-energy as a function of ω and k for T modes in the regime where $x = 0.1$ and $y = 0$. The display is the same as Figure 5.7.

The interpretation of these plots is very similar to the interpretation of the real part. Figures 5.7 and 5.8, for which $x = 0.1$ and $y = 0$, show that there are some discrepancies between the analytic approximation and the numerical computation. Despite these, the overall structure of the imaginary part of the self-energy in phase space is captured by this approximation. Crucially, the self-energy is non-zero when we get off shell, something that obviously isn't captured with the expressions from Braaten and Segel.

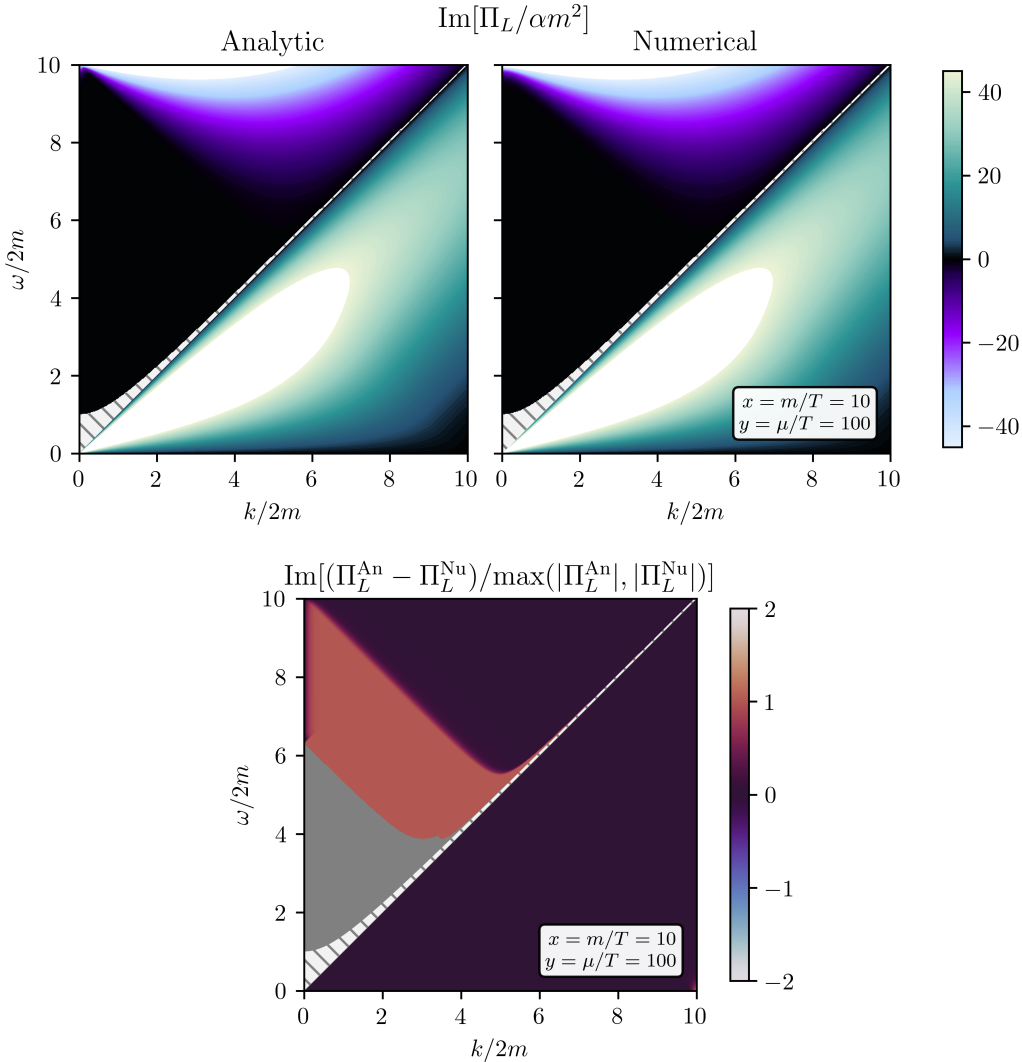


Figure 5.9: Plots of the imaginary part of the self-energy as a function of ω and k for L modes in the regime where $x = 10$ and $y = 100$. The display is the same as Figure 5.7. In the gray region, both the analytic and numerical expressions evaluate to zero.

Figures 5.9 and 5.10, for which $x = 10$ and $y = 100$, show that the analytic approximation is a good one in this different regime as well. Something revealed by the ratio plots, in the bottom panels of these, is that there is a high discrepancy between the analytic and numerical values in regions where the imaginary part of the self-energy is close to zero. This discrepancy becomes important for $\text{Im}[\Pi/\alpha m^2] \lesssim \alpha$. However, for such small imaginary parts, one needs to consider contributions from higher-loop self-energy diagrams, which involve processes like

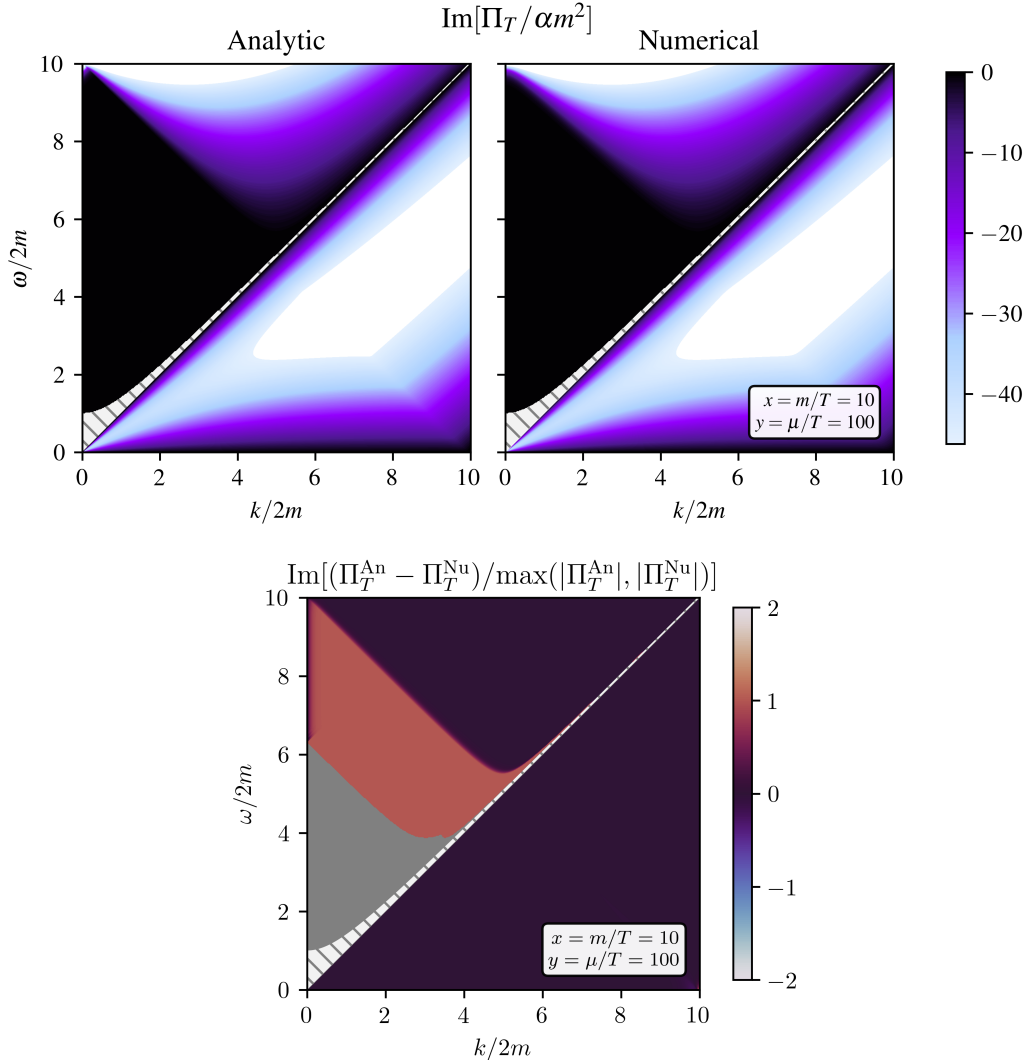


Figure 5.10: Plots of the imaginary part of the self-energy as a function of ω and k for T modes in the regime where $x = 10$ and $y = 100$. The display is the same as Figure 5.7. In the gray region, both the analytic and numerical expressions evaluate to zero.

Compton scattering and bremsstrahlung. Therefore, even if the approximations fail for small values of the imaginary part of the self-energy, this wouldn't have much impact on physical computations provided one considers the physically relevant higher-loop contributions. Note that the gray regions in these plots indicate that both the analytic and numerical expressions evaluate to zero, and the ratio cannot be correctly computed. On the top panels, these regions are shown in black and not in a dashed pattern to differentiate between regions of

phase space where the imaginary part evaluates to zero numerically and those where it is exactly zero for physical reasons.

Just like in the case of the real part, the accuracy of the analytic approximation depends on the regime (i.e., on the values of $x = m/T$ and $y = \mu/T$). Here again, the more relativistic regime ($x \ll 1$) seem to give rise to bigger discrepancies. Therefore, we can expect that this approximation is also most useful for phase space integration, and less for computing the self-energy at specific energy and momentum values.

Conclusion

The photon self-energy is an important quantity, used among other things to place bounds on physics beyond the standard model from cosmology and astrophysics. Scientists have mainly used the analytical approximations derived by Braaten and Segel for the photon self-energy at one loop. Those are only valid for on-shell photons or for photons with soft momenta, but that fact has been overlooked and people have used them for off-shell photons as well. As I have demonstrated in this thesis, Braaten and Segel's formulas break when going away from the on-shell regime. One example of a key qualitative difference is the fact that the self-energy is negative for some values of energy and momentum. One of my main results is the new analytic approximations that I have developed for the photon self-energy at one loop. These approximations are generally valid for both off-shell and on-shell photons. From these, we can recover Braaten and Segel's expressions in the appropriate limit.

For specific values of the photon's energy and momentum and the medium's temperature and chemical potential, these new expressions do faithfully approximate the photon self-energy. However, the approximations always reproduce the general behavior of the self-energy, including the negative value in some regions of phase space. Therefore, they are nonetheless very promising for integration over phase space, a situation where having analytic approximations is most useful. In addition, the analytic approximations for the imaginary part fail when $\text{Im}[\Pi/m^2] \lesssim \mathcal{O}(\alpha^2)$. However, this situation requires considering higher-loop processes, so this discrepancy has no impact on self-consistent physical computations.

The next steps are to revisit some of the bounds placed on physics beyond the Standard Model. In particular, multiple bounds on the dark photon parameter space rely on processes involving off-shell photons. These should be reanalyzed and updated, since the qualitatively different behavior of the photon self-energy off shell has the potential to significantly modify predictions. More broadly, bounds for all dark sector particles interacting with photons should be reassessed in light of these results. We also leave it to future work to investigate potential new signatures and observations from the distinct off-shell photon behavior.

This work generalized previous calculations of the photon self-energy by expanding the validity to all off-shell photons. Key assumptions were homogeneity and isotropy, as well as thermal equilibrium, which are good approximations for many astrophysical and cosmological environments. Future work can still generalize this further by dropping one or more of these assumptions, thus expanding the use of an accurate photon self-energy to an even broader range of physical environments.

Appendix

A Discrepancies between analytic and numerical

The agreement between the analytic approximation and the numerical evaluation of the real part of the self-energy in Chapter 5 depends on the regime, i.e., on the values of μ and T . Figures 5.4 and 5.5 show excellent agreement, meaning that the approximation is very good in this regime. However, Figures 5.2 and 5.3 show big discrepancies. The computation of $J_a(v)$ being quite involved, we need to make sure that this isn't due to mistakes in the final expression, but really due to an actual failure of the approximation in this regime. To do so, recall that the exact real part of the self-energy can be computed numerically in two ways:

$$\Pi_a = m^2 \frac{4\alpha}{\pi} \int_0^1 dv (f + \bar{f}) F_a(v), \quad (\text{A.1})$$

$$\Pi_a = \int_0^1 dv J_a(v) \frac{d\omega_p^2}{dv}, \quad (\text{A.2})$$

which are respectively Equations (4.31) and (4.39). The subplots labeled “Numerical” in Figures 5.2 to 5.5 use Equation (A.1). To verify that $J_a(v)$ has no mistakes in it, we also compute the numerical self-energy using Equation (A.2). Both numerical computation are shown in Figure A.1, for the same regime as in Figures 5.2 and 5.3. This clearly shows that they both give exactly the same result except for small numerical errors. We conclude that $J_a(v)$ is correct, and that it is the sharp peak approximation that fails in this regime.

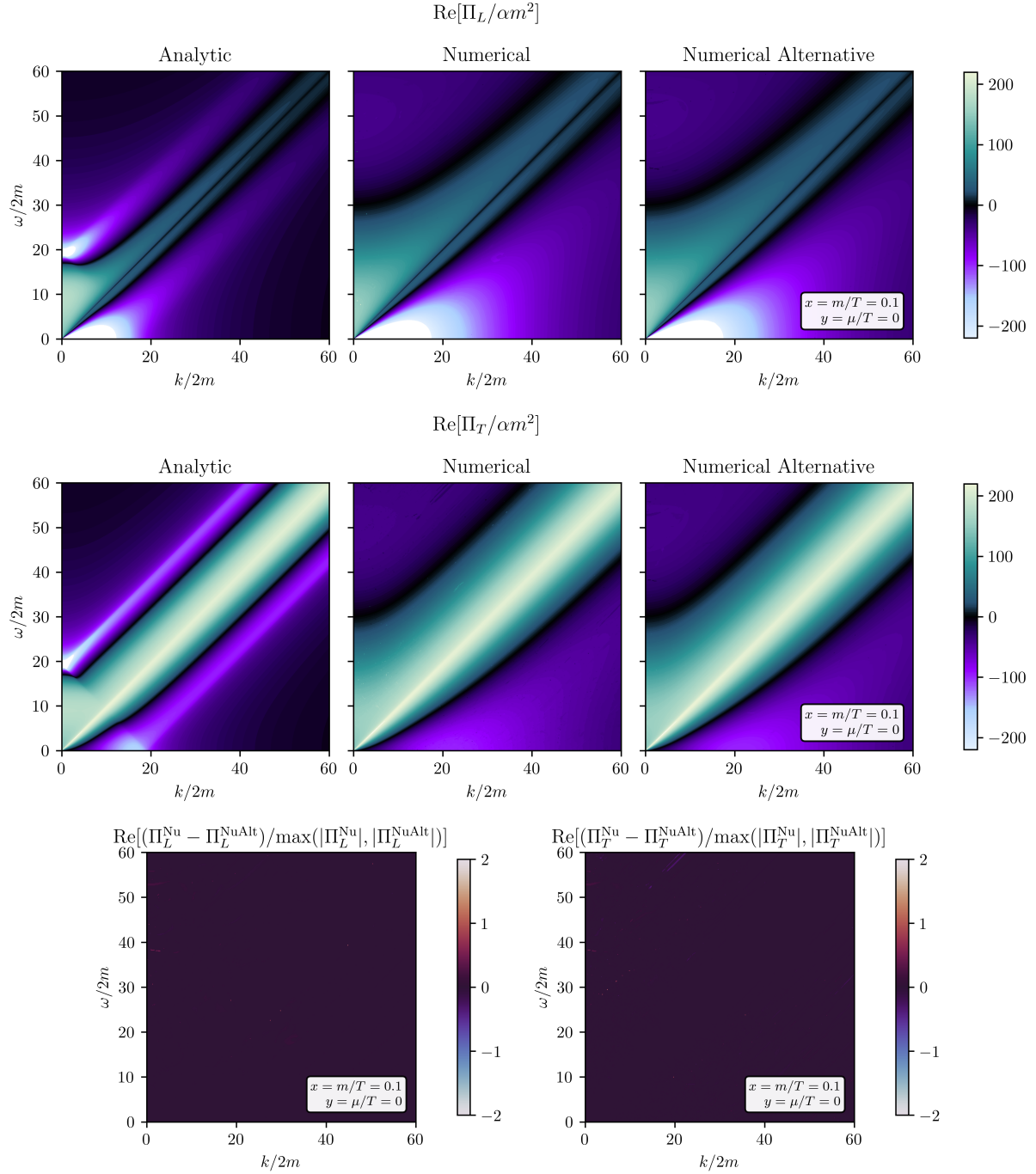


Figure A.1: Plots of the real part of the self-energy as a function of ω and k for L modes (top) and T modes (middle) in the regime where $x = 0.1$ and $y = 0$. The self-energy is computed with the analytic approximation $\Pi_a \simeq \omega_p^2 J(v_*)$ (left panel), the numerical integral using Equation (A.1) (middle panel), and the alternative numerical integral using Equation (A.2) (right panel). The bottom panels show a ratio to assess the discrepancy between both numerical evaluations, for L modes (left) and T modes (right).

References

- [1] Eric Braaten and Daniel Segel. “Neutrino energy loss from the plasma process at all temperatures and densities”. In: *Physical Review D* 48 (Aug. 1993), pp. 1478–1491. DOI: [10.1103/PhysRevD.48.1478](https://doi.org/10.1103/PhysRevD.48.1478).
- [2] G. G. Raffelt. *Stars as laboratories for fundamental physics: The astrophysics of neutrinos, axions, and other weakly interacting particles*. May 1996. ISBN: 978-0-226-70272-8.
- [3] Patrick Aurenche et al. “Landau-Pomeranchuk-Migdal resummation for dilepton production”. In: *Journal of High Energy Physics* 2002.12 (Jan. 2003), p. 006. DOI: [10.1088/1126-6708/2002/12/006](https://doi.org/10.1088/1126-6708/2002/12/006).
- [4] Daniel Baumann. *Cosmology*. Cambridge University Press, July 2022. ISBN: 978-1-108-83807-8. DOI: [10.1017/9781108937092](https://doi.org/10.1017/9781108937092).
- [5] Planck Collaboration et al. “Planck 2018 results. VI. Cosmological parameters”. In: *Astronomy and Astrophysics* 641 (Sept. 2020), A6. DOI: [10.1051/0004-6361/201833910](https://doi.org/10.1051/0004-6361/201833910).
- [6] Douglas Clowe, Anthony Gonzalez, and Maxim Markevitch. “Weak-Lensing Mass Reconstruction of the Interacting Cluster 1E 0657–558: Direct Evidence for the Existence of Dark Matter*”. In: *The Astrophysical Journal* 604.2 (Apr. 2004), p. 596. DOI: [10.1086/381970](https://doi.org/10.1086/381970).

- [7] M. Markevitch et al. “Direct Constraints on the Dark Matter Self-Interaction Cross Section from the Merging Galaxy Cluster 1E 0657–56”. In: *The Astrophysical Journal* 606.2 (May 2004), p. 819. DOI: [10.1086/383178](https://doi.org/10.1086/383178).
- [8] Chandra X ray Observatory. *1E 0657-56: NASA Finds Direct Proof of Dark Matter*. Aug. 2006. URL: <https://chandra.harvard.edu/photo/2006/1e0657/index.html> (visited on 03/08/2024).
- [9] Marco Fabbrichesi, Emidio Gabrielli, and Gaia Lanfranchi. *The Physics of the Dark Photon*. 1st ed. SpringerBriefs in Physics. Springer Cham, Nov. 2020. ISBN: 978-3-030-62518-4. DOI: [10.1007/978-3-030-62519-1](https://doi.org/10.1007/978-3-030-62519-1).
- [10] Javier Redondo and Marieke Postma. “Massive hidden photons as lukewarm dark matter”. In: *Journal of Cosmology and Astroparticle Physics* 2009.02 (Feb. 2009). Publisher: IOP Publishing, pp. 005–005. DOI: [10.1088/1475-7516/2009/02/005](https://doi.org/10.1088/1475-7516/2009/02/005).
- [11] Andrea Caputo et al. “Dark photon limits: A handbook”. In: *Physical Review D* 104.9 (Nov. 2021). Publisher: American Physical Society, p. 095029. DOI: [10.1103/PhysRevD.104.095029](https://doi.org/10.1103/PhysRevD.104.095029).
- [12] Ciaran O’Hare. *Dark photon limits*. URL: <https://cajohare.github.io/AxionLimits/docs/dp.html> (visited on 02/23/2024).
- [13] Alfred Scharff Goldhaber and Michael Martin Nieto. “Photon and graviton mass limits”. In: *Reviews of Modern Physics* 82.1 (Mar. 2010), pp. 939–979. DOI: [10.1103/RevModPhys.82.939](https://doi.org/10.1103/RevModPhys.82.939).
- [14] Itay M. Bloch et al. “Searching for dark absorption with direct detection experiments”. In: *Journal of High Energy Physics* 2017.6 (June 2017), p. 87. ISSN: 1029-8479. DOI: [10.1007/JHEP06\(2017\)087](https://doi.org/10.1007/JHEP06(2017)087).

- [15] Haipeng An et al. “New limits on dark photons from solar emission and keV scale dark matter”. In: *Physical Review D* 102.11 (Dec. 2020). Publisher: American Physical Society (APS). ISSN: 2470-0029. DOI: [10.1103/PhysRevD.102.115022](https://doi.org/10.1103/PhysRevD.102.115022).
- [16] Javier Redondo. “Helioscope Bounds on Hidden Sector Photons”. In: *Journal of Cosmology and Astroparticle Physics* 07 (2008), p. 008. DOI: [10.1088/1475-7516/2008/07/008](https://doi.org/10.1088/1475-7516/2008/07/008).
- [17] Javier Redondo and Georg Raffelt. “Solar constraints on hidden photons re-visited”. In: *Journal of Cosmology and Astroparticle Physics* 08 (2013), p. 034. DOI: [10.1088/1475-7516/2013/08/034](https://doi.org/10.1088/1475-7516/2013/08/034).
- [18] Matthew J. Dolan, Frederick J. Hiskens, and Raymond R. Volkas. “Constraining Dark Photons with Self-consistent Simulations of Globular Cluster Stars”. In: (June 2023). arXiv: [2306.13335](https://arxiv.org/abs/2306.13335).
- [19] Haipeng An, Maxim Pospelov, and Josef Pradler. “New stellar constraints on dark photons”. In: *Physics Letters B* 725.4-5 (Oct. 2013), pp. 190–195. DOI: [10.1016/j.physletb.2013.07.008](https://doi.org/10.1016/j.physletb.2013.07.008).
- [20] J. D. Jackson John David. *Classical electrodynamics*. 2nd. New York: Wiley. ISBN: 978-0-471-43132-9.
- [21] Michael E Peskin and Daniel V Schroeder. *An introduction to quantum field theory*. Boulder, CO: Westview, 1995. ISBN: 978-0-367-32056-0.
- [22] Ashok K. Das. *Finite Temperature Field Theory*. New York: World Scientific, 1997. ISBN: 981-02-2856-2. DOI: [10.1142/3277](https://doi.org/10.1142/3277).
- [23] Mikko Laine and Aleksi Vuorinen. *Basics of Thermal Field Theory*. 1st. Vol. 925. Lecture Notes in Physics. Springer Cham, June 2016. ISBN: 978-3-319-31932-2. URL: <https://doi.org/10.1007/978-3-319-31933-9>.

REFERENCES

- [24] H. Arthur Weldon. “Simple Rules for Discontinuities in Finite Temperature Field Theory”. In: *Physical Review D* 28 (1983), p. 2007. DOI: [10.1103/PhysRevD.28.2007](https://doi.org/10.1103/PhysRevD.28.2007).
- [25] J. I. Kapusta and Charles Gale. *Finite-temperature field theory: Principles and applications*. Cambridge Monographs on Mathematical Physics. Cambridge University Press, 2011. ISBN: 978-1-00-940195-1. DOI: [10.1017/CBO9780511535130](https://doi.org/10.1017/CBO9780511535130).
- [26] Eric Braaten. “Neutrino Emissivity of an Ultrarelativistic Plasma from Positron and Plasmino Annihilation”. In: *Astrophysical Journal* 392 (June 1992), p. 70. DOI: [10.1086/171405](https://doi.org/10.1086/171405).